1977

West Antarctic Ice Streams

Terence J. Hughes
University of Maine - Main, terry.hughes@maine.edu

West Antarctic Ice Streams

T. HUGHES[1]

Department of Geological Sciences, Institute for Quaternary Studies
University of Maine at Orono, Orono, Maine 04473

Solar heat is the acknowledged driving force for climatic change. However, ice sheets are also capable of causing climatic change. This property of ice sheets derives from the facts that ice and rock are crystalline whereas the oceans and atmosphere are fluids and that ice sheets are massive enough to depress the earth's crust well below sea level. These features allow time constants for glacial flow and isostatic compensation to be much larger than those for ocean and atmospheric circulation and therefore somewhat independent of the solar variations that control this circulation. This review examines the nature of dynamic processes in ice streams that give ice sheets their degree of independent behavior and emphasizes the consequences of viscoplastic instability inherent in anisotropic polycrystalline solids such as glacial ice. Viscoplastic instability and subglacial topography are responsible for the formation of ice streams near ice sheet margins grounded below sea level. As a result the West Antarctic marine ice sheet is inherently unstable and can be rapidly carved away by calving bays which migrate up surging ice streams. Analyses of tidal flexure along floating ice stream margins, stress and velocity fields in ice streams, and ice stream boundary conditions are presented and used to interpret ERTS 1 photomosaics for West Antarctica in terms of characteristic ice sheet crevasse patterns that can be used to monitor ice stream surges and to study calving bay dynamics.

1. INTRODUCTION

The basic proposition of this review is that West Antarctic ice streams are inherently unstable components of the Antarctic ice sheet and, by controlling the stability of the marine portion of this ice sheet, are capable of influencing global climatic stability. Before this proposition can be developed, it is useful to define certain glaciological terms. An ice sheet is a continent-sized mass of ice and snow thick enough to flow under its own weight, behaving as a unified dynamic system, and consisting of terrestrial portions grounded on continental shields that are above sea level when unglaciated, marine portions grounded on continental shelves that are below sea level when unglaciated, and floating portions called ice shelves. Ice sheets form from growing mountain glaciers and from the coalescence of ice caps, which are grounded and have centers of spreading called ice domes. Ice shelves form from thickening sea ice and from the coalescence of ice streams, which are fast-flowing currents of ice in marine ice caps or the marine portion of an ice sheet. Outlet glaciers are ice streams that flow in fjords through coastal mountains. Ice rises are ice domes which exist where ice shelves are grounded on bedrock pinning points.

Perhaps only two ice sheets can form on our planet [*Hughes*, 1975*a*; *Hughes et al.*, 1977], an Arctic ice sheet (of which the Greenland ice sheet is a remnant) and an Antarctic ice sheet (which has predominantly terrestrial ice domes in its eastern hemisphere portion and predominantly marine ice domes in its western hemisphere portion). In this review the terms ice dome and ice shelf are used to distinguish the grounded and floating portions of an ice sheet.

Recent studies [*Hughes*, 1972*a*, 1973*a*, *b*, 1974, 1975*a*, *b*, 1976; *Johnsen et al.*, 1972; *Whillans*, 1973; *Langway et al.*, 1974; *Weertman*, 1974; *Denton and Borns*, 1974; *Thomas*, 1976] have examined various aspects of the question, 'Is the West Antarctic ice sheet disintegrating?' This proposition is summarized in Figure 1 and consists of 10 postulates. (1) During global ice ages the Antarctic ice sheet expands to the edge of the Antarctic continental shelf, shown by the dashed 500-m bathymetry contour in Figure 1. (2) Glacial flow near the ice sheet margin becomes concentrated in fjords and channels between mountains and islands along the coast to form outlet glaciers and ice streams, shown by the dotted areas in Figure 1. (3) At the end of an ice age these outlet glaciers and ice streams punch through the ablating ice shelves fringing Antarctica and surge along glacially eroded bedrock troughs, as shown by the arrows in Figure 1. (4) The Ross and Filchner-Ronne ice shelves were created because ice shelf grounding lines retreated up surging West Antarctic ice streams faster than the ice shelf margins retreated by iceberg calving. (5) Retreat of an ice shelf grounding line is slowed when the surging ice streams and outlet glaciers can no longer effectively punch through the ice shelf. (6) Retreat of the ice shelf grounding line stops when it reaches high bedrock up-down sills in ice stream channels and upward steps in glacier fjords. (7) Foredeepening by glacial erosion creates low sills at the front of ice stream channels ending at the edge of the continental shelf and high steps at the rear of outlet glacier fjords beginning at the edge of the continental shield. (8) The Antarctic ice sheet is primarily grounded over a continental shield in its eastern hemisphere portion and a continental shelf in its western hemisphere portion, so the East Antarctic ice sheet is inherently stable because outlet glacier grounding lines cannot retreat beyond high steps, and the West Antarctic ice sheet is inherently unstable because ice stream grounding lines can retreat beyond low sills. (9) A basal water layer uncouples ice from the bed under outlet glaciers and ice streams, giving them concave surfaces which migrate into the heart of an ice sheet during a surge because ice-bed uncoupling moves inland ahead of a retreating ice shelf grounding line. (10) The West Antarctic ice sheet is presently disintegrating, stable, or growing, depending on whether the surface inflection lines and ice shelf grounding lines associated with West Antarctic ice streams are retreating, stationary, or advancing.

The above 10 postulates can be tested by an intensive investigation of the dynamics of outlet glaciers and ice streams. Byrd Glacier begins as an ice stream behind the Transantarctic

[1] Also at National Center for Atmospheric Research, Boulder, Colorado 80307.

Paper number 6R0700.

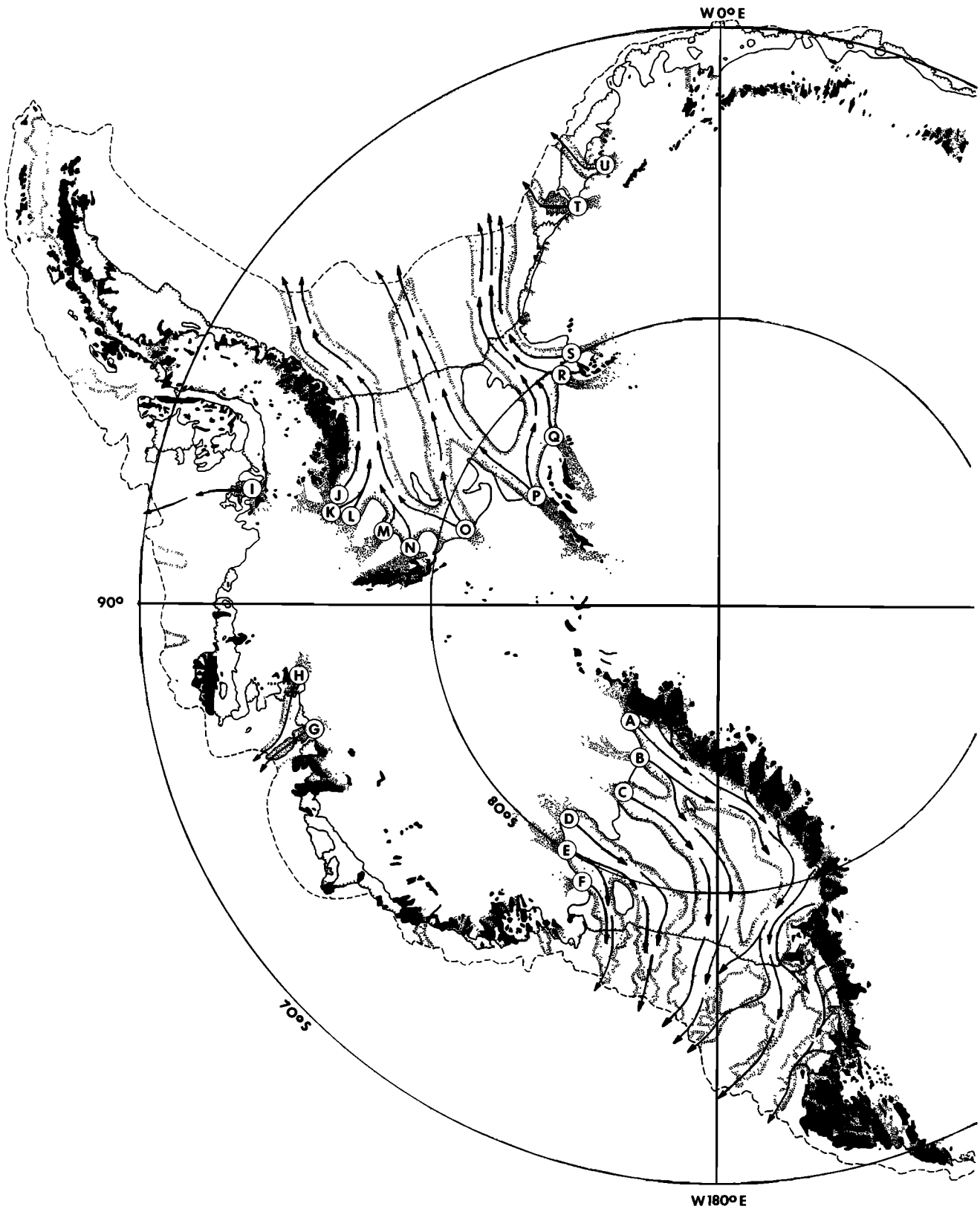

Fig. 1. The role of ice streams in disintegration of the West Antarctic ice sheet during the Holocene. Letters A through U identify the major West Antarctic ice streams presently active, the letters being located at the ice dome–ice shelf junction. Dotted areas on the ice dome side of the junction identify the concave surge basins of the ice streams. Dotted areas on the ice shelf side of the junction identify the bedrock troughs eroded by the surging ice streams when they retreated from the continental shelf margin. The dashed line identifies the continental shelf margin of West Antarctica and the approximate limit of the West Antarctic ice domes during the Wisconsin. The solid line identifies the present limit of the West Antarctic ice domes. The hatchured lines identify the present limits of West Antarctic ice shelves. Black areas identify unglaciated regions and regions where glaciated mountains project above the ice sheet. Arrows show the continuity between past and present ice streams during disintegration of the West Antarctic ice sheet. These arrows emphasize the fact that present Antarctic outlet glaciers are merely the remnants of huge ice streams that extended to the continental shelf margin during the Wisconsin and retreated during the Holocene to the mountain barrier separating shelf portions from shield portions of the Antarctic continent and the corresponding marine portions from terrestrial portions of the Antarctic ice sheet

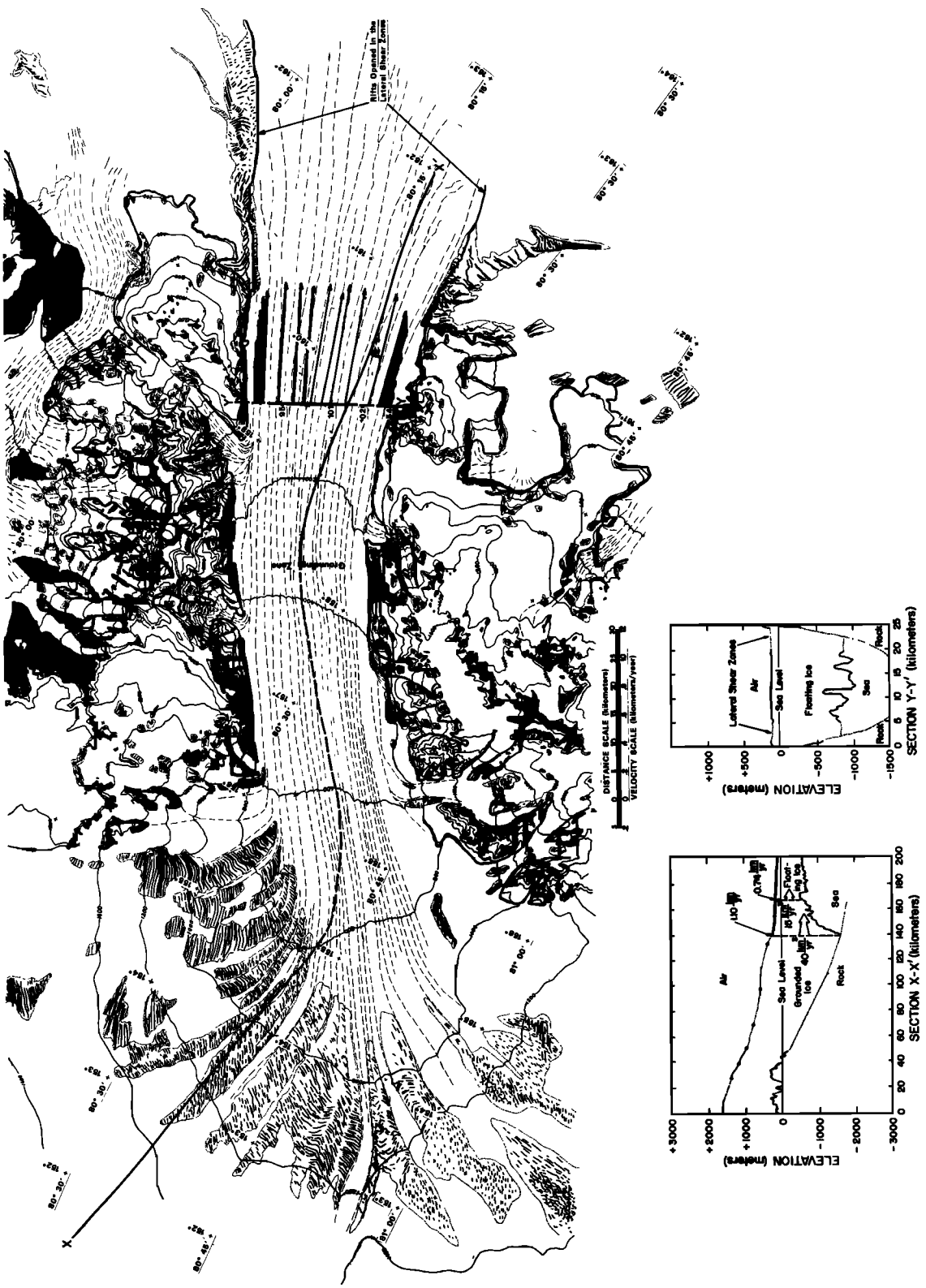

Fig. 2. The Byrd Glacier flow regime. The plan view, contoured at 200-m elevation intervals, shows unglaciated parts of the Transantarctic Mountains (black areas), flight lines for aerial radar sounding (lines *X-X'* and *Y-Y'*), an ice velocity profile across the floating portion of Byrd Glacier (arrows), and major crevasse patterns in ice entering and leaving Byrd Glacier fjord (line segments in areas enclosed by dotted lines). The profile views along flight lines *X-X'* and *Y-Y'* show the top and bottom surfaces of Byrd Glacier (solid lines) except along the dashed portion of the flight line where crevasses scattered the radar signal (dotted lines). The ice thickness profiles were determined by radar sounding (P. Calkin, unpublished material, 1972). The ice velocity profile was determined by aerial photogrammetry [*Swithinbank*, 1963]. The 40-km^3/yr ice flux is based on a mass balance calculation, and the 15-km^3/yr ice flux is based on the ice velocity profile [*Hughes*, 1974].

TABLE 1. Approximate Equilibrium

	Width,[a] km	Depth,[b] km	Velocity,[c] m/yr	Velocity,[c] m/yr	Length, km	Travel Time, yr	Velocity Change, m/yr
1100-m contour[g]	120	~1.1	~117				
				230	45	196	+227
Fjord entrance[h]	28	~1.6	~344				
				348	40	115	+8
Grounding zone[i]	23	1.9	352				
				476	50	105	+248
Fjord exit[j]	32	0.8	600				
				546	26	46	−64
Lateral rift[k]	41	0.7	536				

[a]Measured across glacier surface.
[b]Measured along cross section X-X' with depths extrapolated across regions where bottom radar reflections vanish.
[c]Based on velocity profile measured across cross section Y-Y', surface width (26 km) and mean ice thickness (0.8 km) at cross section Y-Y', and measured surface widths and section X-X' thicknesses of other cross sections, assuming that ice flux across all cross sections was constant and surface mass balance between cross sections was nil.
[d]Upstream depth, L_z'; downstream depth, L_z''. Upstream width, L_y'; downstream width, L_y''.
[e]Given by $\epsilon_z = \ln (L_z''/L_z')$, $\epsilon_y = \ln (L_y''/L_y')$, $\epsilon_x = -(\epsilon_z + \epsilon_y)$.

Mountains, becomes an outlet glacier as it passes through the mountains, and ends as an ice stream penetrating the Ross Ice Shelf. Figure 2 and Table 1 suggest some important features of Byrd Glacier. (1) Byrd Glacier has the velocity and chaotic surface characteristic of a surge. (2) The surge cannot propagate into the East Antarctic ice sheet because the Ross Ice Shelf grounding line cannot propagate beyond a bedrock step at the end of Byrd Glacier fjord. (3) Surface elevation contours show that Byrd Glacier has a concave surface on the ice dome side of the grounding line and a convex surface on the ice shelf side of the grounding line, consistent with extending and compressive flow in these respective regions. (4) Transverse, shear, and longitudinal crevasses predominate for the regions of converging, laminar, and diverging flow in the ice dome, ice fjord, and ice shelf portions of Byrd Glacier, respectively. (5) High crevasse density, indicated by regions where aerial radar sounding signals are not returned, decreases abruptly across the grounding line which separates the grounded and floating parts of Byrd Glacier and across the maximum slope surface inflection lines which separate Byrd Glacier from the ice domes and the ice shelf. (6) Changes in crevasse orientation and density require changes in the direction and magnitude of the principal surface strain rates, which require ice recrystallization to create new grain fabrics. (7) Rapid upstream ice thickening toward the grounding line of the floating portion of Byrd Glacier and ice flux calculations suggest nonequilibrium conditions and grounding line advance. (8) The velocity profile across Byrd Glacier, determined by monitoring crevasse migrations by means of aerial photogrammetry, is a measure of the frictional resistance of the fjord walls to glacial flow. (9) The longitudinal and transverse cross sections across Byrd Glacier suggest broad and narrow grounding zones with pinned and hinged boundary conditions during tidal flexure, respectively. (10) Seawater entering bottom crevasses during tidal flexure allows them to migrate upward and meet surface crevasses, thereby providing the only break in continuity of the ice dome–ice stream–ice shelf dynamic system, as can be seen by the lateral rifts in the floating portion of Byrd Glacier that begin in tidal flexure zones along the sides of Byrd Glacier fjord.

All these features will be examined more closely in the following sections. First, the important role of ice crystal anisotropy in global climatic stability is pinpointed by analyzing stable, unstable, and metastable equilibrium in terms of the cryosphere, hydrosphere, and atmosphere components of the earth's climatic machine; the ice dome, ice stream, and ice shelf components of the cryosphere; and the elastic, slow viscoplastic, and fast viscoplastic stages of polycrystalline ice deformation. Second, an attempt is made to quantitatively relate ice crystal anisotropy to viscoplastic instability during the deformation of polycrystalline ice. Third, this quantitative relationship is applied to elastic-viscoplastic tidal flexure along the ice dome–ice shelf junction of ice streams and outlet glaciers. Fourth, the stress and velocity fields of ice streams and outlet glaciers are described for homogeneous flow and compared with nonhomogeneous flow related to viscoplastic instability arising from crystal anisotropy in glacial ice. Fifth, boundary conditions along the sides, at the grounding line, and on the surface of an ice stream are related to zones of viscoplastic instability, ice shelf constraints, and crevasse patterns, respectively. Sixth, the relationship between viscoplastic instability and surface crevasse patterns is applied to photo interpretation of ERTS 1 imagery to investigate the character of ice streams, outlet glaciers, ice shelves, ice rises, and calving bays associated with the West Antarctic ice sheet.

2. Stable, Unstable, and Metastable Equilibrium

a. Cryosphere-Hydrosphere-Atmosphere Climatic Stability

Solar energy drives the earth's climatic machine, and variations in solar input provide the primary trigger for climatic fluctuations, given the present distribution of continents and oceans. These variations are caused by changes in solar output (correlated with sunspot activity and reversals in polarity of the sun's magnetic field), changes in solar radiation reaching the earth (correlated with variations in the eccentricity of the earth's orbit), changes in the amount of solar radiation reaching various latitudes on the earth's surface (correlated with variations in the tilt of the earth's rotation axis relative to its orbital plane), changes in the amount of solar radiation filtered through the earth's atmosphere (correlated with atmo-

Strain Rates Expected for Byrd Glacier

Normalized Distance Change[d]		Strain[e]			Strain Rate,[f] 10^{-3}/yr		
L_z''/L_z'	L_y''/L_y'	ϵ_z	ϵ_y	ϵ_x	$\dot{\epsilon}_z$	$\dot{\epsilon}_y$	$\dot{\epsilon}_x$
1.451	0.233	+0.372	−1.457	+1.085	+1.9	−7.4	+5.5 (+5.1)
1.187	0.821	+0.171	−0.197	+0.026	+1.5	−1.7	+0.2 (+0.2)
0.421	1.390	−0.865	+0.329	+0.536	−8.2	+3.1	+5.1 (+5.0)
0.875	1.280	−0.134	+0.247	−0.113	−2.9	+5.4	−2.5 (−2.5)

[f]Calculated by dividing strains by travel times. Strain rate $\dot{\epsilon}_x$ was also calculated by dividing velocity change by length and is given in parentheses.
[g]Approximate maximum slope surface inflection line marking beginning of Byrd Glacier.
[h]Coincides approximately with 600-m elevation contour.
[i]Assumed to occur where radar reflections vanish at bottom surface along cross section X-X'.
[j]Located at beginning of lateral rift zone separating floating part of Byrd Glacier from Ross Ice Shelf.
[k]End of southern lateral rift used because rift is shortest.

spheric turbidity, cloudiness, and carbon dioxide content), and radiation changes caused by combinations of these variations. Since some variations are periodic and others are not, the net solar energy flux varies in a semipredictable way from the 11-yr sunspot cycle to the 96,600-yr cycle of orbital eccentricity variations. Known variations in solar output are small and short term in comparison with variations in solar input to the earth caused by changing planetary motions. Hence the former affect weather, and the latter affect climate.

The cryosphere, hydrosphere, and atmosphere components of the earth's climatic machine have markedly different properties determined by their solid, liquid, and gaseous physical states and their differences in mass and distribution over the earth's surface. These differences and their consequences for climatic stability have been discussed elsewhere [*Hughes*, 1973*a*]. These properties are compared in Table 2.

The hydrosphere consists mainly of the oceans. The heat capacity, mass, and momentum of the climatic machine are essentially ocean values, so the thermal and dynamic inertia of the oceans maintains the overall climatic stability which makes our planet habitable. Variations in solar input cause small short-term and large long-term perturbations in this fundamental climatic stability.

Short-term perturbations affect atmospheric circulation. The atmosphere consists mainly of the troposphere. The kinetic energy of the climatic machine is essentially tropospheric kinetic energy. However, the troposphere has the lowest mass and highest velocity of all components in the earth's climatic machine. Hence variations in its kinetic energy due to changes in solar input do not result in momentum changes that are large enough and long enough to change oceanic momentum. Consequently, the atmosphere controls only small short-term climatic variations such as changes in weather.

Long-term perturbations affect cryospheric flow. The cryosphere, especially the flowing cryosphere, consits mainly of ice sheets. The mass and heat capacity of ice sheets are a significant fraction of those for the oceanic surface layer driven by atmospheric winds. By changing sea level, ice sheets adjust this fraction and regulate the surface area of ocean-atmosphere coupling. External ice sheet flow (growth and decay of ice sheets) is solar driven because ice sheets are part of the cryosphere-hydrosphere-atmosphere climatic machine. But internal ice sheet flow (creep deformation and basal sliding) is gravity driven because ice is a crystalline solid. Time constants for both types of flow and for crustal isostatic adjustments to growing or decaying ice sheets are much slower than, and hence independent of, those for ocean and atmospheric circulation. These features of ice sheets allow ice sheet dynamics to change the dynamics of the earth's climatic machine and at the same time maintain a degree of independence from the climatic machine. Consequently, ice sheets help control large long-term climatic variations such as glacial-interglacial ages.

TABLE 2. Selected Physical Characteristics of the Components of the Cryosphere-Hydrosphere-Atmosphere Dynamic System

	Cryosphere		Hydrosphere		
	Land	Sea	Deep	Surface	Atmosphere
Component circulation time, yr	1×10^{4}	2×10^{0}	1×10^{3}	1×10^{21}	5×10^{-2}
H_2O residence time, yr	1×10^{5}	5×10^{-1}	5×10^{3}	1×10^{3}	1×10^{-2}
Heat capacity, cal/°C	1×10^{22}	1×10^{19}	1×10^{24}	5×10^{21}	6×10^{20}
Mass, kg	3×10^{19}	5×10^{16}	1×10^{21}	1×10^{20}	5×10^{18}
Momentum, kg m/yr	9×10^{20}	3×10^{28}	1×10^{25}	1×10^{27}	2×10^{27}
Kinetic energy, kg m^2/yr^2	3×10^{22}	2×10^{30}	1×10^{29}	1×10^{34}	8×10^{35}

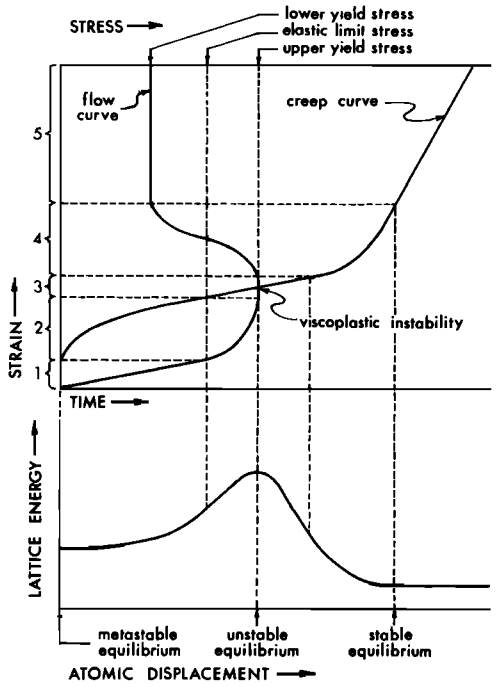

Fig. 3. Viscoplastic instability in ice streams and outlet glaciers related to the flow curve, the creep curve, and the energy curve for polycrystalline ice. The five stages of strain in polycrystalline ice are elastic strain (stage 1), transient strain (stage 2), slow steady state strain (stage 3), transitional strain (stage 4), and fast steady state strain (stage 5). These stages are defined by the creep curve (strain versus time). On the flow curve (strain versus stress) the elastic limit stress coincides with the end of stage 1, the upper yield stress coincides with the middle of stage 3, and the lower yield stress coincides with the beginning of stage 5. On the energy curve, metastable equilibrium exists during stage 1, unstable equilibrium exists during stage 3, and stable equilibrium exists during stage 5, the transition from metastable to unstable equilibrium occurring during stage 2 and the transition from unstable to stable equilibrium occurring during stage 4. Hence the energy curve has zero slopes during the time-independent stages 1, 3, and 5 and maximum slopes during the time-dependent stages 2 and 4, which represent rates of zero and maximum energy change, respectively. The interfaces between the ice dome, ice stream, and ice shelf in the ice sheet dynamic system are regions where viscoplastic instability occurs. Viscoplastic instability occurs at the strain where the creep and flow curves coincide and causes recrystallization of glacial ice. A transition from flow dominated by hard glide to flow dominated by easy glide which causes a strain rate increase $\dot{\epsilon}_5 = 10\ \dot{\epsilon}_3$ in the creep curve (constant stress) causes a stress decrease $\sigma_5 = 10^{-1/3}\sigma_3$ in the flow curve (constant strain rate), since $\dot{\epsilon} \propto \sigma^3$ for ice.

Each major component of the earth's cryosphere-hydrosphere-atmosphere climatic machine plays a unique role in determining climatic equilibrium. Oceans constitute the component which responds reversibly to variations in solar input and is therefore in a state of stable equilibrium which acts to maintain a steady state climate. The troposphere is the component which responds irreversibly to variations in solar input and is therefore in a state of unstable equilibrium which can sustain only small short-term climate changes. Ice sheets constitute the component having internal independent behavior which responds reversibly to small variations in solar input and having external dependent behavior which responds irreversibly to large variations in solar input. Therefore ice sheets exist in a state of metastable equilibrium which can sustain large long-term climate changes. The metastability, size, and distribution of ice sheets enable them to cause climatic change, as well as to be affected by climatic change, whereas the oceans and atmosphere are only affected by climatic change. It seems that solar input and ice sheet dynamics combine with continental drift to regulate the earth's climatic machine.

b. Ice Dome–Ice Stream–Ice Shelf Stability

Metastability in the cryosphere component of the earth's climatic machine is a result of inherent stable, unstable, and metastable equilibrium conditions which exist in the polar ice cover. Equilibrium in the polar ice cover consists of a delicate mass balance relationship between ice on land and on sea. Thickening of land ice causes ice caps to expand onto continental shelves which are below sea level. Thickening of sea ice causes pack ice to be transformed into ice shelves.

Ice caps grounded on continental shields form from snow fields over land which is above sea level when unglaciated. Examples of glaciated continental shields are East Antarctica and Greenland at present and Canada and Scandinavia in the past. Ice caps spreading over continental shields are in relatively stable equilibrium because sheetflow extends to the margin, permitting strong ice-bed coupling along the margin. Stable equilibrium results when the ice cap is able to adjust reversibly to climatic perturbations which change its mass balance regime [*Nye*, 1960*a*; *Weertman*, 1961].

Ice caps grounded on continental shelves form from a combination of thickening sea ice and transgression of land ice from continental shields as sea level falls. Examples of glaciated continental shelves are West Antarctica at present and the Barents Sea in the past. Ice caps grounded on continental shelves are in relatively unstable equilibrium because sheetflow becomes streamflow at the margin, resulting in strong ice-bed uncoupling along the margin. Streamflow results because mountains and islands typically exist along continental margins, so ice must flow between mountains as outlet glaciers and between islands as ice streams. Ice-bed uncoupling is a result of basal water generated by the frictional heat of ice deformation in streamflow. Unstable equilibrium results when the ice sheet adjusts irreversibly to climatic perturbations which influence precipitation and sea level. Ice sheets grounded below sea level on continental shelves are inherently unstable with respect to these external climatic perturbations [*Weertman*, 1974], internal glacial perturbations which cause ice streams to surge [*Hughes*, 1975*a*, 1976], and the delayed isostatic response of crustal loading or unloading by ice sheets [*Thomas*, 1976].

Ice shelves are necessary to stabilize a polar ice cover consisting of sea ice and land ice grounded on both continental shields (terrestrial ice domes) and continental shelves (marine ice domes), because the ice streams draining marine ice domes can plow through thin pack ice but not thick shelf ice. Hence ice shelves buttress in the inherently unstable marine ice sheets by stabilizing surges of its ice streams. Without this buttressing effect of ice shelves the ice stream surges would be unstable and would draw the marine ice dome down until it became a floating ice shelf. A climatic perturbation which removes the fringing ice shelf therefore also removes the marine ice dome and thereby fundamentally changes the equilibrium of the whole polar ice cover. An ice shelf has two equilibrium lines, one along its calving margin which is controlled by atmospheric temperature and one on its underside which is controlled by both ocean temperature and salinity [*Mercer*, 1968]. Since ice shelves are almost flat, a small climatic fluctuation which influences atmospheric temperature and ocean temperature or salinity can cause large displacements of the ice shelf equilibrium lines. All portions of the ice shelf on the ablation side of the equilibrium lines must eventually disappear if the climatic perturbation lasts long enough. Since small perturbations are generally of shorter duration than large per-

turbations, the ice shelf margin advances or retreats reversibly for small perturbations and irreversibly for large perturbations. Hence the ice shelf exists in a state of metastable equilibrium.

During ice ages, both the arctic and the antarctic have polar ice sheets consisting of unified ice dome–ice stream–ice shelf dynamic systems having stable, unstable, and metastable components. Today, only the antarctic ice sheet has these components. Specifically, the marine West Antarctic ice domes are held in unstable equilibrium between the terrestrial East Antarctic ice domes in stable equilibrium and the Ross, Filchner-Ronne, and smaller ice shelves in metastable equilibrium. If these ice shelves disappear, as they probably did during the last interglacial [*Mercer*, 1968], ice stream surges will be uncontained and will lead to rapid disintegration of the inherently unstable West Antarctic ice domes. Hence only the inherently stable East Antarctic and Greenland ice domes can be expected to survive during a full prolonged interglacial age. Even though external [*Weertman*, 1961, 1964*a*] and internal [*Wilson*, 1964; *Budd*, 1975] instability mechanisms can theoretically also reduce these ice domes, there is no conclusive evidence from sea levels that the mechanisms operated on a large scale during interglacials in East Antarctica and Greenland. *Hollin* [1972] discusses the evidence for this type of surge.

c. Viscoplastic Instability in Polycrystalline Ice

Unstable equilibrium inherent in marine ice domes is related partly to time variations in the progressive uncoupling of ice from bedrock across the ice dome–ice shelf junction and partly to time variations in the deformation of ice itself. Figure 3 relates the flow curve (stress versus strain) and the creep curve (strain versus time) to conditions of metastable, unstable, and stable equilibrium in glacial ice during deformation. Viscoplastic instability occurs at the strain where the flow and creep curves intersect. Five stages of strain can be identified from the slope of the creep curve for glacial ice having an initially random crystallographic orientation of grains. The slope of the creep curve is infinite for elastic strain (stage 1), decreases for transient strain (stage 2), has a finite minimum for slow steady state strain (stage 3), increases for transitional strain (stage 4), and has a finite maximum for fast steady state strain (stage 5). Fracture can terminate any of these stages if the strain rate is too rapid for a given ice temperature. The crevasse density in West Antarctic ice streams would therefore be an indication of increasing strain rates due to progressive ice-bed uncoupling toward the ice dome–ice shelf junction.

Slow steady state strain is commonly reported for creep of randomly oriented polycrystalline ice and creep for single-crystal ice oriented to permit only nonbasal slip (hard glide). Fast steady state strain is commonly reported for creep of strongly oriented polycrystalline ice and for creep of single-crystal ice oriented to permit only basal slip (easy glide). Hence slow and fast steady state strain are controlled by hard and easy glide, respectively, and the transitional strain separating them occurs during recrystallization from a hard glide ice fabric to an easy glide ice fabric.

The transition from hard to easy glide is illustrated in Figure 4 and in the schematic energy diagram in Figure 3. The lattice energy before the creep stress is applied consists mainly of the lattice distortion in grain boundaries due to the random alignment of crystals and represents a condition of metastable equilibrium. When the stress is applied, lattice distortion grows in the grains themselves because dislocations moving via easy glide in individual grains pile up at high-angle grain

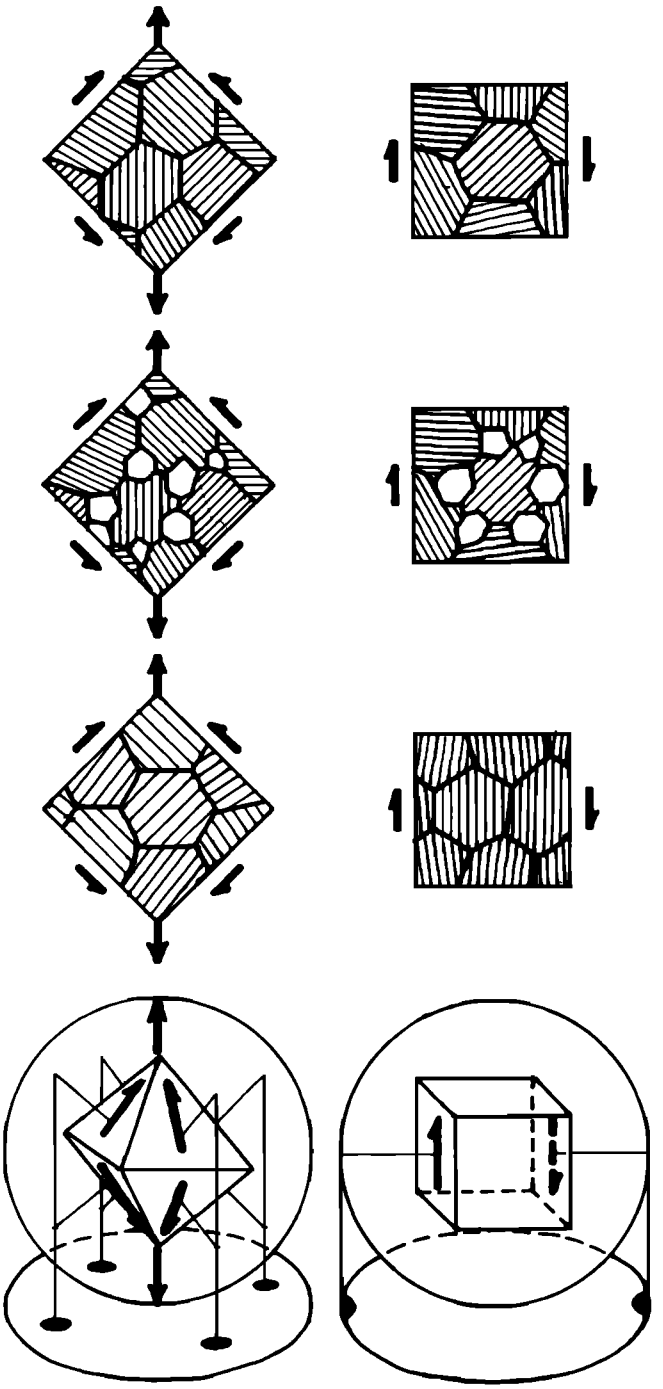

Fig. 4. Viscoplastic instability and recrystallization from random to preferred ice fabrics. The strain field is shown as arrows acting on the squares, ice crystals are polygons inside the squares, and basal slip planes are parallel lines inside the polygons. Randomly oriented polycrystalline ice is in unstable equilibrium with respect to a given strain field (top squares), so that strain leads to viscoplastic instability (center squares) and results in a preferred ice fabric in stable equilibrium with the strain field (bottom squares). The projected recrystallized ice fabric gives a four-pole preferred orientation for a uniaxial tensile strain (left) and a single-pole preferred orientation for a simple shear strain (right). Recrystallization begins when stress is concentrated in high-angle grain boundaries which cause easy glide (basal slip) in one grain to be transmitted as hard glide (nonbasal slip) in neighboring grains. Strain hardening results. During recrystallization, favorably oriented grains (white polygons in center squares) nucleate in high-angle grain boundaries and grow at the expense of unfavorably oriented grains until only low-angle grain boundaries remain. Strain softening results. More strain softening results from simple shear than from uniaxial tension because simple shear created the lowest-angle grain boundaries. In an ice stream, simple shear predominates toward the sides, and uniaxial tension predominates toward the center.

TABLE 3. Equilibrium Conditions Influencing Global Climatic Stability

Component	Metastable Equilibrium	Unstable Equilibrium	Stable Equilibrium
Climatic machine			
Cryosphere	ice sheets		
Atmosphere		troposphere	
Hydrosphere			oceans
Ice sheet dynamics			
Floating	ice shelves		
Marine		ice streams	
Terrestrial			ice domes
Ice deformation			
Elastic	no glide		
Slow steady state		hard glide	
Fast steady state			easy glide

boundaries where lattice energy and distortion are greatest. Metastable equilibrium becomes unstable equilibrium when new grains oriented to favor easy glide are nucleated in these grain boundaries and grow at the expense of old grains oriented to favor hard glide. Recrystallization results in a state of stable equilibrium in which nearly all grains are oriented to favor easy glide and dislocations therefore move across small-angle grain boundaries with minimal pileup. The pileup which does occur is reflected in the lower strain rate for easy glide in polycrystalline ice having a single-maximum fabric compared to easy glide in single-crystal ice. Conversely, the fact that the strain rate is higher for hard glide in polycrystalline ice having a single-maximum fabric than for hard glide in single-crystal ice is evidence that some easy glide occurs in the polycrystalline ice.

If Figure 3 is an accurate qualitative representation of creep, then slow steady state strain (stage 3) is really a stage of unstable equilibrium which exists only as an inflection point on the creep curve between transient strain (stage 2) and transitional strain (stage 4). Therefore all data reported in the literature for creep tests on randomly oriented polycrystalline ice that were terminated prior to recrystallization are measurements of unstable steady state strain controlled by hard glide. Most creep data are of this type, following the precedent established by *Glen* [1955] in his pioneering study of creep in polycrystalline ice. Homogeneous flow in glaciers and ice sheets is probably mainly stable steady state creep controlled by easy glide, since the stress distribution should remain essentially constant long enough for stage 5 to be attained. However, when one homogeneous flow regime changes to another homogeneous flow regime, the grain fabric preferred by the old regime may not be suited to the new regime. In such cases, recrystallization must occur before a new grain fabric allows the new flow regime to attain stage 5 stable equilibrium. The nonhomogeneous flow regime that prevails during the transitions must pass through stage 3 unstable equilibrium where steady state creep is controlled by hard glide, as has been studied by *Glen* [1955] and most of his successors.

Stage 3 steady state strain is expected in glaciers and ice sheets whenever the stress regime changes rapidly. High stress gradients will characterize these conditions. Regions where stage 3 deformation should predominate are in surging portions of glaciers, in glacier ice falls, in active crevasse fields, around bedrock projections into moving ice, alongside ice streams, along ice dome–ice shelf junctions, where glaciers make sharp bends, and in regions of ice sheets where thermal convection is important (if it occurs at all). These are all regions of nonhomogeneous flow and are often the most interesting regions of a glacier or ice sheet.

No comprehensive theory of nonhomogeneous flow in glaciers and ice sheets exists. Classical glaciological theory assumes homogeneous flow and is adequate for all conditions controlled by stage 5 stable equilibrium. Nonhomogeneous flow is controlled by stage 3 unstable equilibrium, which is really transient strain on the verge of recrystallization. This is the essence of slow steady state strain controlled by hard glide, and this is what makes it unstable. The first steps in formulating a nonhomogeneous flow theory must begin with the ice crystals themselves, because nonhomogeneous flow is a consequence of crystal anisotropy.

Nonhomogeneous flow in ice streams occurs across the maximum-slope inflection lines on the surface, across the ice-water-rock interfaces on the bed, and across the tidal flexure zones along the sides. These are all boundary regions having high stress gradients where viscoplastic instability will be associated with stage 3 unstable equilibrium and steady state creep is controlled by hard glide. Creep controlled by hard glide results in strain hardening, as demonstrated by *Hawkes and Mellor* [1972] and illustrated by the flow curve in Figure 3. Strain hardening occurs between the elastic limit and the upper yield stress. The upper yield stress is the maximum stress of slow steady state strain controlled by hard glide, and it occurs at the strain of viscoplastic instability. Stress then decreases during strain softening until it stabilizes at the lower yield stress of fast steady state strain controlled by easy glide.

If instability in the earth's cryosphere-hydrosphere-atmosphere climatic machine is strongly influenced by ice stream instability in the marine portions of polar ice sheets, it is equally clear that ice stream instability is a manifestation of viscoplastic instability in ice crystals themselves. The next section presents a model showing how viscoplastic instability

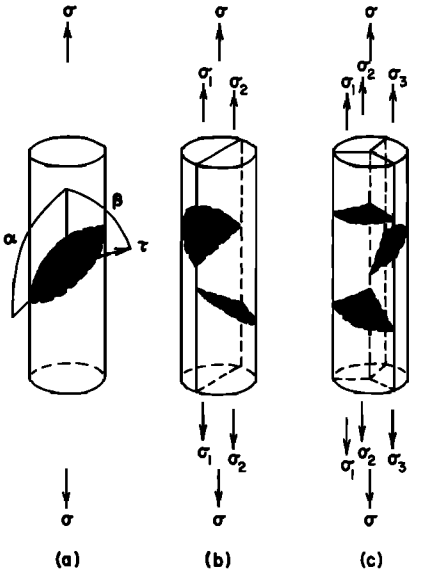

Fig. 5. (*a*) Single-crystal, (*b*) bicrystal, and (*c*) tricrystal specimens being pulled with an average uniaxial tension σ. Each crystal is loaded separately with stress σ_i, where $i = 1, 2, 3$. The angles between the tensile axis and the slip plane and slip direction are α and β, respectively, where τ is the shear stress resolved on the slip plane and in the slip direction. The dominant slip planes of the various crystals are shaded.

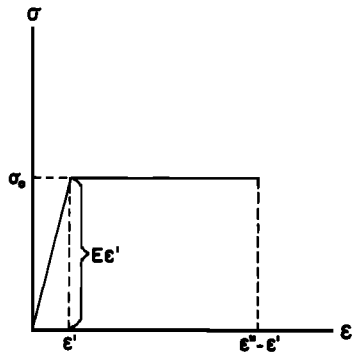

Fig. 6. The perfect elastic-plastic uniaxial flow curve for the single crystal loaded in Figure 5*a*. In this curve and subsequent uniaxial flow curves, σ is the uniaxial applied stress, ϵ is the uniaxial uniform strain, ϵ' and ϵ'' are elastic and plastic uniaxial strains, σ_0 is the uniaxial yield point, and E is the elastic modulus.

might develop in ice crystal aggregates. Table 3 summarizes equilibrium conditions in the climatic machine, in its ice sheet cryosphere component, and in the deformation of glacial ice.

Viscoplastic instability associated with the maximum slope surface inflection lines bordering an ice stream is triggered by the boundary conditions of the ice dome–ice stream–ice shelf dynamic system. Coastal mountain ranges typically fringe continents, so flow from continental ice domes terminating at the ocean must pass through these mountains. Sheetflow is therefore largely transformed to streamflow near the coast. Streamflow focuses the energy of the ice dome at discrete points along its margin, creating outlet glaciers which erode fjords through the mountains and ice streams which erode troughs on the continental shelf beyond the mountains. Therefore streamflow begins as outlet glaciers through coastal mountains and ends as ice streams across the continental shelf. These ice streams are also supplied by sheetflow from marine ice domes on the continental shelves. However, many West Antarctic ice streams are supplied wholly by West Antarctic marine ice domes. These ice streams share with East Antarctic outlet glaciers passing through the Transantarctic Mountains the critical role of focusing flow at the base where concentrated erosion makes ice streams possible, but the focusing role of topography for ice streams beginning as outlet glaciers is not obvious for ice streams that begin in a marine ice dome on the continental shelf [*Weertman*, 1976].

Like outlet glacier fjords, ice stream troughs are foredeepened by glacial erosion so that a low bedrock sill usually exists at the outer margin of the continental shelf where ice streams became afloat and merged with fringing ice shelves surrounding the expanded Antarctic ice domes during the last ice age. Rising Holocene temperatures and sea levels allowed the ice streams to punch through the ice shelf fringe and surge. The ice shelf grounding line then migrated over the sills and up the ice stream channels to the present positions shown in Figure 1.

3. A Parabolic Strain Hardening Law for Glacial Ice

a. Strain Hardening in Polycrystalline Ice

Although the creep curve (strain versus time) for ice has been studied extensively, studies of the flow curve (stress versus strain) are rare [*Weertman*, 1963]. Strain hardening is a feature of the flow curve which has received very little attention. *Hawkes and Mellor* [1972] observed strain hardening in randomly oriented polycrystalline ice, and *Higashi et al.* [1968] showed that strain hardening resulted from hard glide. *Weertman* [1963] cited hard glide as controlling the creep behavior of randomly oriented polycrystalline ice. Therefore the creep curve for this ice is a result of strain hardening.

Stresses built up in a grain by dislocations are relieved when the dislocations migrate across the grain boundaries into neighboring grains. Strain hardening results when this migration is obstructed. Migration is obstructed by high-angle grain boundaries between grains so anisotropic that one slip system is greatly favored over the others. Ice has this degree of anisotropy, and the basal slip system allows easy glide, whereas all other slip systems allow only hard glide. High-angle grain boundaries insure that if the shear stress resolved on the basal plane of a grain is high, it will be low on the basal planes and high on the nonbasal planes of neighboring grains. Hence hard glide will control deformation of the specimen as a whole, and strain hardening results until recrystallization occurs, as shown in Figure 4.

b. An Elastic-Plastic Strain Hardening Model for Polycrystalline Ice

Consider a single crystal of unit cross-sectional area being pulled in uniaxial tension, as shown in Figure 5. The tensile axis is inclined at angle α to the slip direction and at angle β to the slip plane. Therefore [*Dieter*, 1961, p. 99]

$$\tau = \sigma \cos \alpha \cos (90° - \beta) = \sigma \cos \alpha \sin \beta = \sigma/\Omega \quad (1)$$

where τ is the resolved shear stress and σ is the uniaxial tensile stress. Assume that elastic deformation ends and perfectly plastic deformation begins at a uniaxial yield stress σ_0, as shown in Figure 6. Total uniaxial strain ϵ has an elastic component ϵ' and a plastic component ϵ''. For convenience the elastic modulus E will be considered independent of Ω; however, see the work by *Nye* [1960*b*] for the effect of crystal symmetry on the elastic stiffness constants. Before yielding,

$$\sigma = E\epsilon' = E\epsilon \quad (2)$$

After yielding,

$$\sigma = \sigma_0 \quad (3)$$

Consider a bicrystal being pulled in uniaxial tension as shown in Figure 5. Each crystal has unit cross-sectional area

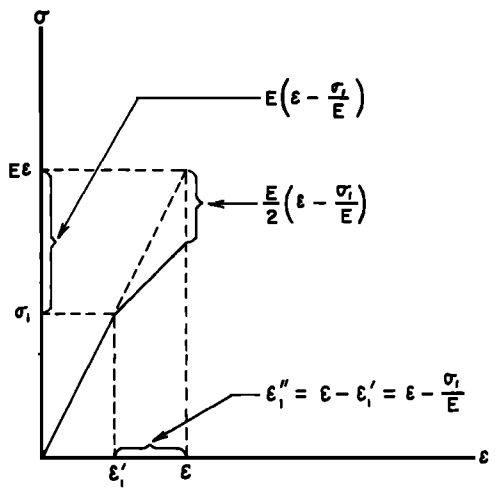

Fig. 7. The perfect elastic-plastic uniaxial flow curve for the bicrystal loaded in Figure 5*b* after crystal 1 has yielded but before crystal 2 has yielded.

normal to the tensile axis with $\Omega_1 < \Omega_2$, where subscript 1 refers to crystal 1 and subscript 2 refers to crystal 2. A given Ω' is referred to the slip system which yields first in each crystal, and this depends on both the value of Ω and the value of σ_0 for a given slip system. Separate uniaxial tensile loads are simultaneously applied to each crystal, so that the uniaxial tensile stress σ applied to the bicrystal is

$$\sigma = \tfrac{1}{2}(\sigma_1 + \sigma_2) \tag{4}$$

where σ_1 and σ_2 are tensile stresses in crystals 1 and 2. The grain boundary connecting crystals 1 and 2 causes the two crystals to deform equally when σ is applied. The uniaxial strain acting on the bicrystal is therefore

$$\epsilon = \epsilon_1 = \epsilon_2 \tag{5}$$

where ϵ_1 and ϵ_2 are tensile strains in crystals 1 and 2.

As σ increases, σ_1 and σ_2 also increase. However, $\Omega_2 > \Omega_1$, so $\sigma_1 = \sigma_0$ first, and crystal 1 will deform plastically while crystal 2 is still deforming elastically. Therefore

$$\epsilon_1 = \epsilon_1' + \epsilon_1'' = (\sigma_1/E) + \epsilon_1'' \tag{6}$$

$$\epsilon_2 = \epsilon_2' = \sigma_2/E \tag{7}$$

Combining (6) and (7) with (4) and (5) gives

$$\sigma = \tfrac{1}{2}[E(\epsilon_1 - \epsilon_1'') + E\epsilon_2] = E\epsilon - \tfrac{1}{2}E\epsilon_1'' = E\epsilon - \tfrac{1}{2}E[\epsilon - (\sigma_1/E)] \tag{8}$$

Equation (8) is plotted in Figure 7. Note the decrease in slope when $\sigma_1 = \sigma_0$.

As σ continues to increase, eventually $\sigma_2 = \sigma_0$, so both crystals will flow plastically. When this happens,

$$\epsilon_1 = \epsilon_1' + \epsilon_1'' = (\sigma_1/E) + \epsilon_1'' \tag{9}$$

$$\epsilon_2 = \epsilon_2' + \epsilon_2'' = (\sigma_2/E) + \epsilon_2'' \tag{10}$$

Combining (9) and (10) with (4) and (5) gives

$$\sigma = \tfrac{1}{2}[E(\epsilon_1 - \epsilon_1'') + E(\epsilon_2 - \epsilon_2'')] = E\epsilon - \tfrac{1}{2}E(\epsilon_1'' + \epsilon_2'') = E\epsilon - \tfrac{1}{2}E\left[\left(\epsilon - \frac{\sigma_1}{E}\right) + \left(\epsilon - \frac{\sigma_2}{E}\right)\right] \tag{11}$$

Equation (11) is plotted in Figure 8. Note that the slope becomes zero when $\sigma_2 = \sigma_0$.

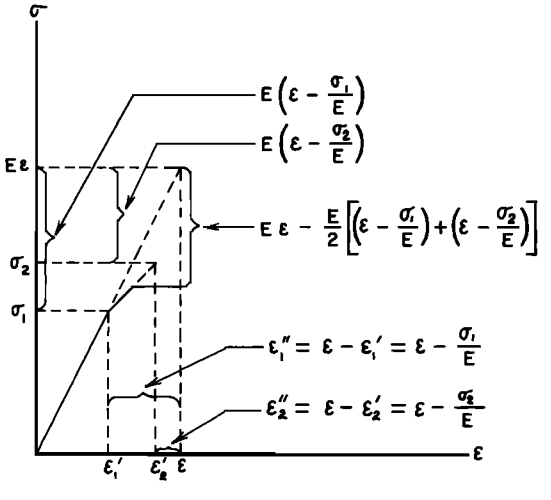

Fig. 8. The perfect elastic-plastic uniaxial flow curve for the bicrystal loaded in Figure 5*b* after crystals 1 and 2 have yielded.

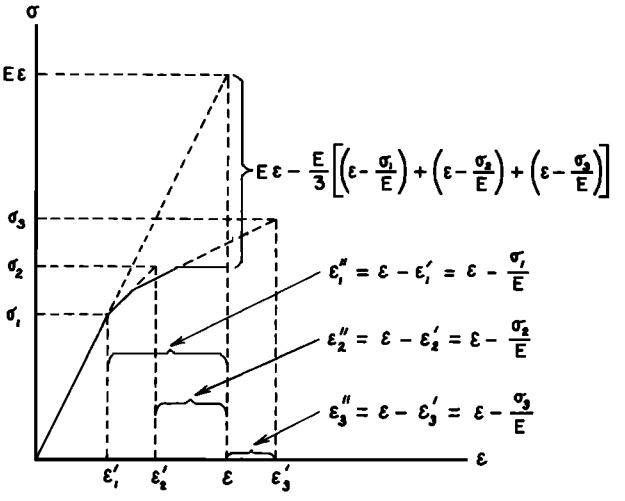

Fig. 9. The perfect elastic-plastic uniaxial flow curve for the tricrystal loaded in Figure 5*c* after all three crystals have yielded.

Consider a tricrystal being pulled in uniaxial tension as shown in Figure 5. Each crystal has unit cross-sectional area normal to the tensile axis with $\Omega_1 < \Omega_2 < \Omega_3$, where subscripts 1, 2, and 3 refer to the crystals 1, 2, and 3 in Figure 5. When each crystal is separately loaded, the stress on the tricrystal is

$$\sigma = \tfrac{1}{3}(\sigma_1 + \sigma_2 + \sigma_3) \tag{12}$$

and the strain on the tricrystal is

$$\epsilon = \epsilon_1 = \epsilon_2 = \epsilon_3 \tag{13}$$

When the first crystal yields,

$$\sigma = \tfrac{1}{3}E[(\epsilon_1 - \epsilon_1'') + \epsilon_2 + \epsilon_3] = E\epsilon - \tfrac{1}{3}E\epsilon_1'' = E\epsilon - \tfrac{1}{3}E[\epsilon - (\sigma_1/E)] \tag{14}$$

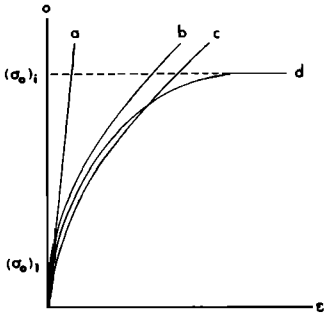

Fig. 10. Components of the flow curve for polycrystalline ice having randomly oriented grains at a constant strain rate and temperature. Shown are flow curves for (*a*) elastic deformation described by (2), (*b*) parabolic strain hardening deformation described by (21), (*c*) elastic-parabolic strain hardening deformation described by adding (2) and (21), and (*d*) elastic-plastic deformation described by (19) when i is very large. The viscoplastic parameter $c = 2$ in (21) results in the parabolic strain hardening law and a viscoplastic strain ϵ_v which is added to the elastic strain ϵ_e to give the total strain ϵ. Stresses $(\sigma_0)_i$ and $(\sigma_0)_f$ in elastic-plastic deformation are comparable to the proportional limit stress and the upper yield stress in elastic-viscoplastic deformation, as can be seen by comparing curve *d* with the flow curve in Figure 2. Hence the parabolic strain hardening law is useful until viscoplastic instability results in strain softening.

When the second crystal yields,

$$\sigma = \tfrac{1}{2}E[(\epsilon_1 - \epsilon_1'') + (\epsilon_2 - \epsilon_2'') + \epsilon_3]$$
$$= E\epsilon - \tfrac{1}{2}E\left[\left(\epsilon - \frac{\sigma_1}{E}\right) + \left(\epsilon - \frac{\sigma_2}{E}\right)\right] \quad (15)$$

When the third crystal yields,

$$\sigma = \tfrac{1}{3}E[(\epsilon_1 - \epsilon_2'') + (\epsilon_2 - \epsilon_2'') + (\epsilon_3 - \epsilon_3'')]$$
$$= E\epsilon - \frac{E}{3}\left[\left(\epsilon - \frac{\sigma_1}{E}\right) + \left(\epsilon - \frac{\sigma_2}{E}\right) + \left(\epsilon - \frac{\sigma_3}{E}\right)\right] \quad (16)$$

Equations (14), (15), and (16) are plotted in Figure 9. Note that the first decrease in slope occurs when $\sigma_1 = \sigma_0$, the second decrease in slope occurs when $\sigma_2 = \sigma_0$, and the third decrease to zero slope occurs when $\sigma_3 = \sigma_0$.

Each crystal of the bicrystal and tricrystal specimens was oriented and loaded as shown in Figure 5 to illustrate how the stress-strain curve for polycrystalline specimens can be understood in terms of successive yielding of individual crystals. Consider a polycrystalline material consisting of i crystals and loaded so that $\Omega_1 < \Omega_2 < \Omega_3 < \cdots < \Omega_i$. Each crystal will experience a different principal tensile stress because the load is transmitted to it through other crystals which respond differently to the load. If the applied stress is averaged over all the crystals in the specimens,

$$\sigma = i^{-1}(\sigma_1 + \sigma_2 + \sigma_3 + \cdots + \sigma_i) = i^{-1}\sum_i \sigma_i \quad (17)$$

If interlocking grain boundaries insure uniform strain in each crystal,

$$\epsilon = \epsilon_1 = \epsilon_2 = \epsilon_3 = \epsilon_i \quad (18)$$

When yielding has occurred in all the crystals,

$$\sigma = E\epsilon - \frac{E}{i}$$
$$\cdot\left[\left(\epsilon - \frac{\sigma_1}{E}\right) + \left(\epsilon - \frac{\sigma_2}{E}\right) + \left(\epsilon - \frac{\sigma_3}{E}\right) + \cdots + \left(\epsilon - \frac{\sigma_i}{E}\right)\right]$$
$$= E\epsilon - Ei^{-1}\sum_i\left(\epsilon - \frac{\sigma_i}{E}\right) = i^{-1}\sum_i \sigma_i \quad (19)$$

If E varies with Ω, then (19) becomes

$$\sigma = (E_1\epsilon + E_2\epsilon + E_3\epsilon + \cdots + E_i\epsilon)i^{-1} - i^{-1}E_i\left[\left(\epsilon - \frac{\sigma_1}{E_1}\right)\right.$$
$$\left. + E_2\left(\epsilon - \frac{\sigma_2}{E_2}\right) + E_3\left(\epsilon - \frac{\sigma_3}{E_2}\right) + \cdots + E_i\left(\epsilon - \frac{\sigma_i}{E_i}\right)\right]$$
$$= i^{-1}\sum_i E_i\epsilon - i^{-1}\sum_i E_i\left(\epsilon - \frac{\sigma_i}{E_i}\right) = i^{-1}\sum_i \sigma_i \quad (20)$$

Hence both (19) and (20) reduce to (17) when $\sigma = \sigma_0$. Although the notation gets cumbersome, the geometry for plotting σ versus ϵ from (20) is similar to that for plotting σ versus ϵ from (19). For simplicity in constructing Figures 7, 8, and 9 an average E for the entire specimen was used to illustrate the qualitative trend of the stress-strain curve as i increases. This qualitative behavior is unchanged if E changes with Ω.

The anticipated stress-strain curve for large i is plotted in Figure 10. When elastic strain is small so that $\epsilon \to \epsilon''$ and when viscoplastic behavior is allowed so that $d\sigma_0/d\epsilon > 0$, the curve in Figure 10 can be closely approximated by the parabolic strain hardening law observed for most polycrystalline materials,

$$\epsilon = (\sigma/\sigma^*)^c \quad (21)$$

where σ^* is the strength coefficient and c is the reciprocal strain hardening coefficient [*Dieter*, 1961, pp. 245–250]. Stress-strain tests are conducted at constant temperature T and strain rate $\dot{\epsilon}$, and when $\sigma = \sigma_0$ in (21), it is often found that

$$\sigma_0{}^s = K_0\dot{\epsilon}\exp(Q/RT) \quad (22)$$

so that

$$\sigma^* = \sigma_0/\epsilon_0{}^{1/c} = [K_0\dot{\epsilon}\exp(Q/RT)]^{1/s}[E_0/\sigma_0(1-\mu^2)]^{1/c} \quad (23)$$

where K_0 is a hardness parameter, s is a yielding parameter, Q is the activation energy of self-diffusion, R is the ideal gas constant, T is absolute temperature, E_0 is Young's modulus, μ is Poisson's ratio, and

$$\epsilon_0 = \epsilon' = \sigma_0/E = \sigma_0(1-\mu^2)/E_0 \quad (24)$$

is the total strain at σ_0.

If the bicrystal and tricrystal analyses are continued for more crystals, they lead to an approximation of the empirical parabolic strain hardening law when i becomes sufficiently large. This suggests that (17) and (18) are not unreasonable, even though their validity is assumed. *Boas and Hargreaves* [1948] found that the crystals in a polycrystalline specimen experience stresses higher or lower than the externally applied stress and that deformation per crystal becomes more uniform as crystal size decreases. Hence (17) seems reasonable, and (18) becomes a better approximation as crystal size decreases. Within limits it seems that single crystal yielding data can be used to predict approximate parabolic strain hardening in polycrystalline materials.

c. *Combining the Flow and Creep Curves for Ice*

Higashi et al. [1964, 1968] and *Higashi* [1967, 1969] studied viscoplastic yielding on basal and prismatic planes for ice

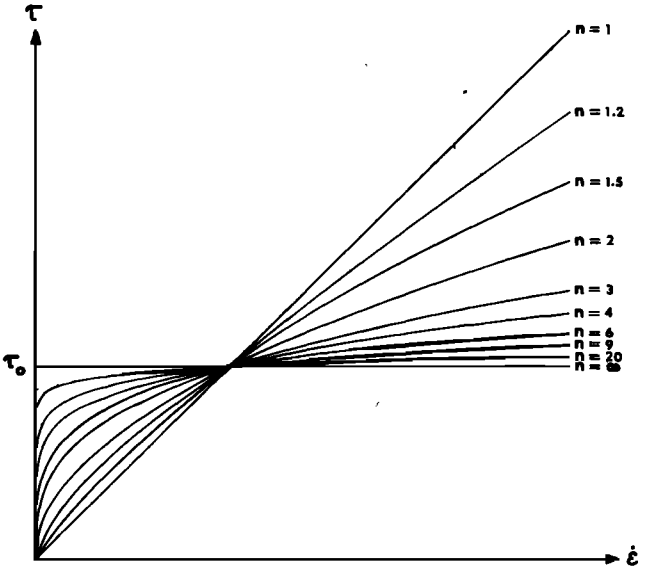

Fig. 11. The viscoplastic spectrum of creep in crystals. The creep law $\dot{\epsilon} = (\tau/A)^n$ is plotted for various values of the viscoplastic parameter n, including viscous flow ($n = 1$), glacial flow ($n = 3$), and plastic flow ($n = \infty$).

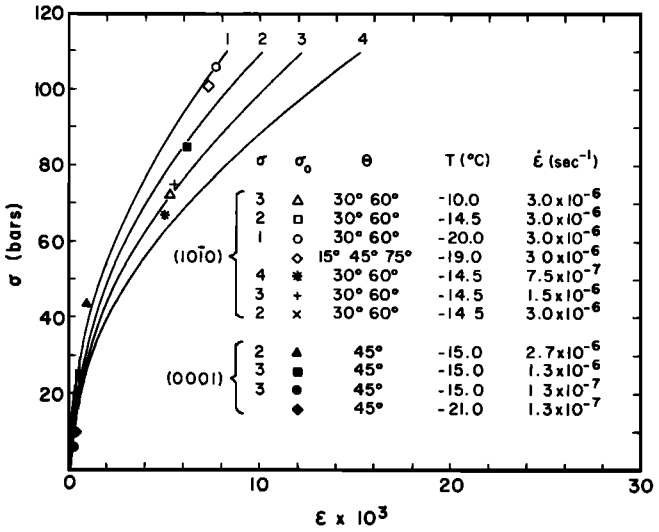

Fig. 12. Plastic yielding data for (0001) basal glide and (10$\bar{1}$0) prismatic glide in ice single crystals pulled in uniaxial tension fitted to the parabolic strain hardening law. Crystals were oriented so that only basal or prismatic slip was possible for a given specimen. Solid lines are flow curves obtained from the parabolic strain hardening law $\sigma = K^*\epsilon^{1/c}\dot{\epsilon}^{1/s} \exp(Q/sRT)$ by using $K^* = 63.2$ bars/s$^{1/s}$, $c = 2$, $s = 6.5$, and $Q = 16$ kcal/mol, where σ is the uniaxial tensile stress, ϵ is the uniaxial strain, $\dot{\epsilon}$ is the uniaxial strain rate at the yield stress, Q is the thermal activation energy for flow, R is the ideal gas constant, and T is the absolute temperature. Data points show the uniaxial yield stress σ_0 of ice single crystals for various combinations of strain rate $\dot{\epsilon}$, temperature T, and angle θ between the basal crystallographic plane and the tensile axis. These data are taken from *Higashi et al.* [1964, 1968] and *Higashi* [1967, 1969].

single crystals pulled in uniaxial tension at constant T and $\dot{\epsilon}$. The uniaxial yield stress σ_0 obeyed (22). For basal (easy) glide, $s = 1.5$ and $Q = 15.6$ kcal mol^{-1} [*Higashi et al.*, 1964], and for prismatic (hard) glide, $s = 6.5$ and $Q = 16.5$ kcal mol^{-1} [*Higashi et al.*, 1968]. In (22) the constant K_0 includes the relationship between the uniaxial stress σ and the shear stress τ resolved on the {0001} or {10$\bar{1}$0} glide planes. If θ is the angle between the tensile axis and the glide plane, where $\theta = \alpha = \beta$ is appropriate for ice [*Kamb*, 1961], this relationship is

$$\tau = (\sin\theta \cos\theta)\sigma = (\sin 2\theta)\sigma/2 \qquad (25)$$

In prismatic glide, strain hardening is greatest when θ is 30° or 60° and least when θ is 15°, 45°, or 75°, but in basal glide, strain hardening is absent [*Higashi*, 1967; *Higashi et al.*, 1968].

Rewriting (22) in terms of strain rate gives

$$\dot{\epsilon} = (\sigma_0/A_0)^s = K_0 \exp(-Q/RT)\sigma_0^s \qquad (26)$$

Equation (26) has the same form as the empirical power law relationship between σ and $\dot{\epsilon}$ commonly observed for steady state creep [*Glen*, 1955],

$$\dot{\epsilon} = (\sigma/A)^n = K \exp(-Q/RT)\sigma^n \qquad (27)$$

where K is a constant determined mainly by the relative contributions of easy glide and hard glide to creep and n is a viscoplastic parameter (see Figure 11). For perfectly viscous flow, $n = 1$ and $A = \eta$, where η is the Newtonian viscosity coefficient for uniaxial tension. For perfectly plastic flow, $n = \infty$ and $A = \sigma_0$, where σ_0 is the plastic yield stress. For ice, $n \simeq 3$ during steady state creep. Equation (25) relates σ and σ_0 in (27) to τ and τ_0 in Figure 11.

The data in Figure 12 are values of σ_0 versus ϵ for various constant values of T and $\dot{\epsilon}$. Plastic yielding data for basal glide are taken from *Higashi et al.* [1964], and plastic yielding data for prismatic glide are taken from *Higashi* [1967]. The curves in Figure 12 are plots of the parabolic strain hardening law

$$\sigma = \epsilon^{1/c}\sigma_0^* = K^*\epsilon^{1/c}\dot{\epsilon}^{1/s} \exp(Q/sRT) \qquad (28)$$

where

$$K^* = K_0^{1/s}[E_0/(1-\mu^2)\sigma_0]^{1/c} \qquad (29)$$

for the values of $\dot{\epsilon}$ and T indicated, where $K^* = 63.2$ bars s$^{1/s}$, $c = 2$, $s = 6.5$, and $Q = 16$ kcal mol^{-1}. These values give the best agreement between the σ_0 data and σ calculated from (28). Note that $s = 6.5$ approximates the perfect plasticity ($n = \infty$) assumed for the analysis which led to (21).

d. Defects and Advantages of the Model

The analysis leading to (19) and (20) has three serious flaws. First, ice is an elastic-viscoplastic material, not an elastic-plastic material, and viscoplastic instability marks the ultimate stress. Second, the uniaxial stress applied to the specimen was assumed to be transmitted as separate uniaxial stresses to each grain in the specimen on the assumption that there could be no shear stresses at the grain boundaries if all grains experienced the same uniaxial strain. However, this cannot be assumed without a detailed treatment of the compatibility conditions and the continuity equations for all three shear stresses at the grain boundaries. Third, the parallel arrangement of the differently oriented crystals does not represent the usual arrangement of polycrystalline ice (fresh sea ice is an exception). Therefore the assumption that all grains are stressed differently but strained identically is further weakened. The complexity of the problem can be better appreciated after consulting the considerable literature on the study of bicrystals, tricrystals, and polycrystals [e.g., *Kawada*, 1951; *Livingston*, 1957; *Elbaum*, 1960*a*, *b*].

In view of the above shortcomings the elastic-plastic strain hardening model presented here provides at best an incomplete description of strain hardening in polycrystalline ice. Therefore it is not surprising that (19) and (20) bear only a qualitative similarity to the empirical parabolic strain hardening law, even when the elastic component is removed, as Figure 10 demonstrates.

Despite its flaws this exercise provides three useful results. First, some insight is gained as to how crystal anisotropy causes strain hardening in randomly oriented polycrystalline ice. Second, it was shown how the flow curve could be combined with the creep curve of ice to obtain $c = 2$ in the parabolic strain hardening law. This value for c is fortunate because it permits a viscoplastic solution for certain transient creep phenomena, such as tidal flexure along an ice dome–ice shelf junction [*Hughes*, 1972*b*; *Holdsworth*, 1975]. Third, the strain hardening coefficient is the strain at which viscoplastic instability begins [*Dieter*, 1961, pp. 245–250]. This is the strain at which necking begins in a tensile test and presumably the strain at which recrystallization begins in glaciers and ice sheets. Since $c = 2$ is the reciprocal strain hardening coefficient, therefore, recrystallization begins when $\epsilon = 0.5$ in glacial ice or in laboratory creep tests on ice. This value for ice lies in the range commonly observed for the onset of viscoplastic instability in metals [*Dieter*, 1961, p. 248].

The progressive yielding criterion for polycrystalline ice developed in this section is specifically for problems in glacial deformation prior to viscoplastic instability and recrystallization. Hence the criterion should apply to elastic, transient, and slow steady state strain. These three stages of defor-

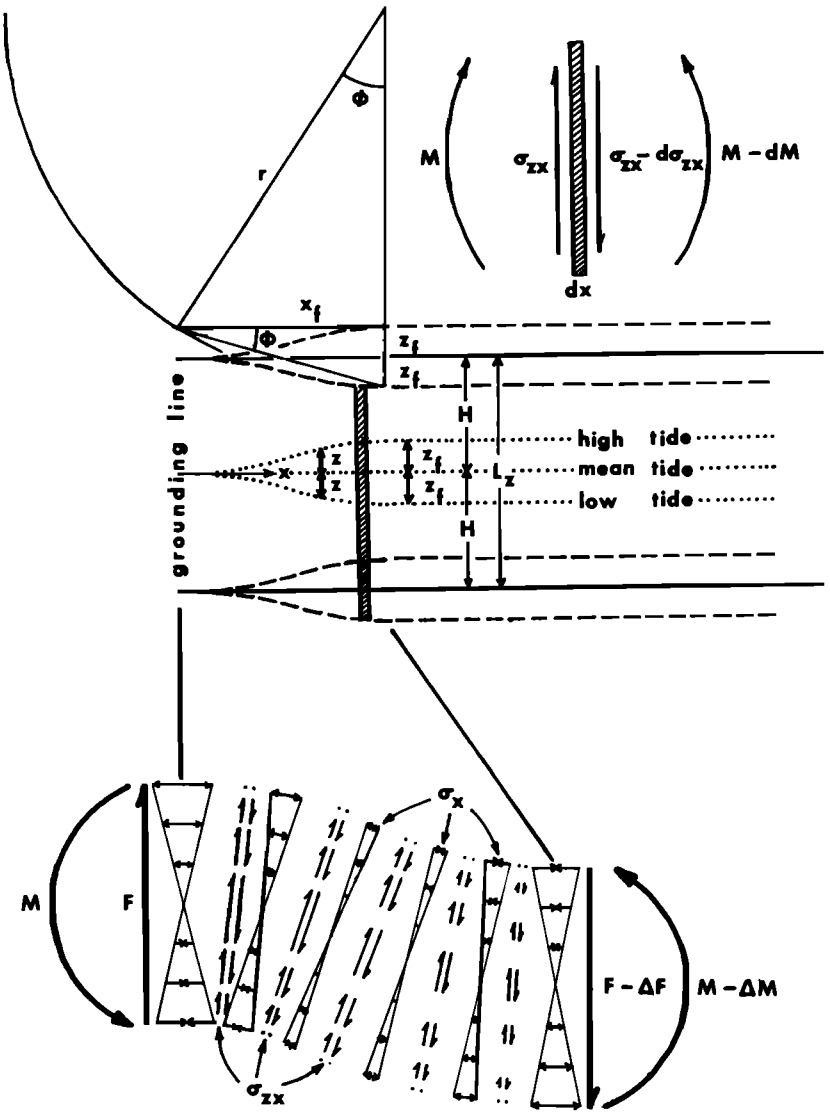

Fig. 13. A schematic longitudinal cross section of a floating glacier bent by tidal flexure. Tidal displacements are referred to reference coordinates x, z, whose origin is where the neutral axis (dotted lines) of the floating ice meets grounded ice. Tidal displacements z of the floating ice surfaces (dashed lines) from their mean tide positions (solid lines) vary along x from zero at the grounding line to z_f when the ice becomes freely floating. Tidal flexure is exaggerated to show the average radius of curvature r and angle of curvature ϕ over the longitudinal distance x_f experiencing tidal flexure. Actually, $L_z \gg z_f$, so that $\phi \simeq \sin \phi \simeq \tan \phi$. The upper right inset shows forces, stresses, and bending moments acting on an element of height L_z, length dx, and unit width according to (1), (2), and (3). The bottom enlargement shows stresses along the length $0 < x < x_f$. These stresses conform with an exponentially damped sinusoidal tidal flexure curve and consist of the shearing stress σ_{zx} due to the rise and fall of tide, which induces a shearing force F, and the longitudinal stress σ_x due to nonrotation of the ice slab for $x < 0$ and $x > x_f$, which induces a bending moment M. From the ice surfaces to the center line, σ_{zx} varies parabolically from zero to a maximum, and σ_x varies linearly from a maximum to zero, for elastic flexure. The maximum moment M_m along the length x_f where the shearing force is closest to F can be very crudely approximated by $M_m \simeq \int_0^{x_f} F\,dx = Fx_f = 2H\sigma_{zx}x_f \simeq \int_{-H}^{+H}(H\sigma_x)\,dz = 2H^2\sigma_x$. Therefore $\sigma_{zx} \simeq \sigma_x$ when $x_f \simeq H$, where σ_{zx} and σ_x are the center line and surface values at the grounding line.

mation are important in an analysis of tidal flexure along the ice dome–ice shelf junction of an ice sheet.

4. Elastic-Viscoplastic Tidal Flexure in Ice Streams

a. Grounding Zones and Tidal Zones Where an Ice Stream Becomes Afloat

The zone between grounded and floating parts of an ice stream includes a tidal zone in which the grounding zone migrates back and forth as the tide rises and falls. The grounding zone is a region of grounding points in which the ice stream is completely aground at one end and completely afloat at the other end in a given instant of time. Hence the grounding zone may be either wider or narrower than the tidal zone. Four extremes are possible: (1) both the tidal zone and the grounding zone are wide for a shallow rough bed, (2) the tidal zone is wider than the grounding zone for a shallow smooth bed, (3) the tidal zone is narrower than the grounding zone for a steep rough bed, and (4) both the tidal zone and the grounding zone are narrow for a steep smooth bed. Several analyses are necessary to determine the precise nature of these zones for a particular ice stream: photo interpretation of surface crevasse patterns, gravimetric recording of tidal amplitudes, tiltmeter

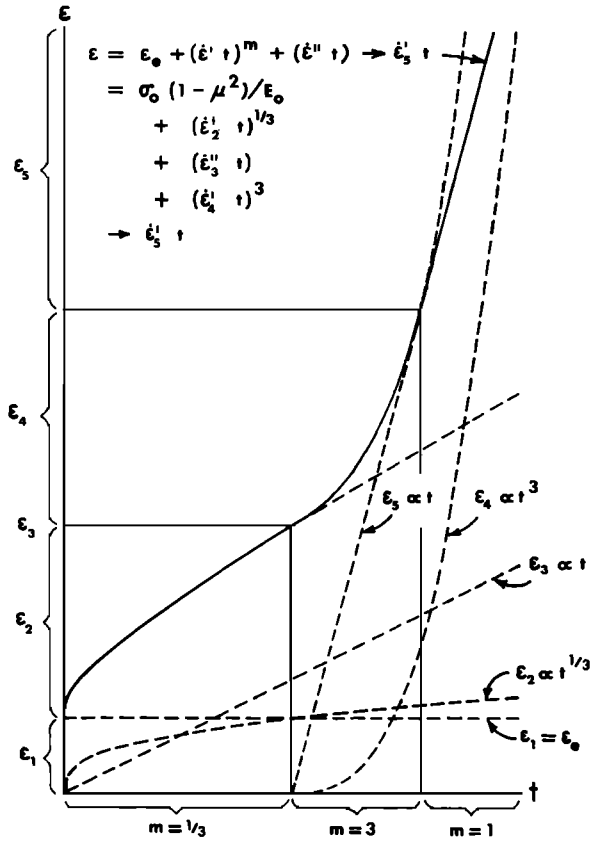

Fig. 14. The creep curve of ice. Total creep strain ϵ is the sum of stage 1 elastic strain ϵ_1, stage 2 transient strain ϵ_2, stage 3 slow steady state strain ϵ_3, and stage 4 transitional strain ϵ_4, which stabilizes to give stage 5 fast steady state strain ϵ_5. Constants $\dot{\epsilon}_1'$, $\dot{\epsilon}_2'$, $\dot{\epsilon}_3'$, $\dot{\epsilon}_4'$, and $\dot{\epsilon}_5'$ have dimensions of strain rate and are proportional to σ^3 for the viscoplastic parameter $n = 3$. Therefore the strain is $\epsilon = \epsilon_1 + \epsilon_2 + \epsilon_3 + \epsilon_4 \rightarrow \epsilon_5 = a\sigma + bt^{1/3}\sigma + ct\sigma^3 + dt^3\sigma^9 \rightarrow et\sigma^3$, and the strain rate is $\dot{\epsilon} = \dot{\epsilon}_1 + \dot{\epsilon}_2 + \dot{\epsilon}_3 + \dot{\epsilon}_4 \rightarrow \dot{\epsilon}_5 = \frac{1}{3}bt^{-2/3}\sigma + c\sigma^3 + 3dt^2\sigma^9 \rightarrow e\sigma^3$, where a, b, c, d, and e are constants.

measurements of tidal bending, radar and seismic sounding for basal ice-rock coupling, monitoring of icequake activity, surface leveling, and surface strain nets. All of these analyses can then be interpreted and correlated to provide a physical and statistical description of both the tidal zone and the grounding zone, their relative widths, and the nature of bed contact during a complete tidal cycle. On the basis of this information, one or more deep drill sites can be chosen for a physical probe of the vertical dimension of the ice stream–ice shelf junction.

A one-dimensional analysis of tidal flexure cracks on the top and bottom surfaces of an ice stream which becomes afloat will be based on five assumptions.

1. The floating ice is rectangular in plane and profile, with length and width greatly exceeding thickness.
2. The floating ice rises and falls freely with the tide at distances far from the grounding zone.
3. The grounding zone does not migrate back and forth with the rise and fall of tide and is narrow enough to be treated as a line.
4. Uniaxial longitudinal tidal strain varies linearly with vertical distance from the neutral axis of the floating ice.
5. Vertical tidal displacements are very small in comparison with the dimensions of the floating ice.

Figure 13 shows the effect of tidal flexure near an ice stream grounding line where tidal amplitude is greatly exaggerated for purposes of illustration. The x axis is horizontal and normal to the grounding line, the y axis is horizontal and parallel to the grounding line, the z axis is vertical, and the origin of these axes is located on the neutral axis of the floating ice above the grounding line. Assuming constant elastic-viscoplastic properties, the neutral axis is at the midpoint through the floating ice.

When assumption 1 is used, the floating ice has constant dimensions of length L_x, width L_y, and thickness L_z, where $L_x \gg L_z \ll L_y$. Consider the vertical forces on a longitudinal cross-sectional element of length Δx, unit width, and thickness $L_z = 2H$, located at distance x from the grounding line (see Figure 13). When assumptions 2 and 3 are used, a net vertical shear stress σ_{zx} varies along x as an ebb tide lowers the floating ice or a flood tide raises the floating ice. Since the grounding line is a rigid boundary with respect to vertical displacements, σ_{zx} resists tidal flexure of the ice slab between $x = 0$ at the grounding line and $x = x_f$ where the slab first becomes freely floating. Analytically,

$$\sigma_{zx} = \int_{-H}^{+H} \frac{\partial \sigma_{xz}}{\partial x}\, dz = P_i - P_w = k(z_f - z) = \rho_w g(z_f - z) \quad (30)$$

where P_i is the downward load pressure of the ice slab, P_w is the upward water pressure available at point x to support the ice, $(z_f - z)$ is the vertical displacement of the neutral axis of the ice slab at point x from its position z_f at point x_f, $k = \rho_w g$ is the elastic modulus of the water supporting the freely floating part of the ice slab, ρ_w is the water density, and g is the acceleration of gravity. Note that x_f varies from zero at mean tide to a maximum at flood or ebb tide, and z_f is the rise or fall of sea level from its position at mean tide.

The variation of σ_{zx} with x results in a shearing force F and a bending moment M, which vary with x for $0 \le x \le x_f$. If the vertical forces acting on the ice slab element in Figure 13 are summed,

$$F - (F + dF) + \sigma_{zx}\, dx = 0 \quad (31)$$

Combining (30) and (31) gives

$$\sigma_{zx} = dF/dx = \rho_w g(z_f - z) = d^2M/dx^2 \quad (32)$$

where σ_{zx} is the shearing stress acting on an area element of length dx and unit width and $F = dM/dx$ by definition.

b. Relating Tidal Flexure to an Elastic-Viscoplastic Flow Law

Tidal flexure consists of an instantaneous elastic deformation accompanied by a time-dependent viscoplastic deformation. These two deformation types can be described by the following expression relating strain ϵ to stress σ for randomly oriented polycrystalline ice [*Hughes*, 1972*b*]:

$$\epsilon = (\sigma/\sigma^*)^c \quad (33)$$

For an elastic response to flexure, $c = 1$, and from (23) and (24),

$$\sigma^* = \sigma_e{}^* = E_0/(1 - \mu^2) \quad (34)$$

where E_0 is Young's modulus and μ is Poisson's ratio. For a viscoplastic response to tidal flexure, $c = 2$, and from (23) and (27),

$$\sigma^* = \sigma_v{}^* = A\dot{\epsilon}^{1/n} \quad (35)$$

where A and n reflect degrees of ductility and viscoplasticity, respectively.

According to Figure 14, the total strain ϵ prior to recrys-

tallization consists of an elastic component ϵ_e and two viscoplastic components, namely, a transient component ϵ_t and a steady state component ϵ_s:

$$\epsilon = \epsilon_e + \epsilon_t + \epsilon_s = \epsilon_e + (\dot{\epsilon}'t)^m + \dot{\epsilon}''t \tag{36}$$

where t is time, $\dot{\epsilon}'$ is a transient creep constant and $\dot{\epsilon}''$ is a steady state creep constant, both having the dimensions of strain rate, and m is a constant determined by the relative contributions of easy glide (basal shear) and hard glide (nonbasal shear) to creep. Differentiating (36) gives the total viscoplastic strain rate $\dot{\epsilon}_v$:

$$\dot{\epsilon}_v = mt^{m-1}\dot{\epsilon}'^m + \dot{\epsilon}'' + mt^m\dot{\epsilon}'^{m-1}\ddot{\epsilon}' + t\ddot{\epsilon}'' \simeq mt^{m-1}\dot{\epsilon}'^m + \dot{\epsilon}'' \tag{37}$$

where $\dot{\epsilon} = d\epsilon/dt$, $\ddot{\epsilon} = d^2\epsilon/dt^2$, and the $\ddot{\epsilon}$ terms are nil. Assume that the *Glen* [1955] viscoplastic flow law for ice applies for both transient and steady state creep, and let $A = \sigma_0/\dot{\epsilon}_T^{1/n}$ in (27):

$$\dot{\epsilon} = \dot{\epsilon}_T(\sigma/\sigma_0)^n = \dot{\epsilon}_0 \exp(-Q/RT)(\sigma/\sigma_0)^n \tag{38}$$

where $\dot{\epsilon}_T$ is a thermally activated creep rate, σ_0 is the viscoplastic yield stress, n is a viscoplastic parameter, $\dot{\epsilon}_0$ is a constant creep rate (for a given ice fabric, texture, purity, and density), Q is the thermal activation energy for creep, R is the ideal gas constant, and T is absolute temperature. Applying (38) to both $\dot{\epsilon}'$ and $\dot{\epsilon}''$ in (37) gives

$$\dot{\epsilon}_v = mt^{m-1}[\dot{\epsilon}_0' \exp(-Q'/RT)(\sigma/\sigma_0')^n]^m + \dot{\epsilon}_0'' \exp(-Q''/RT)(\sigma/\sigma_0'')^n \tag{39}$$

where single-prime terms refer to transient creep and double-prime terms refer to steady state creep. The hard glide creep data in Figure 15 suggest that just before ice recrystallization (which changes m, $\dot{\epsilon}_0'$, $\dot{\epsilon}_0''$, σ_0', and σ_0''), (39) reduces to

$$\dot{\epsilon}_v = (K_t\sigma + K_s\sigma^3) \exp(-Q/RT) \tag{40}$$

This requires that $m = \frac{1}{3}$, $n = 3$, $Q = Q'' = Q'/3$, $K_t = \dot{\epsilon}_0'^{1/3}/3t^{2/3}\sigma_0'$, $K_s = \dot{\epsilon}_0''/\sigma_0''^3$, and $\dot{\epsilon}_t > \dot{\epsilon}_s$ until steady state equilibrium predominates at time t_e. Equating $K_t\sigma$ with $K_s\sigma^3$ in (40) gives

$$t_e = (\dot{\epsilon}_0'^{1/3}\sigma_0''^3/3\dot{\epsilon}_0''\sigma_0'\sigma^2)^{3/2} \tag{41}$$

Note that $t_e \propto \sigma^{-3}$. Using these values and solving (39) for $\dot{\epsilon} = \dot{\epsilon}_v$ during transient creep and steady state creep give σ_v^* in (35). For transient creep,

$$\sigma_v^* = (\dot{\epsilon}/K_t) \exp(Q/RT) = 3t^{2/3}\sigma_0'\dot{\epsilon}_0'^{-1/3}\dot{\epsilon} \exp(Q/RT) \tag{42}$$

For steady state creep,

$$\sigma_v^* = [(\dot{\epsilon}/K_s) \exp(Q/RT)]^{1/3} = \sigma_0''\dot{\epsilon}_0''^{-1/3}\dot{\epsilon}^{1/3} \exp(Q/3RT) \tag{43}$$

The yield stress σ_0 for viscoplastic creep obeys the relationship

$$\sigma_0^s = K_0\dot{\epsilon} \exp(Q/RT) \tag{44}$$

where $s = 1.6$ for easy glide, $s = 6.5$ for hard glide, and K_0 is a constant determined by ice fabric, texture, purity, and density [*Higashi*, 1969].

When assumption 4 is used, longitudinal strain ϵ_x varies linearly with vertical distance h from the neutral axis of floating ice. Therefore at distance x from the grounding line,

$$\epsilon_x = (h/H)(\epsilon_x)_H = (h/H)(H/r_x) = h/r_x \tag{45}$$

where the maximum longitudinal strain $(\epsilon_x)_H$ occurs at $h = H = L_z/2$ and r_x is the radius of curvature of the floating glacier at point x. The bending moment is obtained from (32) and (45):

$$M = \int_{-H}^{+H} \sigma_x h\, dh = \int_{-H}^{+H} \sigma^*(h/r_x)^{1/c}h\, dh = \frac{2c\sigma^*H^2}{2c+1}\left(\frac{H}{r_x}\right)^{1/c} \tag{46}$$

When assumption 5 is used, the curvature of the neutral axis of floating ice is $d^2z/dx^2 \simeq r_x^{-1}$ for small deflections. Therefore from (46),

$$\frac{d^2z}{dx^2} = \frac{1}{r_x} = \left[\frac{(2c+1)M}{2c\sigma^*H^2H^{1/c}}\right]^c = \left[\frac{(2+1/c)M}{2\sigma^*H^{(2+1/c)}}\right]^c \tag{47}$$

Differentiating twice more gives

$$\frac{d^4z}{dx^4} = \left[\frac{2+1/c}{2\sigma^*H^{(2+1/c)}}\right]^c = \left[(c-1)cM^{c-2}\left(\frac{dM}{dx}\right)^2 + cM^{c-1}\left(\frac{d^2M}{dM^2}\right)\right] \tag{48}$$

Solutions of (48) will be considered for elastic and viscoplastic deformation.

c. *Elastic Deformation During Tidal Flexure*

Setting $c = 1$ and $\sigma^* = \sigma_e^*$ for elastic deformation in (48) and combining with (32) give

$$\frac{d^4z}{dx^4} = \left[\frac{3}{2\sigma_e^*H^3}\right]\frac{d^2M}{dx^2} = \frac{3\rho_w g(z^* - z)}{2\sigma_e^*H^3} \tag{49}$$

which has a solution of the form

$$(z_f - z) = (A\cos\lambda x + B\sin\lambda x)\exp(\lambda x) + (C\cos\lambda x + D\sin\lambda x)\exp(-\lambda x) \tag{50}$$

where the elastic damping factor $\lambda = \lambda_e$ is given by the expression

$$\lambda_e^4 = \frac{1}{4}\left[\frac{3\rho_w g}{2\sigma_e^*H^3}\right] = \frac{3\rho_w g}{8\sigma_e^*H^3} \tag{51}$$

and the constants A, B, C, and D are determined by the boundary conditions. When assumption 2 is used, the region $x_f \le x \le L_x$ along which $z = z_f$ is equivalent to $x = \infty$ in (50). Hence the divergent part of (50) is zero, which means that $A = B = 0$. When assumption 2 is used at the grounding line, $z = 0$ and $dz/dx = 0$. Hence the convergent part of (50) becomes z_f, which means that $C = D = z_f$. The exact solution of (50) for these boundary conditions is therefore

$$z = z_f[1 - (\cos\lambda_e x + \sin\lambda_e x)\exp(-\lambda_e x)] \tag{52}$$

Twice differentiating (52) and combining with (47) give the longitudinal bending moment

$$M_x = \tfrac{1}{3}\sigma_e^*H^3\lambda_e^2 z_f(\cos\lambda_e x - \sin\lambda_e x)\exp(-\lambda_e x) = M_0(\cos\lambda_e x - \sin\lambda_e x)\exp(-\lambda_e x) \tag{53}$$

where M_0 is the bending moment at $x = 0$. For elastic flexure, using (34), (51), and (53) gives

$$M_0 = \tfrac{1}{3}\sigma_e^*H^3\lambda_e^2 z_f = \left[\frac{6\rho_w g H^3 z_f^2 E_0}{(1-\mu^2)}\right]^{1/2} \tag{54}$$

The surface stresses $(\sigma_x)_H$ at $h = \pm H$ are obtained from (33), (34), (45), (47), (51), and (53):

$$(\sigma_x)_H = \sigma_e^*(\epsilon_x)_H = \sigma_e^* H(d^2z/dx^2)$$

$$= 2\sigma_e^* H\lambda_e^2 z_f(\cos \lambda_e x - \sin \lambda_e x) \exp(-\lambda_e x)$$

$$= \left[\frac{3\rho_w g z_f^2 E_0}{2H(1-\mu^2)}\right]^{1/2} (\cos \lambda_e x - \sin \lambda_e x) \exp(-\lambda_e x) \quad (55)$$

This solution follows directly from the analysis by *Hetényi* [1946] and has been applied to floating ice shelves by *Robin* [1958] and to floating ice tongues by *Holdsworth* [1969].

d. Viscoplastic Deformation During Tidal Flexure

Setting $c = 2$ and $\sigma^* = \sigma_v^*$ for viscoplastic deformation in (48) gives

$$\frac{d^4z}{dx^4} = \left[\frac{5}{4\sigma_v^* H^{5/2}}\right]^2 \left[2\left(\frac{dM}{dx}\right)^2 + 2M\left(\frac{d^2M}{dx^2}\right)\right] \quad (56)$$

Equation (32) shows that d^2M/dx^2 varies linearly with z, so that the variation of dM/dx, M, and $(dM/dx)^2$ with z contains terms in z^2, z^3, and z^4, respectively. Hence (56) cannot be integrated to give the variation of z with x, as was done for elastic deformation with $c = 1$.

Approximate solutions for viscoplastic deformation are possible if certain assumptions are made. *Holdsworth* [1969] suggested that the bending moment for elastic deformation given by (53) could be used to approximate the early stages of viscoplastic deformation. This suggestion was the basis of an attempted viscoplastic solution based on (32) with $c = 2$ and $\sigma^* = \sigma_v^*$, but the effort was inconclusive [*Hughes*, 1972*b*]. Later, *Holdsworth* [1975] used (32) with $c = 2$ and $\sigma^* = \sigma_v^*$ to obtain a bending moment based on the assumption that the elastic displacement curve given by (52) has the same form for the transient creep stage of viscoplastic deformation. This assumption led to separate equations describing the variation of stress with x for elastic and viscoplastic deformation.

An alternative approach is to assume that the stress levels given by (55) for elastic deformation cause different amounts of elastic strain ϵ_e and viscoplastic strain ϵ_v, as suggested by Figure 10. This assumption is based on the common observation that elastic strain continues to increase linearly with stress even after viscoplastic deformation dominates, suggesting that the total strain is additive and is given by combining (32), (34), and (35):

$$\epsilon = \epsilon_e + \epsilon_v = (\sigma/\sigma_e^*) + (\sigma/\sigma_v^*)^2 \quad (57)$$

Since (55) gives the stress causing both ϵ_e and ϵ_v, the viscoplastic strain at $h = H$, assuming that ϵ_v does not greatly exceed ϵ_e, is

$$(\epsilon_v)_H = \left[\frac{3\rho_w g z_f^2 E}{2H(1-\mu^2)\sigma_v^{*2}}\right](\cos \lambda_e x - \sin \lambda_e x)^2 \exp(-2\lambda_e x) \quad (58)$$

Since $\epsilon_x = H/r_x = H\, d^2z/dx^2$, the displacement curve for viscoplastic deformation is obtained from the equation

$$\frac{d^2z}{dx^2} = \frac{(\epsilon_v)_H}{H} = \left[\frac{3\rho_w g z_f^2 E}{2H^2(1-\mu^2)\sigma_v^{*2}}\right](\cos \lambda_e x - \sin \lambda_e x)^2 \exp(-2\lambda_e x) \quad (59)$$

A solution of (59) is

$$z = z_f[(2 - \cos 2\lambda_e x) \exp(-2\lambda_e x) - 1] \quad (60)$$

where, when (34) and (51) are used,

$$z_f = \frac{4^2\lambda_e^2 H^2(1-\mu^2)\sigma_v^{*2}}{3\rho_w g E} = \left[\frac{32H\sigma_v^{*4}}{3\rho_w g \sigma_e^{*3}}\right]^{1/2} \quad (61)$$

Average values of $\langle\dot{\epsilon}\rangle$ at $x = 0$ during time t since mean tide are obtained from (45), (47), and (58):

$$\langle\dot{\epsilon}\rangle = \frac{H}{tr_x} = \frac{H}{t}\frac{d^2z}{dx^2} = \frac{3\sigma_e^*\rho_w g z_f^2}{2\sigma_v^{*2}Ht} \simeq \frac{3\rho_w g z_f^2}{2\sigma_v^* Ht} \quad (62)$$

assuming $\sigma_e^* \simeq \sigma_v^*$. Combining (62) with (42) and solving for $\langle\dot{\epsilon}_t\rangle = \langle\dot{\epsilon}\rangle \simeq \dot{\epsilon}$ when transient creep dominates at $t < t_e$ give

$$\langle\dot{\epsilon}\rangle_t = \left[\frac{E\rho_w g z_f^2 \dot{\epsilon}_0'^{2/3}}{6(1-\mu^2)H\sigma_0'^2 t^{7/3} \exp(2Q/RT)}\right]^{1/3}$$

$$\simeq \left[\frac{\rho_w g z_f^2 \dot{\epsilon}_0'^{1/3}}{2H\sigma_0' t^{5/3} \exp(Q/RT)}\right]^{1/2} \quad (63)$$

Combining (62) with (43) and solving for $\langle\dot{\epsilon}\rangle_s = \langle\dot{\epsilon}\rangle \simeq \dot{\epsilon}$ when steady state creep dominates at $t > t_e$ give

$$\langle\dot{\epsilon}\rangle_s = \left[\frac{3E\rho_w g z_f^2 \dot{\epsilon}_0''^{2/3}}{2(1-\mu^2)H\sigma_0''^2 t \exp(2Q/3RT)}\right]^{3/5}$$

$$\simeq \left[\frac{3\rho_w g z_f^2 \dot{\epsilon}_0''^{1/3}}{2H\sigma_0'' t \exp(Q/3RT)}\right]^{3/4} \quad (64)$$

Equation (36) suggests a means for estimating average tidal flexure strains. In the transient creep range ($t < t_e$),

$$\langle\epsilon\rangle_t = (\langle\dot{\epsilon}\rangle_t t)^{1/3} \simeq (\langle\dot{\epsilon}\rangle_t t^{5/6})^{1/3} = \left[\frac{\rho_w g z_f^2 \dot{\epsilon}_0'^{1/3}}{2H\sigma_0' \exp(Q/RT)}\right]^{1/6} \quad (65)$$

In the steady state creep range ($t > t_e$),

$$\langle\epsilon\rangle_s = \langle\dot{\epsilon}\rangle_s t \simeq \langle\dot{\epsilon}\rangle_s t^{3/4} = \left[\frac{3\rho_w g z_f^2 \dot{\epsilon}_0''^{1/3}}{2H\sigma_0'' \exp(Q/3RT)}\right]^{3/4} \quad (66)$$

Hence tidal flexure strain depends on the tidal amplitude and the temperature, thickness, density, and viscoplastic properties of ice for both transient and steady state creep.

A comparison between the above approach based on (57) and the *Holdsworth* [1975] approach based on (52) with λ_v substituted for λ_e requires separating transient and steady state strain regimes. If the viscoplastic displacement curve caused by tidal flexure has the same form as the elastic displacement curve given by (52) except that a viscoplastic damping factor λ_v replaces λ_e, then

$$z = z_f[1 - (\cos \lambda_v x + \sin \lambda_v x) \exp(-\lambda_v x)] \quad (67)$$

An equation for the viscoplastic curvature of the floating ice when $\lambda_v \simeq \lambda_e$ is obtained by twice differentiating (67) and equating it with (47):

$$\frac{d^2z}{dx^2} = 2z_f\lambda_v^2(\cos \lambda_v x - \sin \lambda_v x) \exp(-\lambda_v x)$$

$$= \left[\frac{(2 + 1/c)M}{2\sigma^* H^{2+1/c}}\right]^c \quad (68)$$

Setting $c = 2$ and solving for M in (68) give the viscoplastic bending moment

$$M_x = M_0 (\cos \lambda_v x - \sin \lambda_v x)^{1/2} \exp(-\tfrac{1}{2}\lambda_v x) \quad (69)$$

where the sign of M_x is the sign of the term $(\cos \lambda_v x - \sin \lambda_v x)$ and the viscoplastic bending moment at $x = 0$ is

$$M_0 = [4(2)^{1/2}/5]\sigma^* H^{5/2} \lambda_v z_f^{1/2} \quad (70)$$

The difference between the elastic and viscoplastic bending moments is seen by comparing (53) and (54) with (69) and (70).

The viscoplastic surface stresses $(\sigma_x)_H$ at $h = \pm H$ are obtained from (33), (35), (42), (43), and (68):

$$(\sigma_x)_H = \sigma_v^*(\epsilon_x)_H^{1/2} = \sigma_v^*(H/r_x)^{1/2} = \sigma_v^*(Hd^2z/dx^2)^{1/2}$$

$$= 2^{1/2}\sigma_v^* H^{1/2}\lambda_v z_f^{1/2} (\cos \lambda_v x - \sin \lambda_v x)^{1/2} \exp(-\tfrac{1}{2}\lambda_v x)$$

$$= \left[\frac{3(2)^{1/2} H^{1/2} \lambda_v z_f^{1/2} \sigma_0'}{\dot{\epsilon}_0'^{1/3} \exp(-Q/RT)}\right] t^{2/3} \dot{\epsilon}_t' (\cos \lambda_v x$$

$$- \sin \lambda_v x)^{1/2} \exp(-\tfrac{1}{2}\lambda_v x) \quad (71)$$

Note that the time-independent surface stress for elastic tidal flexure given by (55) must be added to the time-dependent surface stress for viscoplastic tidal flexure given by (71), since $\lambda_v = \lambda_e$ at $t = 0$. An approximate expression for the time dependence of λ_v is obtained from (51) by setting $\lambda_e = \lambda_v$ and $\sigma_e^* = \sigma_v^*$, where σ_v^* is given by (42) and (43), and letting t be the time since tidal flexure starts. Tidal flexure begins as transient creep, with $t = 0$ at mean tide. Transient creep prevails for $t < t_e$ in (41), and (42) and (51) predict that

$$\lambda_v \simeq \left[\frac{3\rho_w g}{8\sigma_v^* H^3}\right]^{1/4} = \left[\frac{\rho_w g \dot{\epsilon}_0'^{1/3} \exp(-Q/RT)}{8H^3 \sigma_0' t^{2/3} \dot{\epsilon}}\right]^{1/4} \quad (72)$$

Steady state creep prevails for $t > t_e$ in (41), and (43) and (51) predict that

$$\lambda_v \simeq \left[\frac{3\rho_w g}{8\sigma_v^* H^3}\right]^{1/4} = \left[\frac{3\rho_w g \dot{\epsilon}_0''^{1/3} \exp(Q/3RT)}{8H^3 \sigma_0''^{1/3}}\right]^{1/4} \quad (73)$$

Average values of $\langle\dot{\epsilon}\rangle$ at $x = 0$ during time t since mean tide are obtained from (55), (57), and (68):

$$\langle\dot{\epsilon}\rangle = \frac{H}{tr_x} = \frac{H}{t}\frac{d^2z}{dx^2} = \frac{2Hz_f\lambda_v^2}{t} \quad (74)$$

Combining (74) with (42) and solving for $\langle\dot{\epsilon}\rangle_t = \langle\dot{\epsilon}\rangle \simeq \dot{\epsilon}$ when transient creep dominates at $t < t_e$ give

$$\langle\dot{\epsilon}\rangle_t = \left[\frac{\rho_w g z_f^2 \dot{\epsilon}_0'^{1/3}}{2H\sigma_0' t^{2/3} \exp(Q/RT)}\right]^{1/3} \quad (75)$$

Combining (74) with (43) and solving for $\langle\dot{\epsilon}\rangle_s = \langle\dot{\epsilon}\rangle \simeq \dot{\epsilon}$ when steady state creep dominates at $t > t_e$ give

$$\langle\dot{\epsilon}\rangle_s = \left[\frac{3\rho_w g z_f^2 \dot{\epsilon}_0''^{1/3}}{2H\sigma_0'' t^2 \exp(Q/3RT)}\right]^{3/7} \quad (76)$$

Equation (36) suggests a means for estimating average tidal flexure strains. In the transient creep range ($t < t_e$),

$$\langle\epsilon\rangle_t = (\langle\dot{\epsilon}\rangle_t t)^{1/3} \simeq (\langle\dot{\epsilon}\rangle_t t^{8/9})^{1/3} = \left[\frac{\rho_w g z_f^2 \dot{\epsilon}_0'^{1/3}}{2H\sigma_0' \exp(Q/RT)}\right]^{1/9} \quad (77)$$

In the steady state creep range ($t > t_e$),

$$\langle\epsilon\rangle_s = \langle\dot{\epsilon}\rangle_s t \simeq \langle\dot{\epsilon}\rangle_s t^{6/7} = \left[\frac{3\rho_w g z_f^2 \dot{\epsilon}_0''^{1/3}}{2H\sigma_0'' \exp(Q/3RT)}\right]^{3/7} \quad (78)$$

Hence tidal flexure strain depends on tidal amplitude and the temperature, thickness, density, and viscoplastic properties of ice for both transient and steady state creep. However, the influence of these terms on tidal flexure strain is significantly less for the analysis based on (67) than for the analysis based on (57), as is seen by comparing (77) and (78) with (65) and (66).

e. Tidal Flexure of Outlet Glaciers and Ice Streams

The significance of the tidal flexure solutions based on (57) and (67) is seen from the slopes of the viscoplastic tidal flexure curves for each solution at the ice grounding line. Equation (60) is the viscoplastic tidal flexure curve derived from (57). It satisfies the boundary conditions that $z = 0$ at $x = 0$ and $|z| = |z_f|$ as $x \to \infty$, but it requires that $dz/dx = 2\lambda_e z_f \simeq 2\lambda_v z_f$ at $x = 0$. Equation (67) is the viscoplastic tidal flexure curve based on (52). It also satisfies the boundary conditions that $z = 0$ at $x = 0$ and $|z| = |z_f|$ as $x \to \infty$, but it requires that $dz/dx = 0$ at $x = 0$. This is a boundary condition for a semi-infinite elastic slab on an infinite elastic foundation, as analyzed by *Hetényi* [1946]. Hence (57) requires a hinged boundary ($dz/dx \neq 0$) at the grounding line, and (67) requires a pinned boundary ($dz/dx = 0$) at the grounding line. A hinged boundary may exist along the sides of outlet glaciers where the grounding line

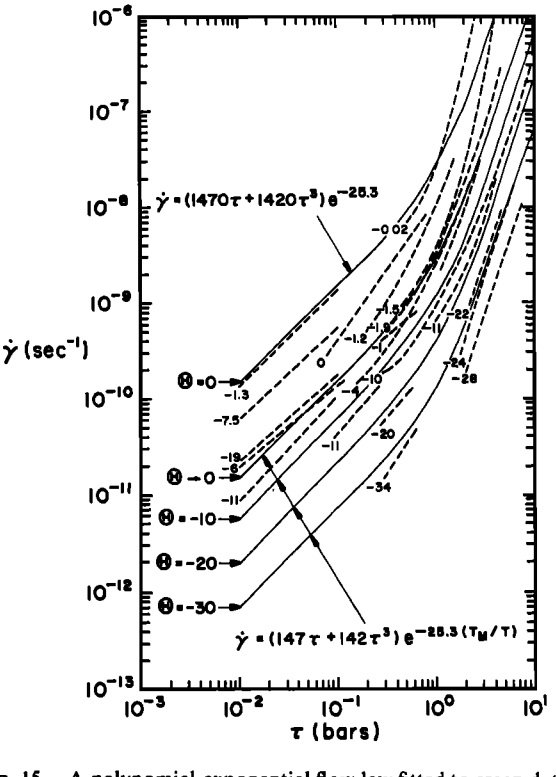

Fig. 15. A polynomial-exponential flow law fitted to creep data for polycrystalline ice having randomly oriented grains. Plotted is the variation of octahedral shear stress τ in bars versus octahedral shear strain rate $\dot{\gamma}$ in seconds at various Celsius temperatures. Dashed lines show creep data from laboratory experiments and glacier studies plotted by *Budd* [1969]. Thin solid lines give the best fit of the flow law to these data for the homologous temperature T/T_M in degrees Kelvin, corresponding to various temperatures Θ in degrees Celsius. Note that $\dot{\gamma} \propto \tau$ when $\tau < 0.5$ bar, $\dot{\gamma} \propto \tau^3$ when $\tau > 5.0$ bars, and $\dot{\gamma}$ increases tenfold as $T \to T_M$. In this paper it is assumed that the apparent viscous creep of ice at low stresses is caused by transient creep, for which $\dot{\gamma} \propto \tau/t^{2/3}$. However, it might be that steady state creep is also viscous at low stresses [*Goodman et al.*, 1975].

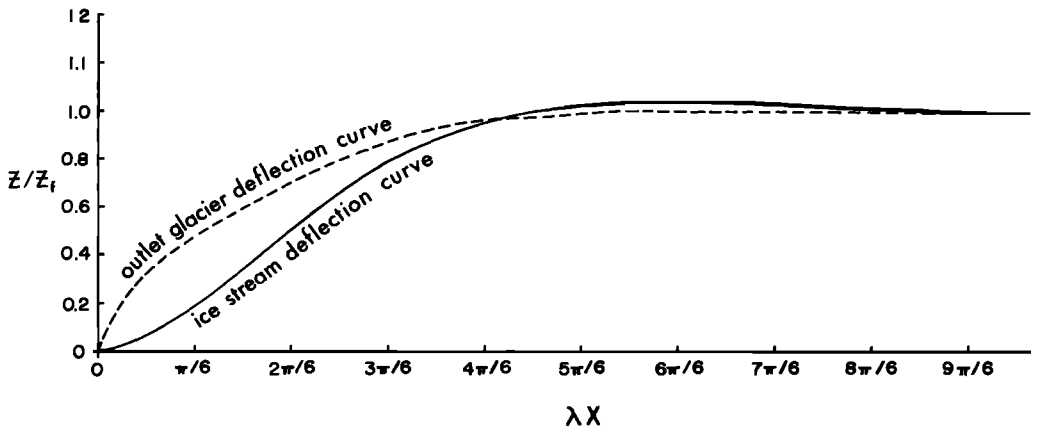

Fig. 16. Viscoplastic tidal flexure curves for the floating portions of ice streams and outlet glaciers when nontidal stresses are ignored and hard glide predominates. The normalized tidal displacement of the ice surface is plotted versus normalized distance from the grounding line by using (52) for ice streams and (59) for outlet glaciers. Vertical displacements of the floating ice from its mean tide position are z, where $z = z_f$ at maximum and minimum tide. Horizontal distance of the floating ice from its grounding line is x. The elastic-viscoplastic damping factor is λ, where $\lambda = \lambda_e$ for elastic flexure and $\lambda = \lambda_v$ for viscoplastic flexure, as described in the text. These tidal flexure curves apply to the side grounding zones, rather than the rear grounding zones, of floating ice streams and outlet glaciers.

parallels an ice-rock shear zone. A pinned boundary may exist along the sides of ice streams where the grounding line parallels an ice-ice shear zone. Therefore the analysis based on (57) may describe tidal flexure along the sides of a floating outlet glacier, and the analysis based on (67) may describe tidal flexure along the sides of a floating ice stream. When one side parallels an ice-rock shear zone and the other side parallels an ice-ice shear zone, such as Rutford Glacier in Antarctica and Jakobshavns Glacier in Greenland, (60) may describe tidal flexure along the ice-rock shear zone, and (67) may describe tidal flexure along the ice-ice shear zone. Figure 15 compares the viscoplastic tidal flexure curves for outlet glaciers and ice streams according to (60) and (67), respectively.

It remains to determine how long the tidal flexure of floating ice is dominated by transient and steady state creep during the period t_c of a tidal cycle. As an example of how this is done, consider the hinged grounding line of a floating outlet glacier. Substituting (42) for σ_v^* in (61), setting $\epsilon_0' = K_v\sigma_0'$ at the point in Figure 15 where $K_t\sigma = K_s\sigma^3$ in (40), and solving for t_e give

$$t_e = \left[\frac{\rho_w g z_f^2 \sigma_e^{*3} K_v^{4/3}}{864 H \dot{\epsilon}_t^4 \sigma_0^{8/3} \exp(4Q/RT)}\right]^{3/8} \tag{79}$$

Note that t_e must be compared to $\frac{1}{4}t_c$, which is the time from mean tide to maximum flood or ebb tide. Let $\rho_w = 1.03$ g/cm^3, $g = 9.8$ m/s^2, $z = 1$ m, $E_0 = 2.7 \times 10^4$ bars, $\mu = 0.3$, $H = 1$ km, $Q = 14$ kcal/mol, $R = 2$ cal/mol deg, and $T = 270$°K for the ice-rock-water boundary which defines the ice stream grounding line. Then (34) gives $\sigma_e^* = 3.0 \times 10^4$ bars, (51) gives $\lambda_e = 0.186$/km, and (55) gives $(\sigma_x)_H = 2.13$ bars at the junction. From Figure 16 it is clear that $z \simeq z_f$ at $\lambda_e x \simeq \pi$, giving $x_f = 17$ km. From Figure 13 the average angle of curvature ϕ can be estimated from similar triangles when ϕ is small:

$$\phi \simeq (2z_f/x_f) \simeq (x_f/r_x) \tag{80}$$

where r_x is the average radius of curvature for $0 \leq x \leq x_f$. When (45) and (80) are combined, for a tidal cycle of period t_c the mean longitudinal surface strain rate over time $\frac{1}{4}t_c$ is obtained as follows:

$$\langle\dot{\epsilon}\rangle_x = (2\langle\epsilon\rangle_x/t_c) = (2h/r_x t_c) = (4z_f h/x_f^2 t_c) \tag{81}$$

which gives $\dot{\epsilon}_x = 3.2 \times 10^{-10}$/s for $t_c = 12$ hours. When the data reported by *Higashi* [1969] are used at $T = -19$°C = 254°K and $\dot{\epsilon} = 3 \times 10^{-6}$/s, easy glide gives $\sigma_0 = 0.11$ kg/mm^2 = 10.78 bars for $s = 1.53$, $Q = 15.9$ kcal/mol, and $K_0 = 5.62 \times 10^{-5}$ bar s$^{1/s}$, and hard glide gives $\sigma_0 = 1.1$ kg/mm^2 = 107.8 bars for $s = 6.5$, $Q = 16.5$ kcal/mol, and $K_0 = 5.164$ bars s$^{1/s}$. Applying these values of s, Q, and K_0 to $T = -3$°C = 270°K and $\dot{\epsilon} = 3.2 \times 10^{-10}$/s for tidal flexure gives $\sigma_0 = 7.94 \times 10^{-3}$ bar for easy glide and $\sigma_0 = 19.6$ bars for hard glide.

Both easy glide and hard glide occur in randomly oriented polycrystalline ice. However, hard glide determines $\dot{\epsilon}$ until recrystallization results in an ice fabric oriented to favor easy glide, unless the easy glide ice fabric already exists at the grounding line. The tidal flexure strain is too low for recrystallization to occur during one tidal cycle, but it might occur over multiple tidal cycles if tidal flexure stresses dominate other stresses at the ice sheet–ice shelf junction. From Figure 15, upon converting octahedral to uniaxial strain rates and stresses, $K_v = \dot{\epsilon}_0'/\sigma_0' = (\dot{\gamma}/2^{1/2})/(3\tau/2^{1/2}) = (142/\text{bar s})/3 = 47.3$/bar s in (79) for the range of $\dot{\epsilon}$ caused by tidal flexure. It might seem that $\sigma_0 = \sigma_0'$ is the major unknown quantity in (79), since it ranges over 4 orders of magnitude, depending on the relative contributions of easy glide and hard glide to viscoplastic tidal flexure. However, (79) was derived on the assumption that hard glide controls the creep rate, so $\sigma_0 = 19.6$ bars must be used. Solving (79) for this value gives $t_e = 0.7$ hour $= 0.06t_c$. Hence viscoplastic transient creep predominates until $4 \times 6 = 24\%$ of the time has elapsed from mean tide to maximum flood or ebb tide. Steady state creep predominates over the remaining 76% of this time.

If an ice fabric favoring tidal flexure strain rates controlled by easy glide creep exists, then $m > 1$ should be used in (36), and (79) will be modified accordingly. Putting $\sigma_0 = 7.94 \times 10^{-3}$ bar in (79) gives $t_e = 1715$ hours $= 143t_c$. This means that transient creep lasts throughout the tidal cycle, which is impossible because transient creep does not occur when $m > 1$ [*Hughes*, 1975*b*]. Equation (79) cannot be modified for $m > 1$ until the value of m is determined in laboratory creep experiments for polycrystalline ice having a crystal fabric favoring creep controlled by easy glide from the start of the creep test.

Such experiments are important because an oriented crystal fabric can be expected along the side grounding lines of floating outlet glaciers and ice streams where laminar flow predominates.

Suppose that hard glide initially controls tidal flexure creep because the oriented fabric created by laminar flow along the side grounding lines does not favor easy glide from tidal flexure stresses. Then (79) is still valid. However, the question which arises is, 'How can viscoplastic creep even occur if the hard glide viscoplastic yield stress is $\sigma_0 = 19.6$ bars but the maximum tidal flexure stress is only $(\sigma_x)_H = 2.13$ bars?' The answer is that since glacial ice is polycrystalline, even if hard glide controls the tidal flexure creep rate, there will always be an easy glide component and $\sigma_0 = 7.94 \times 10^{-3}$ bar for easy glide. In fact, the parabolic strain hardening law obtained by setting $c = 2$ in (32) is satisfied most accurately for viscoplastic deformation of polycrystalline materials and requires that some viscoplastic deformation occur at all stresses, however small. This requirement is met by a 'progressive yielding' criterion in which grains best aligned for easy glide yield first and grains best aligned for hard glide yield last. If most grains have a hard glide orientation in the stress field, creep via hard glide perdominates even if initial yielding occurs in grains aligned for easy glide.

Several inadequacies in this tidal flexure analysis must be emphasized. Although the elastic solution is exact, it predicts stress levels that would cause viscoplastic deformation, thereby nullifying the elastic solution. However, exact viscoplastic solutions are impossible, and even approximate viscoplastic solutions contain ambiguities. For example, both the outlet glacier and the ice stream deflection curves (equations (60) and (67), respectively) depend on assumptions based on the elastic analysis. Equation (60) requires that $D = 2C$ in (50) but was based on an elastic stress distribution for which $D = C$. Equation (67) assumes that replacing σ_e^* for elastic deformation with σ_v^* for viscoplastic deformation in (51) gives the viscoplastic damping factor λ_v, even though (51) strictly applies only for elastic damping. Perhaps even more serious than these analytical ambiguities are defects in certain initial assumptions. The floating parts of ice streams and outlet glaciers generally have variable thicknesses where they become grounded, they become grounded across a zone rather than a line, and this zone oscillates back and forth with the rise and fall of tide. The interaction of tidal stress fields with stress fields at the tips of crevasses and stress fields associated with glacial flow was ignored, although they cause viscoplastic instability in the grounding zone. All of these rather severe restrictions were imposed to focus attention on the elastic-viscoplastic nature of tidal flexure, particularly the elastic deformation, viscoplastic yielding, transient creep, steady state creep sequence. The imposed boundary conditions most closely conform with the side grounding zones of ice streams and outlet glaciers; little or no ice moves across these zones, the zones are narrow, and tidal oscillations of the zones are small.

This analysis of tidal flexure is useful only if tidal flexure plays a significant role in ice sheet dynamics where ice streams merge with ice shelves. First, are tides significant at these junctions? *Holdsworth* [1975] presents maps showing tidal amplitudes along the margins of the Greenland and Antarctic ice sheets. Greenland tides vary from 0.5 to 5.0 m in amplitude, and Antarctic tides vary from 1.04 to 3.25 m in amplitude. These tides can be related to ocean tides in the rest of the world [*Hendershott*, 1973] and to the periodic rise and fall of floating ice shelves [*Thiel et al.*, 1960]. Of particular significance for tidal flexure analyses is the observation of *Robinson et al.* [1974] that ocean tides beneath the Ross Ice Shelf have much the same amplitude over a 630-km span from near its northern calving barrier (78°S, 162°W) to near its southern grounding line (84°S, 180°W). Hence tides are indeed significant along ice stream–ice shelf junctions. The next question is, 'What role does tidal flexure play in ice stream–ice shelf dynamics?' If Byrd Glacier is typical of an ice stream flowing at surge velocities, Figure 2 suggests that tidal flexure stresses serve to concentrate shear crevasses in a narrow zone along the fjord walls, so that these crevasses can continue as rifts that uncouple the floating ice stream from the floating ice shelf for distances up to 50 km beyond the fjord. Tidal flexure stresses are theoretically greatest along these fjord walls, as is shown by Figure 16. Hence the major role of tidal flexure stresses may be to promote shear uncoupling from the fjord walls, so that the ice stream enters the ice shelf with minimal lateral constraint. *Thiel and Ostenso* [1961] describe a band of shear crevasses confined to a shallow trough created by tidal flexure along an ice shelf grounding line [*Swithinbank*, 1955; *Robin*, 1958].

5. The Stress and Velocity Field of Ice Streams

a. *Components of Flow in Ice Streams*

Ice streams, by definition, are rapidly moving currents of ice commonly observed along the marine margins of ice sheets. They are recognized by the distinctive shear crevasse patterns that result from the high velocity gradients between ice streams and neighboring ice. Outlet glaciers are ice streams that carve fjords through mountain ranges fringing an ice dome. Ice tongues are floating ice streams and can be either freely floating or imbedded in an ice shelf. In the latter case they form thick ice lobes which supply the ice shelf [*Hughes*, 1975*a*, Figure 3]. Ice shelves maintained by the coalescing floating tongues of ice streams often form the floating fringe of a marine ice sheet grounded below sea level on a continental shelf. This is the case for the huge ice shelf fringe of the West Antarctic ice sheet.

In principle, the boundaries of an ice stream coincide with a line of maximum surface slope which circumscribes the ice stream. Following an ice flow line, this inflection maximum separates the generally convex ice dome surface from the concave surface of the grounded ice stream and separates the convex surface of the floating ice stream from the generally flat surface of the ice shelf. In practice, however, surface inflection maxima can be caused by other factors besides the velocity gradients associated with ice streams (such as surface snow drift patterns and basal topographic features). Figure 2 and Table 1 suggest that the ice stream velocity gradients giving concave and convex surfaces result from extending and compressive flow, respectively. Extending flow in the grounded portion of an ice stream results from (1) the convergence of flow lines entering the ice stream, (2) the increase of basal sliding as the ice stream becomes uncoupled from the bed, and (3) a positive mass balance resulting from snowfall along the ice stream. Compressive flow in the floating portion of an ice stream results from (1) the divergence of flow lines leaving the ice stream, (2) lateral shear between the ice stream and an ice shelf, and (3) a negative mass balance resulting from basal melting along the ice stream. An ice stream terminating as a freely floating ice tongue will experience extending flow

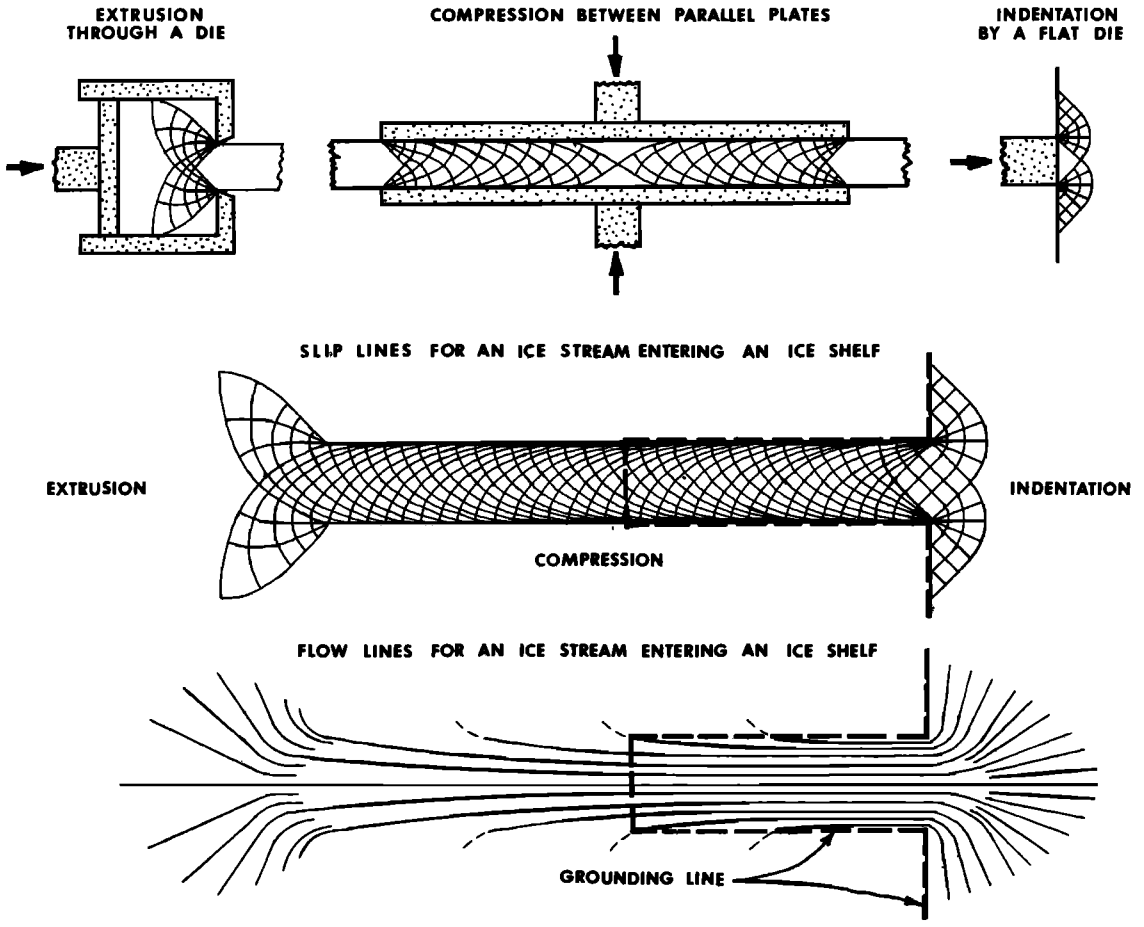

Fig. 17. A plan view of slip line and flow line fields in ice streams according to plasticity theory. Ice sheet flow converging at the head of an ice stream is analogous to extrusion of a plastic material through a rigid die. Ice sheet flow entering the sides of the ice stream is analogous to compression of a plastic slab between rigid parallel plates. Ice stream flow diverging at the foot of an ice stream into an ice shelf is analogous to indentation of a plastic plate by a rigid punch. The slip line fields for extrusion, compression, and indentation are known from plasticity theory. Joining these slip line fields gives an approximation to the orthogonal lines of maximum shear stress for an idealized ice sheet–ice stream–ice shelf complex. Ice flow lines are obtained from input velocities u_i and principal strain rates $\partial u_i/\partial x_i$ at 45° to the slip lines. The resulting flow line field shows that sheetflow becomes streamflow at the head of the ice stream and that streamflow returns to sheetflow at the foot of the ice stream. Velocity in the ice sheet–ice stream–ice shelf complex is raised by streamflow and lowered by sheetflow. If the ice shelf is narrow enough for the ice stream to punch through it, then no divergence of flow occurs, and the ice stream can increase its high velocity by discharging directly into the sea after it becomes afloat. Ice thinning accompanies acceleration of the ice stream. Ice stream thinning causes the maximum slope inflection lines defining the head and sides of the ice stream to migrate inland, thereby drawing down the ice sheet. Sea level increases as the ice sheet is drawn down, and this causes retreat of the ice shelf–ice stream grounding line. Simultaneously, transverse crevasses formed in the extending flow regime characteristic of the grounded portion of the ice stream migrate through the floating portion and section it into tabular icebergs. Therefore a calving bay develops which follows the grounding line into the heart of the ice sheet.

throughout its length because divergence is less and lateral shear is absent.

Two different driving forces cause ice stream flow. The elevation difference along an ice stream causes advective flow, which results primarily in horizontal motion. The temperature difference across an ice stream might cause convective flow, which results primarily in vertical motion. Advective flow certainly occurs. Convective flow is still speculative, but if it does occur, it would be a primary mechanism for decoupling an ice stream from the bed. Both types will be treated.

b. Slip Line Fields for Advective Flow in Ice Streams

Advective flow in an ice sheet is horizontal spreading from the center to the edge of the ice sheet. Marine ice sheets typically have an ice shelf fringe, with advective flow generally diverging from ice domes, converging on ice streams, and diverging onto the ice shelf. Ice streams, therefore, discharge most of the ice connecting the ice domes to the fringing ice shelves. For example, consider ice flowing down the west slope of the West Antarctic ice divide [*Hughes*, 1973*b*]. Ice domes along this ice divide are associated with the Edsel Ford, Flood, and Executive Committee ranges and the Crary, Whitmore, Thiel, and Horlick mountains. Flow lines diverging from these ice domes converge on ice streams A through F in Figure 1, which begin downstream from the six saddles separating the seven ice divide domes. Flow lines diverging from these six ice streams form the bulk of the West Antarctic portion of the Ross Ice Shelf.

The slip line field for advective flow in ice streams can be determined by applying plasticity theory to various types of plane strain deformation. Surface advective flow in plan view

is a combination of extrusion flow at the beginning of the ice stream, extending flow in the body of the ice stream, and indenting flow at the end of the ice stream. Plane strain slip line fields for extrusion, extending, and indenting flow are all calculated from plasticity theory and are given by *Hill* [1964]. These three solutions are shown in Figure 17 and are joined to give the ice stream solution. Flow lines in Figure 17 are vector sums of ice velocity vectors u_i entering the ice stream and principal strain rate vectors $\partial u_j/\partial x_j$ in the ice stream at 45° to slip lines. The curvature of slip lines in extrusion flow is controlled by the ratio of the piston diameter to the orifice diameter. In the ice stream application this curvature would be determined by the ratio of the ice stream width to the distance between ice streams. The curvature of slip lines in extending flow is determined by the ratio of the distance between parallel plates to their half-length. In the ice stream application this curvature would be determined by the ratio of ice stream width to ice stream length. The curvature of slip lines in indenting flow is determined by the shape of the die driven into the plastic plate. In the ice stream application the die shape is related to the ice stream surface velocity field when it penetrates the ice shelf. As is shown by Figure 2, this velocity field is equivalent to a flat die. For ice streams the rate of extrusion flow is determined by the dynamics of converging flow at the head of the ice stream, the rate of extending flow is determined by the dynamics of lateral flow from glaciated areas between ice streams, and the rate of indenting flow is determined by the dynamics of diverging flow when the ice stream merges with the ice shelf. These dynamics are controlled by ice stream geometry, which is determined primarily by basal conditions. Hence a direct study of surface dynamics is an indirect study of basal conditions.

Advective flow in longitudinal profile for an ice stream is akin to the plane strain problem of a long thin slab flowing down a gentle slope under its own weight. The plasticity solution for this problem has been given by *Nye* [1951]. Furthermore, viscoplastic solutions have been provided by *Nye* [1957] for ice frozen to the bed and by *Weertman* [1957] for ice floating above the bed. These two solutions are modificiations of solutions for a material compressed between rough and smooth rigid parallel plates, respectively, rough plates being coupled to the material and smooth plates being uncoupled from the material. They apply at the beginning and at the end of an ice stream, respectively, assuming that the ice stream forms by progressive uncoupling from the bed until it floats. These two solutions, therefore, help define the boundary conditions for an ice stream solution. Figure 18 illustrates the slip line field and laminar flow line field that such a solution is expected to predict. The segments of mutually orthogonal cycloids constitute the slip line field for the ice dome coupled to the bed at the head of the ice stream. In the ice stream this slip line field gradually is converted into an orthogonal slip line field consisting of concentric circles and radial lines converging at the ice stream–ice shelf junction. The slip line field then converts to a square grid intersecting the top and bottom surfaces at 45° angles when the ice stream becomes afloat and merges with the ice shelf.

c. *Surface Plastic Stress and Velocity Fields Across an Ice Stream*

Consider the surface of an ice stream midway between its head, where extrusion flow predominates, and its foot, where indenting flow predominates. The plane strain stress–velocity plasticity solution for this region is equivalent to that of a weightless plastic slab compressed between rigid parallel plates, as described by *Hill* [1964, pp. 226–236] and illustrated in Figure 19. Let x be the longitudinal flow direction along flow lines, y be the transverse direction normal to flow lines, and z be the vertical direction normal to the surface. Consider the central region of an ice stream having a constant width. Flow lines in this region will therefore be parallel, and the equations of surface stress on an ice stream whose length L greatly exceeds its half width Λ are

$$(\sigma_x/\tau_0) = \psi + k(x/\Lambda) \pm 2[1 - k^2(y/\Lambda)^2]^{1/2} \quad (82)$$

$$(\sigma_y/\tau_0) = \psi + k(x/\Lambda) \quad (83)$$

$$(\sigma_{xy}/\tau_0) = k(y/\Lambda) \quad (84)$$

where τ_0 is the lateral plastic yield stress in shear and $0 \leq k \leq 1$. The ice stream coupling factor k describes coupling across the side boundaries of the ice stream. Note that the stress components are independent of x and y when the ice stream is uncoupled across its side boundaries ($k = 0$). The constant ψ is determined by the value of k.

For the last term in (82) the positive sign applies for extending ice stream flow, and the negative sign applies for compressive ice stream flow. When an ice stream merges with a confined and pinned ice shelf, extending flow predominates upstream from the ice stream grounding line and is caused by lateral flow from the ice dome to the ice stream, and compressive flow predominates downstream from the ice stream grounding line and is caused by lateral flow from the ice stream to the ice shelf. This lateral flow is along flow lines which cross the stationary sides of the ice stream and is equivalent to deformation of a plastic slab when the rigid parallel plates are being either forced together (extending flow) or forced apart (compressive flow). Extending flow exists along the entire ice stream if its floating tongue is unconfined by an ice shelf.

When mass balance in the ice stream is neglected, the equations of surface velocity for the ice stream are

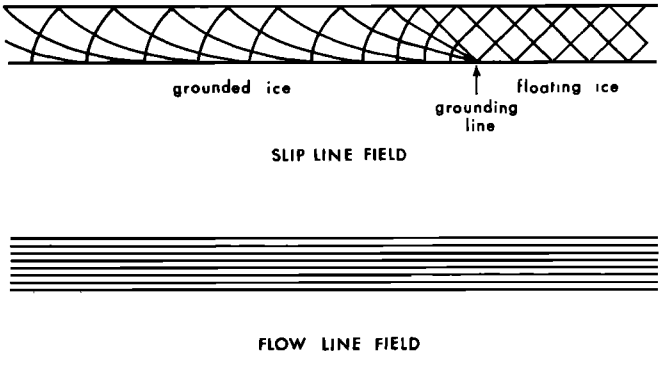

Fig. 18. A longitudinal profile of slip line and flow line fields in ice streams according to plasticity theory. The ice stream has a free top surface for both its grounded and its floating portion, so that lines of maximum shear stress must meet the surface at 45° angles everywhere. However, the ice stream base changes from a rigid boundary on the ice sheet side of its surface inflection line to a free boundary on the ice shelf side of its basal grounding line. Lines of maximum shear stress meet the rigid boundary at 0° or 90° angles and meet the free boundary at 45° angles. Hence the slip line field in the ice stream is a continuous change from orthogonal cycloids in the ice sheet to orthogonal straight lines in the ice shelf and reflects progressive ice-bed uncoupling. The flow line field in the ice stream consists of straight lines parallel to the ice stream surfaces, provided ice thickness is constant and no accumulation or ablation occurs at the surface and base of the ice stream.

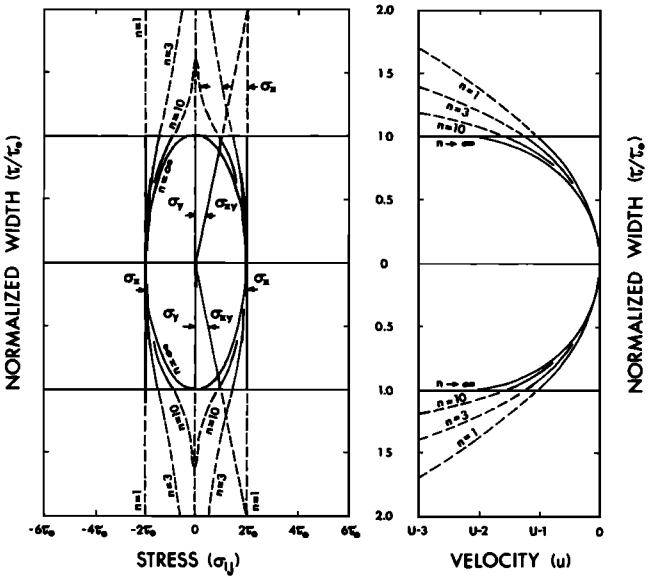

Fig. 19. The stress and velocity fields across the surface of an ice stream. The stress tensor σ_{ij} has longitudinal, transverse, and horizontal shear components σ_x, σ_y, and σ_{xy}. The effective stress τ reaches a maximum τ_0 at the sides of the ice stream. The longitudinal velocity u reaches a maximum U at the center line of the ice stream. Variations of σ_1 and σ_{11} are independent of the viscoplastic properties of ice, but variations of σ_1 and u are not. Hence σ_x and u variations are shown for several values of the viscoplastic parameter n in (98), ranging from perfectly viscous flow ($n = 1$) to perfectly plastic flow ($n = \infty$). Note that $\tau = \tau_0$ is the plastic yield stress, and this fixes the position of the ice stream sides for $n = \infty$. Extending and compressive flow exists for values of σ_1 to the right and left of the σ_y line, respectively. The surface stress and velocity fields extend to the base for the floating portion of an ice stream. The velocity profile is for homogeneous deformation. However, viscoplastic instability insures nonhomogeneous deformation which would sharpen the velocity profile toward the sides of the ice stream, as shown for Byrd Glacier in Figure 2.

$$u = U \pm V(x/\Lambda) + V(2/k)[1 - k^2(y/\Lambda)^2]^{1/2} \quad (85)$$

$$v = \mp V(y/\Lambda) \quad (86)$$

where u is velocity in the x direction, v is velocity in the y direction, U is the surface flow rate through a transverse cross section, and V is the surface flow rate through a longitudinal cross section along the side of the ice stream. Note that u is independent of y and becomes infinite when the ice stream is uncoupled across its side boundaries ($k = 0$).

The longitudinal velocity field across the ice stream surface is a half ellipse given by the equation

$$\left[\frac{k(Ut)\xi}{\Lambda^2 - (Ut)^2} + (1 - k^2)^{1/2}\right]^2 + \left(k\frac{y}{\Lambda}\right)^2 = 1 \quad (87)$$

This equation describes the forward bowing ξ during time t of a straight line initially of length Λ and parallel to y, where each ξ applies to a point on the line for which (y/Λ) remains constant, so that (Λ/k) and $[\Lambda^2 - (Ut)^2]/k(Ut)$ are the semimajor and semiminor axes of the half ellipse. Note that the velocity profile becomes less dependent on y as k decreases. Equation (87) is the ice stream equivalent of the deformation profile derived by *Hill* [1964, p. 234] for compression of a plastic slab between flat rigid parallel plates.

d. Center Line Plastic Stress and Velocity Fields Along an Ice Stream

Consider a vertical plane along the center line and midway between the beginning and end of an ice stream. The plane strain stress-velocity solution for this region is equivalent to the deformation under its own weight of a plastic slab lying on a flat rigid bed, as described by *Nye* [1951] and illustrated in Figure 20. For an ice stream the bed varies from perfectly rough at its head, where ice-bed coupling is strong, to perfectly smooth at its foot, where ice-bed coupling vanishes. The stress equations for an ice stream having constant thickness h and slope θ are

$$(\sigma_x/\tau_0) = -k(z/h)\cot\theta \pm 2[1 - k^2(z/h)^2]^{1/2} \quad (88)$$

$$(\sigma_z/\tau_0) = -k(z/h)\cot\theta \quad (89)$$

$$(\sigma_{xz}/\tau_0) = k(z/h) \quad (90)$$

where τ_0 is the basal plastic yield stress in shear and $0 \le k \le 1$. The ice stream coupling factor k describes coupling across the bottom boundary of the ice stream. Note that the stress components are independent of z when the ice stream is uncoupled across its bottom boundary ($k = 0$), since k is zero for ice floating above the bed and unity for ice frozen to the bed.

For the last term in (88) the positive sign applies to extending ice stream flow, and the negative sign applies to compressive ice stream flow. When an ice stream merges with a confined and pinned ice shelf, extending flow predominates upstream from the ice stream grounding line where $0 < k < 1$, and compressive flow predominates downstream from the grounding line where $k = 0$. However, if the floating portion of the ice stream does not merge with an ice shelf or if it punches through an ice shelf into open sea, $k = 0$, and extending flow characterizes both the grounded and the floating portion of the ice stream.

Including mass balance in the ice stream, the velocity equations are

$$u = U \pm W(x/h) + W(2/k)[1 - k^2(z/h)^2]^{1/2} \quad (91)$$

$$w = \mp W(z/h) \quad (92)$$

where w is the ice velocity parallel to z and W is the net ice accumulation rate on the ice stream surfaces. Note that u is independent of z and becomes infinite when the ice stream is uncoupled across its bottom boundary ($k = 0$). The surface velocity U includes any basal sliding.

The longitudinal velocity field through the ice stream is a quarter ellipse given by the equation

$$\left[\frac{k(Ut)\zeta}{h^2 - (Ut)^2} + (1 - k^2)^{1/2}\right]^2 + \left(k\frac{z}{h}\right)^2 = 1 \quad (93)$$

This equation describes the forward bowing ζ during time t of a straight line initially of length h and parallel to z, where ζ applies to a point on the line for which (z/h) remains constant. The velocity profile is therefore a quarter ellipse having a semimajor axis (h/k) and a semiminor axis $[h^2 - (Ut)^2]/k(Ut)$. Note that the velocity profile becomes independent of z as k decreases.

Plasticity theory is inadequate when $k = 0$ because the longitudinal velocity becomes infinite, and its lateral and vertical profiles become indeterminate. Viscoplastic theory based on the flow law of ice must therefore be applied.

e. The Ice Stream Coupling Factor and Viscoplastic Instability

Stress, velocity, and slip line fields presented thus far are based on the theory of plasticity, for which $n = \infty$ in (27). However, ice is a viscoplastic material best approximated by n

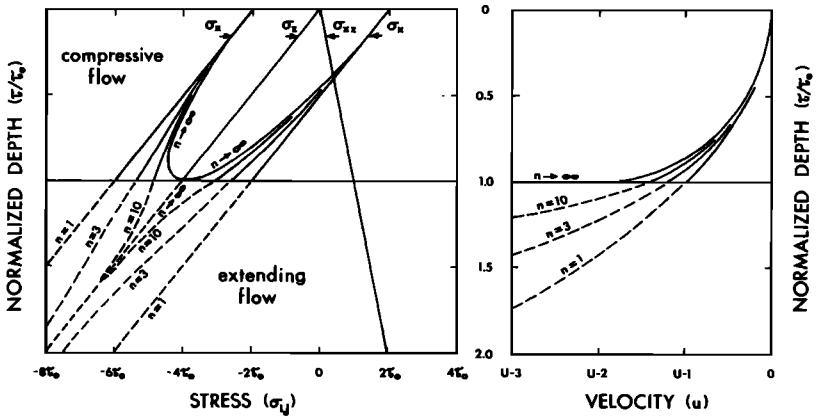

Fig. 20. The stress and velocity fields in a vertical cross section along the center line of an ice stream. The stress tensor σ_{ij} has longitudinal, vertical, and vertical shear components σ_x, σ_z, and σ_{xz}. The effective stress τ reaches a maximum τ_0 at the base of the ice stream. The longitudinal velocity u reaches a maximum U at the surface of the ice stream. Variations of σ_z and σ_{xz} are independent of the viscoplastic properties of ice, but variations of σ_x and u are not. Hence σ_x and u variations are shown for several values of the viscoplastic parameter n in (98), ranging from perfectly viscous flow ($n = 1$) to perfectly plastic flow ($n = \infty$). The value of U results from internal ice deformation and does not include the surface velocity resulting from basal sliding of the ice stream. Note that $\tau = \tau_0$ is the plastic yield stress, and this fixes the position of the ice stream bed for $n = \infty$. Extending and compressive flows exist for values of σ_x to the right and left of the σ_z line, respectively. The center line stress and velocity fields apply only to the grounded portion of an ice stream, and the velocity profile is for homogeneous deformation [*Nye*, 1957]. However, viscoplastic instability insures nonhomogeneous deformation which would sharpen the velocity gradient toward the bed.

= 3. The similarities and differences between plastic and viscoplastic flow are emphasized by normalizing lateral and vertical stress profiles with respect to the maximum surface shear stress at the sides of the ice stream $(\tau_0)_s$, the maximum center line shear stress at the base of the ice stream $(\tau_0)_c$, and the maximum center line hydrostatic pressure at the base of the ice stream $(P_0)_c$, where the x axis is the center line surface flow line:

$$(\tau_0)_s = \rho g \Lambda \sin\theta \tag{94}$$

$$(\tau_0)_c = \rho g h \sin\theta \tag{95}$$

$$(P_0)_c = \rho g h \cos\theta \tag{96}$$

For an ice stream of half width Λ, thickness h, and slope θ, based on (94)–(96), the surface plane strain stresses are given by the following equations:

Plastic

$$(\sigma_x/\tau_0)_s = \psi + k(x/\Lambda) \pm 2[1 - k^2(y/\Lambda)^2]^{1/2}$$

Viscoplastic

$$(\sigma_x/\tau_0)_s = \psi + k(x/\Lambda) \pm 2[(\tau/\tau_0)_s^2 - k^2(y/\Lambda)^2]^{1/2}$$

Plastic

$$(\sigma_y/\tau_0)_s = \psi + k(x/\Lambda)$$

Viscoplastic

$$(\sigma_y/\tau_0)_s = \psi + k(x/\Lambda)$$

Plastic

$$(\sigma_{xy}/\tau_0)_s = k(y/\Lambda)$$

Viscoplastic

$$(\sigma_{xy}/\tau_0)_s = k(y/\Lambda)$$

and the center line plane strain stresses are given by the following equations:

Plastic

$$(\sigma_x/\tau_0)_c = -(P_0/\tau_0)_c(z/h) \pm 2[1 - k^2(z/h)^2]^{1/2}$$

Viscoplastic

$$(\sigma_x/\tau_0)_c = -(P_0/\tau_0)_c(z/h) \pm 2[(\tau/\tau_0)_c^2 - k^2(z/h)^2]^{1/2}$$

Plastic

$$(\sigma_y/\tau_0)_c = -(P_0/\tau_0)_c(z/h)$$

Viscoplastic

$$(\sigma_y/\tau_0)_c = -(P_0/\tau_0)_c(z/h)$$

Plastic

$$(\sigma_{xy}/\tau_0)_c = k(z/h)$$

Viscoplastic

$$(\sigma_{xy}/\tau_0)_c = k(z/h)$$

There is no difference between plastic and viscoplastic flow in the σ_y and σ_{xy} expressions, and the only difference in the σ_x expressions is the ratio (τ/τ_0) in their final term, where τ is the effective shear stress.

In view of the strong similarities between plastic and viscoplastic flow emphasized by these equations the ice stream coupling factor k developed from plasticity theory must also be fundamental to viscoplastic flow. It should be related to viscoplastic instability across shear zone boundaries that are lubricated by a strain-softened ice layer and to glacial sliding across ice-rock boundaries that are lubricated by a meltwater layer. The slip velocity u_s across these ice stream boundaries is [*Weertman*, 1964*b*]

$$u_s = (\tau_0/B)^\omega \tag{97}$$

where τ_0 is the shear stress in ice at the boundary, B is a boundary friction parameter, and ω is a viscoplastic parameter. Note the similarity with the flow law for ice [*Nye*, 1957],

$$\dot{\epsilon} = (\tau/A)^n \tag{98}$$

where $\dot{\epsilon}$ is the effective strain rate, τ is the effective shear stress,

A is a rigidity parameter, and n is a viscoplastic parameter. Simple shear exists in a lateral shear zone of width W alongside an ice stream. Viscoplastic instability in the shear zone reduces W and reduces A in the shear zone. Hence if u_s is the mean slip velocity across W, (97) and (98) can be combined to give

$$u_s = (\tau_0/B)^\omega \simeq W(\tau/A)^n \tag{99}$$

This suggests the following formulation for the ice stream coupling factor:

$$k = W/\Lambda \simeq A^n\tau_0^\omega/\Lambda B^\omega\tau^n \tag{100}$$

For complete coupling, $k = 1$ and $W = \Lambda$. Viscoplastic instability has not occurred, so there is no strain-softened ice, and homogeneous deformation allows simple shear to extend from the sides to the center line of the ice stream. For partial coupling, $0 < k < 1$ and $0 < W < \Lambda$. Viscoplastic instability has created strain-softened ice zones of width W alongside the ice stream, and nonhomogeneous deformation confines most of the simple shear to these zones. For no coupling, $k = 0$ and $W = 0$. Flotation uncouples the basal boundary from bedrock, and fracture uncouples the side boundaries from slow-moving ice or rock walls, so the ice stream has free surfaces at its base and sides when $k = 0$. Hence $W = 0$ because simple shear vanishes.

The slip velocity u_s can have a component due to shear within W and sliding across W when $0 < k < 1$. In the *Weertman* [1964*b*, 1969] theory of glacial sliding, $B \propto A$ and $\omega = n$ for a frozen ice-rock boundary, and $B \propto AR^2$ and $\omega = \frac{1}{2}(n + 1)$ for a thawed ice-rock boundary, where the bed roughness factor R is the ratio of the average dimension of bedrock projections of a given size divided by the average separation of these projections and is assumed to be constant for all sizes of projections. Sliding across ice stream boundaries is increased by reducing A and R, which decrease B in (99). Viscoplastic instability reduces A by strain softening. Frictional heat reduces A by raising temperature below the pressure melting point and reduces R by increasing melting at the pressure melting point. Increased melting thickens the basal water layer, which lowers R by drowning the smaller bedrock projections and leads to ice-bed uncoupling sufficient to cause a glacial surge [*Weertman*, 1969]. Complete basal uncoupling, of course, requires that $R = 0$ and that the ice be floating on the basal water layer. Hence an ice stream must be afloat when $k = 0$ at its bottom boundary. Equation (97) is invalid when an ice stream becomes afloat, because $\tau_0 = 0$ when $R = 0$ and new boundary conditions apply.

f. The Ice Stream Coupling Factor and Surging Ice Streams

Complete lateral uncoupling also requires that the ice stream become afloat, because fracture cracks in the lateral shear zones alongside the ice stream can then fill with water for all depths below sea level. This water exerts a positive hydrostatic pressure at the crack tip (water being more dense than ice), so that the tips can migrate toward each other from the top and bottom ice stream surfaces [*Weertman*, 1973]. Tidal flexure of the floating ice stream may be responsible for fracture along the lateral shear zones as $W \to 0$ if the ice stream sides remain grounded either on bedrock or against fjord walls. Lateral tensile stresses σ_y caused by tidal flexure are normal to lateral shear stresses σ_{xy} which created the easy glide ice fabric in the lateral shear zones. Hence σ_y results in hard glide, which terminates in brittle fracture more quickly than ductile easy glide does [*Higashi*, 1969]. The lateral rift zones extending beyond Byrd Glacier fjord in Figure 2 may have been initiated by tidal flexure of the portion of Byrd Glacier afloat in the fjord. Once formed, the rifts could be maintained by the differential velocity between the Byrd Glacier floating ice tongue and the Ross Ice Shelf. This ice tongue remains substantially uncoupled from the ice shelf for up to 45 km beyond Byrd Glacier fjord. Presumably, rift length increases as the ice stream velocity increases, so that a surging ice stream could punch through a sufficiently narrow ice shelf.

Viscoplastic instability changes the field of maximum surface shear stress from the one shown in Figure 17 to the one shown in Figure 21. In plasticity theory, Figure 21 shows the slip line field for plastic slabs compressed between rigid parallel plates, one plate being perfectly rough ($k = 1$) and the other plate perfectly smooth ($k = 0$). The plastic slabs are the lateral shear zones of width W alongside an ice stream where viscoplastic instability has created strain-softened ice. The central zone of the ice stream moves as a rigid slab between these shear zones if laminar flow predominates. However, if either extending or compressive flow exists in the central zone, it will deform like a plastic slab compressed between frictionless plates. These plates would be the lateral shear zones. Comparing velocity profiles across Antarctic and Greenland ice streams [*Swithinbank*, 1963; *Carbonnell and Bauer*, 1968] shows that the width of the lateral shear zones decreases as ice velocity and ice temperature increase. This is possible only if these increases resulted from viscoplastic instability which created an easy glide ice fabric in the shear zones. The distribution of maximum surface shear stresses shown in Figure 21 is the result and can therefore be expected during an ice stream surge. *Weertman* [1969] believes that these fast-moving ice streams are indeed surging.

g. Convection Flow in Ice Streams

Convection flow in an ice sheet may arise from vertical density inversions caused by the increase in ice temperature toward the bed [*Hughes*, 1976]. The ice stream modification of ice sheet convection would arise from horizontal density gradients caused by an increase in ice temperatures toward ice streams. In both cases the increase in temperature is due to an increase in frictional heat generated by shear deformation. If frictional heating at the base and along the sides of an ice stream does indeed make the ice stream significantly hotter than adjacent ice, the ice stream may rise en masse as a rigid slab, owing to buoyancy effects. *Orowan* [1965] has analyzed the similar problem of a hot slab rising in the earth's mantle, and his analysis is easily modified for ice streams, as is shown in Figure 21. Consider an ice stream in a shallow subglacial bedrock trench ending at the continental shelf margin, as is the case for the major ice streams in West Antarctica. As the ice stream flows toward the ice sheet margin, frictional heat expands ice in the vertical shear zones alongside the ice stream. Buoyancy then moves this hot ice upward, to be replaced by colder ice moving in from the sides by normal advective flow. To apply Orowan's analysis, if d is the thickness of hot ice in the shear zone and h is the thickness of the ice sheet, the temperature difference δT between the shear zone and adjacent ice needed to cause ice stream convection is

$$\delta T = [(1 + \pi/2)W + 3d]\sigma_0/\rho g d W \alpha_V \tag{101}$$

where $d < h$, W is the width of the shear zone, ρ is mean ice density, g is gravity acceleration, σ_0 is the yield stress of ice in

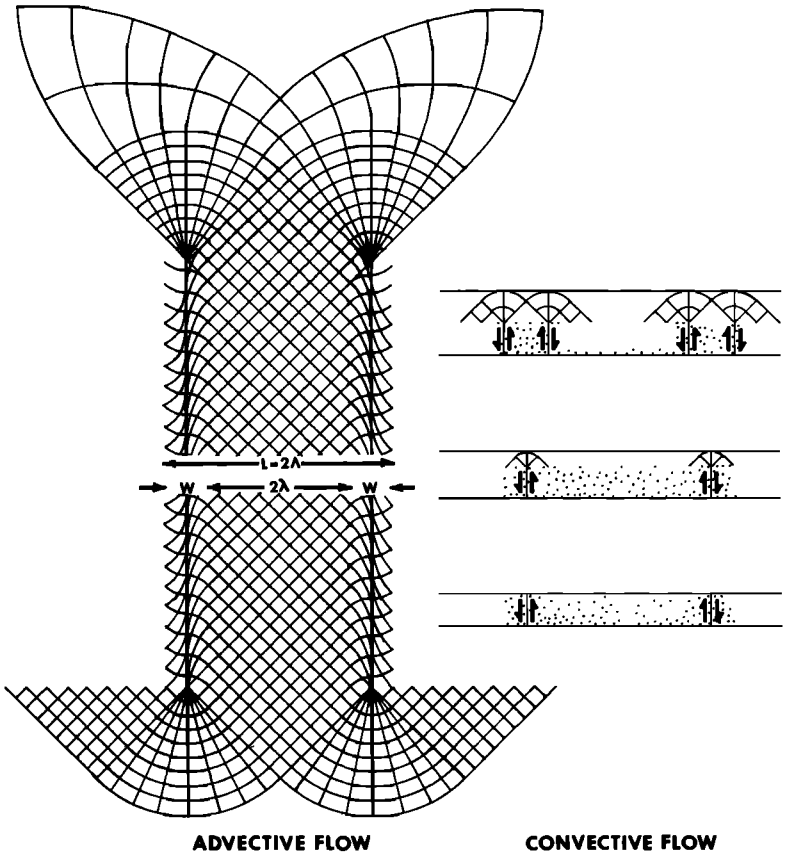

Fig. 21. The field of maximum shear stress in an ice stream when advective horizontal flow in the surface plan view and convective vertical flow in the transverse profile views are influenced by viscoplastic instability. In advective flow, longitudinal strain rates predominate toward the center, where the shear stress trajectories are orthogonal straight lines, and shear strain rates predominate toward the sides, where the shear stress trajectories are orthogonal cycloids, creating four-pole and single-pole ice fabrics in widths 2λ and W, respectively, separated by transitional ice fabrics in widths $\Lambda - \lambda - W$. For an outlet glacier, 2Λ is the fjord width, and the maximum shear strain rate may occur along the fjord walls, so that W is half the width shown here. In convective flow, vertical shear buoys only the lateral shear zones if widths W are much hotter than flanking ice and buoys the entire ice stream if width 2Λ is much hotter than flanking ice. If the thickness of cold surface ice is comparable to the thickness of hot basal ice, then convection flow must also deform the cold ice overlying the lateral shear zones. Hot ice is dotted.

uniaxial compression, and α_V is the volume thermal expansion coefficient of ice. As the ice stream accelerates with increased convergent flow and basal sliding toward the ice sheet margin, frictional heat from longitudinal strain rates may make the entire ice stream sufficiently warmer than adjacent ice to be buoyed upward en masse. In this case, (101) reduces to

$$\delta T = \sigma_0/\rho g L \alpha_V \tag{102}$$

where $d = h$ and L is the width of the ice stream. This is the interesting case. Since an ice stream is grounded below sea level and becomes afloat when it reaches the sea, en masse uplift from convection will cause sea water to rush in under the ice stream and uncouple it from its bed. An ice stream surge should result [*Hughes*, 1976].

For axes x horizontal along the ice stream, y horizontal across the ice stream, and z vertical, viscoplastic instability and the advective shear stress σ_{xy} create a single-maximum ice fabric in the shear zones alongside the ice stream, the optic axes of ice crystals being closely parallel to the y axis. This is also an easy glide ice fabric for the convective shear stress σ_{zy}, so the yield stress will be much less than for randomly oriented ice crystals in which both easy glide and hard glide occur. The yield stress usually assigned to ice when it is treated as a perfectly plastic material is $\sigma_0 \simeq 1.0$ bar. However, $\sigma_0 \simeq 10$ bars for a hard glide fabric, and $\sigma_0 \simeq 0.1$ bar for an easy glide fabric. Equations (101) and (102) are plotted in Figure 22 as $\delta T/\sigma_0$ versus W or L for $d = 1$ km, which is the approximate ice thickness when ice streams first become visible on the surface. Typical widths of major West Antarctic ice streams are in the range 25 km $< L <$ 50 km, for which $0.3° < \delta T < 0.1°$ when $d = h$ and $\sigma_0 = 0.1$ bar. The ice stream should rise en masse under these conditions, because $\delta T/\sigma_0$ is lowest when the width of the hot ice slab is greatest. Hence an ice stream of width $L >> W$ is more easily buoyed upward than ice in its lateral shear zones of width W, unless shear zone ice is substantially hotter than ice in the ice stream as a whole.

Of course, the surface temperature of an ice stream in a layer of depth $(h - d)$ is comparable with the general surface temperature, which is substantially lower than temperatures deeper in the ice stream. Therefore (101) must be used if $(h - d) \simeq d$, and values of $\delta T/\sigma_0$ in Figure 22 are too large for ice stream convection because the buoyancy stress must overcome not only the low-yield stress in hot flanking ice favorably oriented for vertical shear, but also the high-yield stress in cold overlying ice not favorably oriented for indenting flow. Ice stream convection is possible only if $(h - d) \ll d$, so that (102) applies.

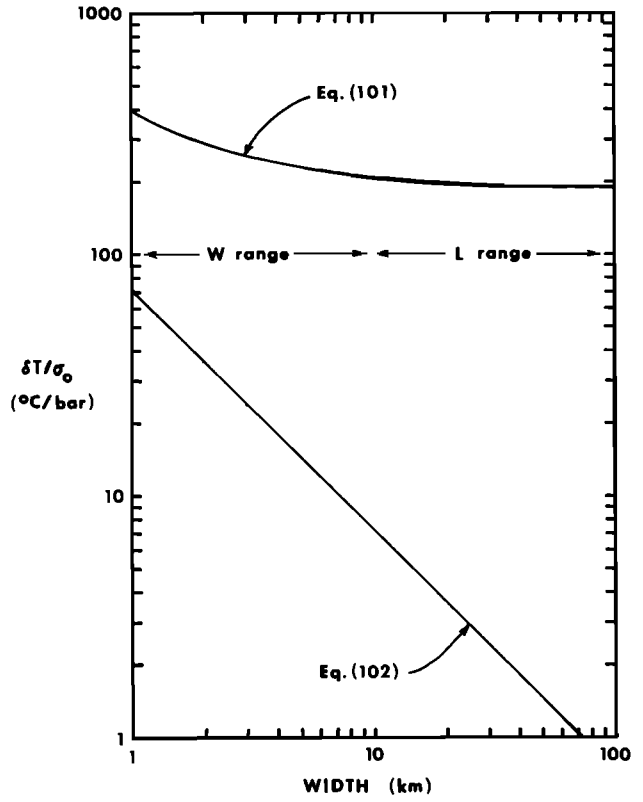

Fig. 22. Thermal conditions for ice stream convection according to plasticity theory. The temperature difference δT needed to buoy a slab of hot ice having a yield stress σ_0 varies according to the value of σ_0, the width of the hot slab, and the thickness of cold ice above the slab. Values of $\delta T/\sigma_0$ are given by (101) if the cold ice layer is thick and by (102) if the cold ice layer is thin. If the hot slab is confined to the lateral shear zones alongside an ice stream, it has widths in the *W* range, but if the hot slab is the entire ice stream, it has widths in the *L* range.

6. The Boundaries of Ice Streams

a. Viscoplastic Instability and the Side Ice Stream Boundaries

A comparison of the surface velocity profile across several East Antarctic outlet glaciers [*Swithinbank*, 1963] with the surface velocity profile predicted for homogeneous flow in Figure 19 shows progressively poorer agreement as outlet glacier velocity increases, shear deformation being increasingly confined in increasingly narrow zones alongside the outlet glacier. Nonhomogeneous flow results if viscoplastic instability has restricted most of the surface velocity gradient to relatively narrow shear zones alongside ice streams. Byrd Glacier has the fastest velocity and, as shown in Figure 2, a velocity profile least like that predicted by Figure 19.

Viscoplastic instability also generates frictional heat where sharp strain gradients exist because ice deformation is intense. Ice temperature rises in such regions, provided the ice is below its pressure melting point. As is shown by Figure 15, the strain rate of ice in a given stress regime is increased when its temperature increases. Hence viscoplastic instability concentrates the velocity gradient at the sides of an ice stream by creating an easy glide ice fabric at an elevated temperature near these boundaries.

The shape of the Byrd Glacier velocity profile in Figure 2, fundamentally different from ice stream velocity profiles predicted by (85) and shown in Figure 19, will now be analyzed in terms of viscoplastic instability. As with other problems in glaciology, viscoplastic instability can be analyzed by using the tensor forms of the equilibrium equations

$$\partial\sigma_{ij}/\partial j + \rho g_i = 0 \tag{103}$$

the compatibility equations

$$\dot{\epsilon}_{ij} = \tfrac{1}{2}(\partial u_i/\partial j + \partial u_j/\partial i) \tag{104}$$

the constitutive equations

$$\dot{\epsilon}_{ij} = (\tau^{n-1}/A^n)\sigma_{ij}' \tag{105}$$

and the boundary conditions, where

$$\sigma_{ij}' = \sigma_{ij} - \tfrac{1}{3}\delta_{ij}\sigma_{kk} = \sigma_{ij} - \delta_{ij}P \tag{106}$$

and

$$\tau = (\tfrac{1}{2}\sigma_{ij}'\sigma_{ij}')^{1/2} \tag{107}$$

where $i, j, k = x, y, z$ in succession and represent mutually orthogonal coordinates, σ_{ij} are components of the stress tensor, σ_{ij}' are deviator stress components, σ_{kk} are normal stress components, τ is the effective stress, P is the hydrostatic pressure, $\dot{\epsilon}_{ij}$ are components of the strain rate tensor, g_i are components of the gravity acceleration vector, u_i and u_j are components of the velocity vector, ρ is density, n is a viscoplastic parameter, A is a rigidity parameter, and δ_{ij} is the Kronecker delta ($\delta_{ij} = 1$ when $i = j$ and $\delta_{ij} = 0$ when $i \neq j$). See the book by *Nye* [1960*b*] for a comprehensive introduction to tensor theory and the book by *Paterson* [1969] for application to glaciological problems.

Viscoplastic instability in Byrd Glacier can be studied by applying (103)–(107) and the procedures developed by *Thomas* [1973*a*, *b*] to the data in Table 1. Take the origin of coordinates x, y, z at sea level halfway across the velocity profile in Figure 2, with x horizontal along the fjord, y horizontal across the fjord, and z vertical above the fjord. From (103), assuming $\sigma_{xz} \simeq \sigma_{yz} \simeq 0$,

$$\partial\sigma_x/\partial x \simeq -(\partial\sigma_{xy}/\partial y) \tag{108}$$

$$\partial\sigma_y/\partial y \simeq -(\partial\sigma_{xy}/\partial x) \tag{109}$$

$$\partial\sigma_z/\partial z \simeq \rho g \tag{110}$$

These assumptions are based on the observation [*Giovinetto et al.*, 1966] that the velocity profile in Figure 2 was measured across the floating portion of Byrd Glacier. Hence free surface boundary conditions prevail at $z = h$ and $z = H$, where h and H are the ice thicknesses above and below sea level. Assuming that ice is incompressible,

$$\dot{\epsilon}_x + \dot{\epsilon}_y + \dot{\epsilon}_z = 0 \tag{111}$$

From (105), (106), (107), and (111),

$$\begin{aligned} 2\tau^2 &= \sigma_x'^2 + \sigma_y'^2 + \sigma_z'^2 + 2(\sigma_{xy}^2 + \sigma_{yz}^2 + \sigma_{zx}^2) \\ &= \sigma_x'^2 + [(\dot{\epsilon}_y/\dot{\epsilon}_x)\sigma_x']^2 + [(\dot{\epsilon}_z/\dot{\epsilon}_x)\sigma_x']^2 \\ &\quad + [(\dot{\epsilon}_{xy}/\dot{\epsilon}_x)\sigma_x']^2 + [(\dot{\epsilon}_{yz}/\dot{\epsilon}_x)\sigma_x']^2 + [(\dot{\epsilon}_{zx}/\dot{\epsilon}_x)\sigma_x']^2 \\ &= 2(1 + \alpha + \alpha^2 + \beta^2)\sigma_x' \end{aligned} \tag{112}$$

where $(\dot{\epsilon}_y/\dot{\epsilon}_x) = \alpha$, $(\dot{\epsilon}_z/\dot{\epsilon}_x) = -(1 + \alpha)$, $(\dot{\epsilon}_{xy}/\dot{\epsilon}_x) = \beta$, and $(\dot{\epsilon}_{yz}/\dot{\epsilon}_x) \simeq (\dot{\epsilon}_{zx}/\dot{\epsilon}_x) \simeq 0$. From (105) and (112),

$$\begin{aligned} \dot{\epsilon}_{xy} &= (\tau^{n-1}/A^n)\sigma_{xy}' \\ &= [(1 + \alpha + \alpha^2 + \beta^2)^{1/2}(\sigma_{xy}'/\beta)]^{n-1}\sigma_{xy}'/A^n \\ &= [(1 + \alpha + \alpha^2 + \beta^2)/\beta^2]^{(n-1)/2}(\sigma_{xy}'/A)^n \end{aligned} \tag{113}$$

From (104), $\partial u_x/\partial y = \dot{\gamma}_{xy} = 2\dot{\epsilon}_{xy}$ for simple shear. Assume $\sigma_{xy}' = (y/\Lambda)\tau_0$, where τ_0 is the yield shear stress along the fjord walls and Λ is the half width of the glacier. For simple shear along the fjord walls,

$$u_x = \int 2\dot{\epsilon}_{xy}\,dy = 2\int_y^{\Lambda}\left(\frac{1+\alpha+\alpha^2+\beta^2}{\beta^2}\right)^{(n-1)/2}(\tau_0/\Lambda A)^n y^n\,dy$$

$$= \left[\frac{2(1+\alpha+\alpha^2+\beta^2)^{(n-1)/2}\tau_0{}^n}{(n+1)\beta^{n-1}\Lambda^n A^n}\right](\Lambda^{n+1}-y^{n+1})$$

$$= \left[\frac{2(1+\alpha+\alpha^2+\beta^2)^{(n-1)/2}\Lambda\tau_0}{(n+1)\beta^{n-1}A^n}\right]\left[1-\left(\frac{y}{\Lambda}\right)^{n+1}\right]$$

$$= u_0\left[1-\left(\frac{y}{\Lambda}\right)^{n+1}\right] \qquad (114)$$

where u_0 is the velocity along the ice stream center line. This solution assumes that A, n, and $(1+\alpha+\alpha^2+\beta^2)/\beta^2$ are independent of y.

Strictly speaking, (114) applies only when the glacier behaves isotropically and deforms homogeneously. This means that A and n are constant in (114). In fact, ice is highly anisotropic, and nonhomogeneous deformation resulting from viscoplastic instability should cause A to decrease rapidly as the four-pole ice fabric developed by the predominance of σ_x toward the center of Byrd Glacier is transformed to the single-pole ice fabric developed by the predominance of σ_{xy} toward the glacier sides (see Figure 4).

To illustrate the consequences if strain softening due to viscoplastic instability is ignored, take $\Lambda = 12.8$ km and $u_0 = 2.25$ m/d as the half width and maximum velocity of Byrd Glacier at section $Y - Y'$ in Figure 2. When (114) is solved by using these values and the results are compared with the observed velocity profile, Figure 23 shows poor agreement for $n = 3$ but fair agreement for $n = 9$. One might therefore conclude that ice is much further to the plastic end of the viscoplastic spectrum than it actually is.

When strain softening due to viscoplastic instability is considered, then (114) must be modified. Take λ as the half width of the central region in which a four-pole ice fabric approximates isotropic conditions that allow homogeneous deformation for σ_x and $u_0 - u_\lambda$ as the maximum velocity change across this region. Setting $A = A_\lambda$ for $0 < y < \lambda$ gives

$$u_x - u_\lambda = \left[\frac{2(1+\alpha+\alpha^2+\beta^2)^{(n-1)/2}\lambda\tau_0{}^n}{(n+1)\beta^{n-1}A_\lambda{}^n}\right]\left[1-\left(\frac{y}{\lambda}\right)^{n+1}\right]$$

$$= (u_0-u_\lambda)\left[1-\left(\frac{y}{\lambda}\right)^{n+1}\right] \qquad (115)$$

where n, A_λ, and $(1+\alpha+\alpha^2+\beta^2)/\beta^2$ are independent of y. Take W as the width of the lateral shear zones, where the highly anisotropic single-pole ice fabric results in homogeneous deformation for σ_{xy}, and u_λ as the maximum velocity in this region. Furthermore, the velocity data near the fjord walls in Figure 23 suggest that $\sigma_{xy}' = \tau_0$ is a constant yield stress across W. Setting $A = A_W$ for $\lambda < y < \Lambda$ gives

$$u_x = \int 2\dot{\epsilon}_{xy}\,dy = 2\int_y^{\Lambda}\left(\frac{1+\alpha+\alpha^2+\beta^2}{\beta^2}\right)^{(n-1)/2}(\tau_0/A_W)^n\,dy$$

$$= \left[\frac{2(1+\alpha+\alpha^2+\beta^2)^{(n-1)/2}\tau_0{}^n}{\beta^{n-1}A_W{}^n}\right](\Lambda-y)$$

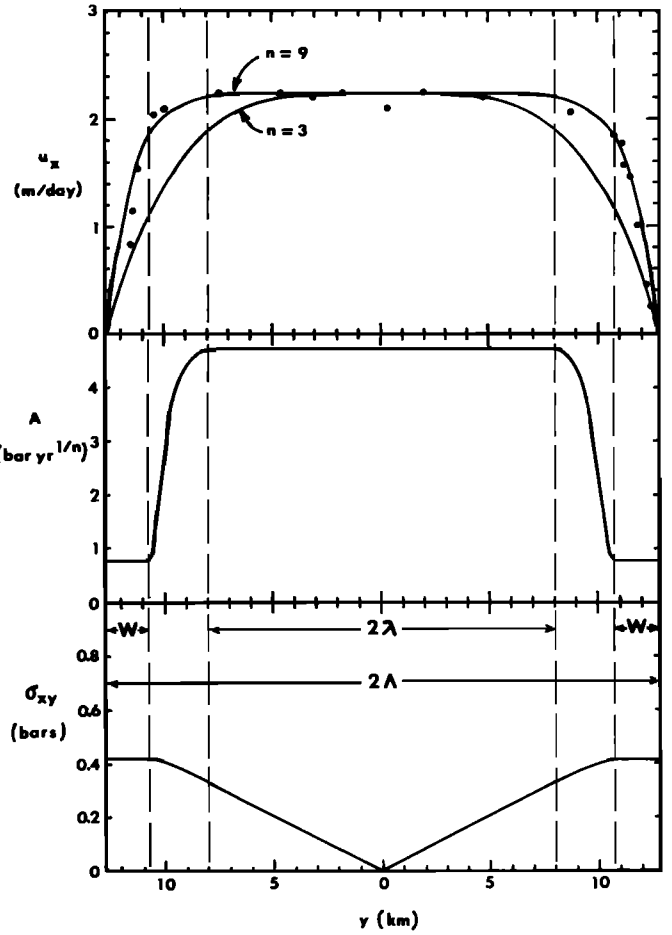

Fig. 23. The Byrd Glacier velocity data related to viscoplastic instability and strain softening alongside an ice stream. Longitudinal surface velocities u_x across section Y-Y' in Figure 2, reported by *Swithinbank* [1963] and shown as solid circles, are compared with theoretical curves for homogeneous flow, in which the rigidity parameter A is constant and the shear stress σ_{xy} varies linearly across the ice stream. Agreement is poor for $n = 3$, the measured viscoplastic parameter of ice, and fair for $n = 9$, a nearly plastic viscoplastic parameter. Agreement is best for $n = 3$ if A and σ_{xy} vary as shown, which is expected if viscoplastic instability creates a four-pole ice fabric in zone 2λ, a single-pole ice fabric in zones W, and transitional ice fabrics in zones $\Lambda - \lambda - W$. As is shown in Figure 4, strain softening is much more pronounced in a single-pole fabric than in a four-pole fabric.

$$= \left[\frac{2(1+\alpha+\alpha^2+\beta^2)^{(n-1)/2}\Lambda\tau_0{}^n}{\beta^{n-1}A_W{}^n}\right]\left[1-\left(\frac{y}{\Lambda}\right)\right]$$

$$= u_\lambda\frac{\Lambda}{W}\left(1-\frac{y}{\Lambda}\right) \qquad (116)$$

where n, A_W, and $(1+\alpha+\alpha^2+\beta^2)/\beta^2$ are independent of y.

From Figure 23, take $\Lambda = 12.8$ km as the total half width, $W = 2.0$ km and $u_\lambda = 1.90$ m/d as the width and maximum velocity for anisotropic zones alongside Byrd Glacier in (116), and $\lambda = 8.0$ km and $u_0 - u_\lambda = 0.01$ m/d as the half width and maximum velocity change for the isotropic central zone of Byrd Glacier in (115). These equations then give the best fit with the observed velocity profile at section Y-Y' of Byrd Glacier if $A_\lambda \to A_W$ across a transition zone of width $\Lambda - (\lambda + W) = 2.8$ km. Note that (114) for $n = 9$ fits the observed velocity profile almost as well as (115) and (116) with $n = 3$. This suggests that homogeneous plastic flow closely approximates nonhomogeneous viscoplastic flow. Hence the fact that many glaciological problems can be solved to a good approxi-

mation by assuming that ice is a perfectly plastic isotropic material is a direct result of viscoplastic instability in polycrystalline ice.

Velocities predicted by (115) and (116) are identical if $y = \lambda$ is placed in the transition zone at the point where $A_\lambda = A_W$. Outside this zone, from (113) and (114),

$$A_W \simeq \left[\frac{(n+1)W(u_0 - u_\lambda)}{\lambda u_\lambda}\right]^{1/n} A_\lambda \tag{117}$$

Substituting (117) into (116) and solving for τ_0 give

$$\tau_0 \simeq \left[\frac{(n+1)\beta^{n-1}A^n(u_0 - u_\lambda)}{2(1+\alpha+\alpha^2+\beta^2)^{(n-1)/2}\lambda}\right]^{1/n} \tag{118}$$

Assume that $\dot{\epsilon}_x$ and $\dot{\epsilon}_y$ are constant across section Y-Y' and are the values averaged between the grounding line and the fjord mouth in Table 1. Obtain the variation of $\dot{\epsilon}_{xy}$ across section Y-Y' from (104) and the velocity profile in Figure 23. These strain rates give $\alpha = 0.61$ and $\beta = 31$ for $y > \lambda$. Take $\Lambda = 12.8$ km, $\lambda = 10.0$ km, $u_0 = 2.25$ m/d, $u_\lambda = 2.24$ m/d, $n = 3$, and $A_\lambda = 4.75$ bars yr$^{1/3}$ for $y < \lambda$, assuming that this part of Byrd Glacier has ice fabrics and temperatures similar to the Ross Ice Shelf [*Thomas*, 1971]. Then (117) gives $A_W = 0.16$ and $A_\lambda = 0.78$ bar yr$^{1/3}$, and (118) gives $\tau_0 = 0.42$ bar. The variations of A and σ_{xy} for this analysis are plotted in Figure 23, where a transition from A_λ to A_W in the vicinity of $y = \lambda$ gives the u_x variation needed to match the observed velocity profile.

Setting $W = \Lambda - \lambda = 2.8$ km in (100) gives $k = 0.22$ as the viscoplastic coupling factor. Hence the effect of viscoplastic instability is to substantially uncouple Byrd Glacier from the fjord walls, so that the glacier behaves as though it were an ice stream of infinite width. The instability theory developed by *Weertman* [1974] for the ice shelf grounding line of a two-dimensional ice sheet will therefore apply to any fast-moving ice stream draining a marine ice sheet. In this theory, once the instability criterion is met, only boundary constraints in the ice shelf itself can prevent catastrophic collapse of the marine ice sheet.

b. *Ice Shelves and the Front Ice Stream Boundary*

In his two landmark papers, *Thomas* [1973*a*, *b*] developed the framework for treating all problems in ice shelf dynamics, including their interaction with ice streams. An ice shelf confined in an embayment and pinned at ice rises offers considerable resistance to the ice stream when it becomes afloat, so $\dot{\epsilon}_x$ will be lower than it would be for a freely floating ice tongue. In calculating $\dot{\epsilon}_x$, *Thomas* [1973*a*] notes that $\sigma_z' = (\dot{\epsilon}_z/\dot{\epsilon}_x)\sigma_x'$ from (105), $\sigma_x' + \sigma_z' = (\sigma_x - P) + (\sigma_z - P)$ from (106), and $\dot{\epsilon}_z = -(\dot{\epsilon}_x + \dot{\epsilon}_y)$ from (111) to obtain

$$\sigma_x' = \frac{\sigma_x - \sigma_z}{2 + (\dot{\epsilon}_y/\dot{\epsilon}_x)} = \frac{\sigma_x - \sigma_z}{2 + \alpha} \tag{119}$$

From (105), (112), and (119),

$$\begin{aligned}\dot{\epsilon}_x &= (\tau^{n-1}/A^n)\sigma_x' \\ &= [(1+\alpha+\alpha^2+\beta^2)^{(n-1)/2}/A^n]\sigma_x'^n \\ &= [(1+\alpha+\alpha^2+\beta^2)^{(n-1)/2}/(2+\alpha)^n A^n](\sigma_x - \sigma_z)^n\end{aligned} \tag{120}$$

A freely floating ice tongue spreads as a result of σ_z, which is the difference between the hydrostatic pressure in the ice and the hydrostatic pressure in the water. Spreading is retarded by σ_x when the floating ice tongue is imbedded in a confined and pinned ice shelf.

From (108), letting $L_z = H + h$ be the ice tongue thickness, ρ be mean ice density, and ρ_w be mean water density gives

$$\begin{aligned}\sigma_z &= -\frac{1}{L_z}\left[\int_{-H}^{h}\int_{z}^{h}\rho g\,dz\,dz - \int_{-H}^{0}\int_{z}^{0}\rho_w g\,dz\,dz\right] \\ &= -\frac{1}{2}\rho g L_z\left(1 - \frac{\rho}{\rho_w}\right) = -\frac{1}{2}\rho g h\end{aligned} \tag{121}$$

The force opposing spreading along x is F_x. Letting $L_y = 2\Lambda$ gives a relationship between σ_x and F_x of

$$\begin{aligned}\sigma_x &= -\frac{1}{L_y}\int_{-\Lambda}^{\Lambda}\left[\frac{1}{L_z}\int_{-H}^{h}\sigma_x\,dz\right]dy \\ &= -\frac{1}{L_y L_z}\int_{-\Lambda}^{\Lambda}\int_{-H}^{h}\sigma_x\,dz\,dy = -\frac{F_x}{L_y L_z}\end{aligned} \tag{122}$$

Substituting (121) and (122) into (120) gives

$$\dot{\epsilon}_x = \frac{(1+\alpha+\alpha^2+\beta^2)}{(2+\alpha)^n A^n}\left[\frac{\rho g h}{2} - \frac{F_x}{L_y L_z}\right]^n \tag{123}$$

where $L_y L_z$ is the cross-sectional area of the ice stream at the ice shelf grounding line.

The two major restraints exerted by a confined and pinned ice shelf on the ice stream are the shearing force F_s along the ice stream–ice shelf boundary and the pinning force F_p exerted by ice rises on the ice shelf. Therefore

$$F_x = F_s + F_p \tag{124}$$

In the work by *Thomas* [1973*a*] the expression for F_s is obtained from (108); and since there are two shear zones,

$$\begin{aligned}F_s &\simeq -\int_{-H}^{h}\int_{-\Lambda}^{\Lambda}\int_{0}^{x}\left(\frac{\partial\sigma_{xy}}{\partial y}\right)dx\,dy\,dz \\ &\simeq -\frac{\tau_0}{\Lambda}(h+H)2\Lambda x = -2\tau_0 L_z x\end{aligned} \tag{125}$$

where $x = 0$ at the ice shelf grounding line and $(\partial\sigma_{xy}/\partial y) = \sigma_{xy}/y = \tau_0/\Lambda$ is assumed. In the work by *Thomas* [1973*b*] the expression for F_p was deduced from field data on the Brunt Ice Shelf as

$$F_p \simeq k/r^\kappa \tag{126}$$

where r is the radial distance from the ice rise pinning point and the value of F_p at a given r in a given direction is determined by constants k and κ. An ice rise significantly restrains the forward motion of an ice shelf over an arc of approximately 120° upstream from the pinning point.

As was shown for Byrd Glacier, viscoplastic instability can greatly reduce the restraining effect of F_s because σ_{xy} creates a strain-softened ice zone that lubricates the ice stream–ice shelf boundary. However, F_p should still be a major restraining force because σ_x creates a strain-hardened ice zone that fans out upstream from each pinning point. In fact, *Thomas* [1976] has shown that ice shelf pinning points probably play a decisive role in stabilizing marine ice sheets.

Note that $\dot{\epsilon}_x = 0$ when $\sigma_x = \sigma_z$ in (120). This situation exists when the constraints of the ice shelf exactly cancel the driving force of an ice stream merging with the ice shelf. Assuming that there are no ice rises pinning the ice shelf in this region so that $F_p = 0$ in (124), the distance x from the grounding line to the point where shear between the ice shelf and the floating part of the ice stream results in $\dot{\epsilon}_x = 0$ is obtained by combining (123), (124), and (125):

$$x = (\rho g h/4\tau_0)L_y \tag{127}$$

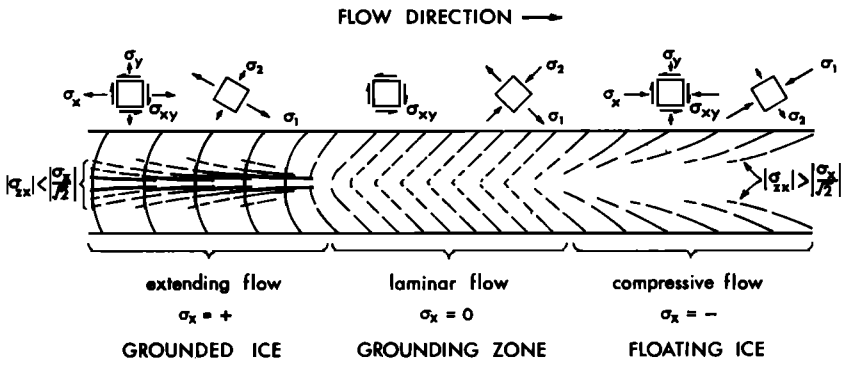

Fig. 24. Crevasse patterns in an outlet glacier ice stream related to stresses in the extending, laminar, and compressive flow regimes of its grounded, tidal, and floating portions, in a fjord of constant width. Longitudinal, transverse, and shear surface stresses are σ_x, σ_y, and σ_{xy} and resolve into principal surface stresses σ_1 and σ_2. Transverse-shear crevasses in the zone of grounded ice become pure shear crevasses in the tidal zone and longitudinal-shear crevasses in the zone of floating ice. Shear-longitudinal crevasses also form in the zone of grounded ice for outlet glaciers and for ice streams in which conservation of volume is not maintained by ice moving across the sides of the ice stream. Note that the envelope of longitudinal-shear crevasses is strongest along the sides and diverges in the downstream direction, but the envelope of shear-longitudinal crevasses is strongest along the center line and converges in the downstream direction. The compressive flow zone in the floating portion exists if the frictional drag along the fjord walls exceeds the gravity force pulling floating ice through the fjord. Therefore extending flow exists in both grounded and floating ice if viscoplastic instability largely uncouples the outlet glacier from the fjord walls by creating a lubricating band of strain-softened ice in the lateral shear zones.

At section Y-Y' across the floating part of Byrd Glacier, letting $h \simeq 100$ m, $\tau \simeq 0.42$ bar, and $L_y \simeq 26$ km in Figures 2 and 23 gives $x \simeq 140$ km. The distance from the Byrd Glacier grounding line to the end of the longest lateral rift in Figure 2 is $x \simeq 97$ km. Hence either pinning points exist in this region so that $F_p > 0$, or $F_s > 0$ for about 43 km beyond the longest lateral rift, or $F_s > 0.42$ bar along the rifts, or a combination of these factors exists. In any case, $\tau_0 > 0.42$ bar is expected beyond the ends of the lateral rifts where viscoplastic instability should transform the strain-softened ice along the rifts into the strain-hardened ice typical of ice shelves. That is, the single-pole ice fabric created by σ_{xy} in simple shear becomes a four-pole ice fabric created by σ_x in uniaxial extension, as shown in Figure 4.

c. Crevasse Patterns and the Surface Ice Stream Boundary

The *Hopkins* [1862] theory of crevasse patterns, which has been described and expanded by *Nye* [1952], assumes that the longitudinal tensile or compressive stress is substantially constant across an ice stream or outlet glacier. Figure 19 shows that these stresses generally decrease from the center to the side of an ice stream if flow is homogeneous. However, viscoplastic instability will tend to make the longitudinal stresses more constant across the ice stream because the easy glide ice fabric developed by σ_{xy} toward the sides of the ice stream is a hard glide ice fabric for σ_x. Hence strain softening for σ_{xy} is strain hardening for σ_x, and since σ_{xy} dominates toward the sides, σ_x must increase in these regions. This increase offsets the decrease in Figure 19 and is predicted by the flow curve in Figure 3. Therefore viscoplastic instability suggests that the Hopkins-Nye crevasse theory is correct, so it will now be applied to ice streams and outlet glaciers.

Consider a parallel sided ice stream. Let its thickness remain constant. Then $\dot{\epsilon}_z = 0$, so that $\dot{\epsilon}_x = -\dot{\epsilon}_y$ by (111) and $\sigma_x' = -\sigma_y'$ by (105). The effect of a tensile or compressive $\dot{\epsilon}_x$ along the ice stream is to make the ice stream contract (negative $\dot{\epsilon}_y$) or expand (positive $\dot{\epsilon}_y$) because the ice stream sides are defined by maximum slope surface inflection lines. This is the situation in Figure 18, where ice flowing across the sides of the ice stream completely accounts for the longitudinal strain rate. In this case the ice stream behaves as if its sides were free surfaces, so that $\sigma_y = 0$ at the surface. On the other hand, let the ice stream width remain constant. Then $\dot{\epsilon}_y = 0$, so that $\dot{\epsilon}_x = -\dot{\epsilon}_z$ by (111) and $\sigma_x' = -\sigma_z'$ by (105). Then the ice stream thins (negative $\dot{\epsilon}_z$) or thickens (positive $\dot{\epsilon}_z$) as $\dot{\epsilon}_x$ is tensile or compressive. This is the situation when an ice stream passes through a fjord where no ice flows across its sides. In this case the ice stream behaves as if its sides were rigid surfaces, so that $\sigma_y' = 0$ by (105) and $\sigma_y = \frac{1}{2}\sigma_x$ at the surface by both (106) and $\sigma_z = P = 0$ at the surface. In general both the width and the thickness change, so that $0 \leq |\sigma_y| \leq \frac{1}{2}|\sigma_x|$. The two extremes are $\sigma_y = 0$, if the ice stream laterally expands or contracts to relieve σ_y completely as σ_x changes, and $\sigma_y = \sigma_x/2$, if the ice stream sides remain fixed regardless of variations in σ_x.

Mohr's circles can be constructed to give the magnitude and direction of the maximum and minimum principal stresses σ_1 and σ_2, respectively, corresponding to the values of σ_x, σ_y, and σ_{xy} at various positions y across the ice stream plotted in Figure 18. Crevasses open normal to principal tensile stresses, with major cravasses normal to a tensile σ_1 and minor crevasses normal to a tensile σ_2. The relationships of σ_1 and σ_2 to σ_x, σ_y, and σ_{xy} are

$$\sigma_1 = \tfrac{1}{2}(\sigma_x + \sigma_y) + [\tfrac{1}{4}(\sigma_x - \sigma_y)^2 + \sigma_{xy}^2]^{1/2} \quad (128)$$

$$\sigma_2 = \tfrac{1}{2}(\sigma_x + \sigma_y) - [\tfrac{1}{4}(\sigma_x - \sigma_y)^2 + \sigma_{xy}^2]^{1/2} \quad (129)$$

Note that $2^{1/2}\sigma_{xy} = \sigma_x$ when $\sigma_x = 2\sigma_y$ and $\sigma_1 = 0$ or $\sigma_2 = 0$. Figure 24 shows the three categories of crevasse patterns expected for the three principal stress combinations.

In the pure shear crevasse category, $\sigma_x = 0$, so that $\sigma_y = 0$ and $|\sigma_{xy}| = \sigma_1 = -\sigma_2$. Crevasses are linear, are aligned at 45° to the ice stream sides, and gradually vanish toward the ice stream center line where $\sigma_{xy} = 0$.

In the extending flow crevasse category, σ_x is tensile, so that σ_y is tensile or zero. Since $\sigma_{xy} = 0$ along the center line of the ice stream, σ_x opens primary transverse crevasses, and σ_y opens secondary longitudinal crevasses in this region. As σ_{xy} increases toward the ice stream sides, these crevasses curve because they acquire an increasing shear component. The

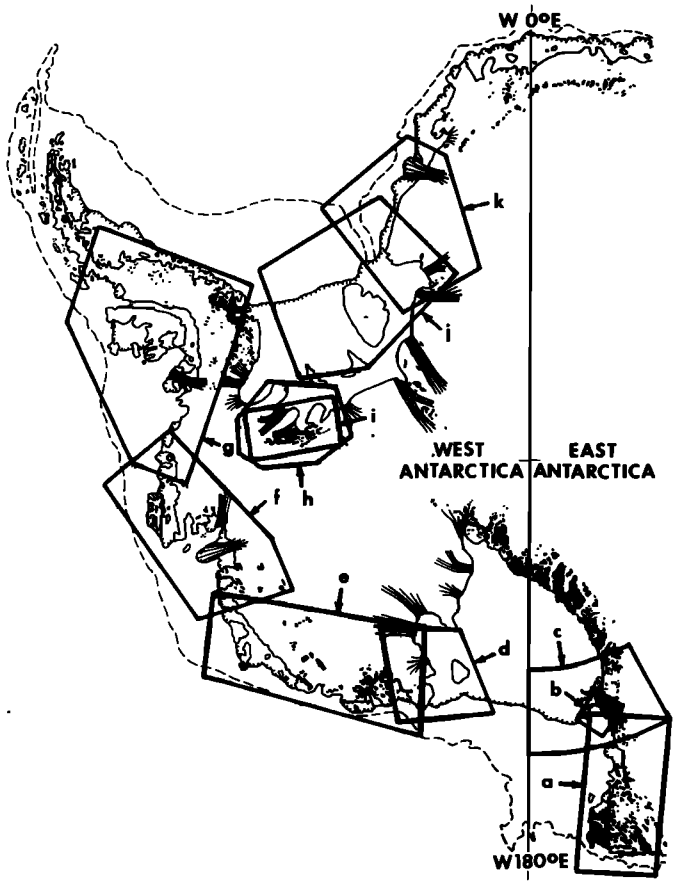

Fig. 25. Map showing locations of preliminary Landsat image mosaics assembled from ERTS 1 photography over West Antarctica and adjacent parts of East Antarctica.

primary crevasses therefore meet the ice stream sides at an angle between 45° and 90°, depending on the relative strength of σ_x and σ_{xy} along the sides. The secondary crevasses, being orthogonal to the primary crevasses, would meet the ice stream sides at angles between 0° and 45°, depending on the relative strength of σ_y and σ_{xy}. If σ_2 becomes compressive toward the ice stream sides, however, the secondary crevasses will die out with increasing distance from the center line. For example, in the case of an ice stream whose width is unaffected by σ_x variations, σ_2 is compressive when $2^{1/2}\sigma_{xy} > \sigma_x = 2\sigma_y$.

In the compressive flow crevasse category, σ_x is compressive, so that σ_y is compressive or zero, and σ_{xy} is the only stress component capable of making σ_1 tensile. Since $\sigma_{xy} = 0$ along the center line of the ice stream, no tensile principal stresses exist in this region, so no crevasses can form. However, as σ_{xy} increases toward the sides of the ice stream, shear crevasses having a compressive component can open. The compressive component bends the shear crevasses in the opposite sense to that expected by a tensile component, so that the crevasses intersect the ice stream sides at an angle between 0° and 45°. These crevasses will not form until σ_1 is tensile, which occurs when $2^{1/2}\sigma_{xy} > \sigma_x = 2\sigma_y$.

All but a few West Antarctic ice streams are absorbed by confined and pinned ice shelves, and so it is expected that their grounded portion ($0 < k < 1$ in (88)–(90)) will experience extending flow and their floating portion ($k = 0$ in (88)–(90)) will experience compressive flow. The surface crevasse pattern should change accordingly. To refer to Figure 24, therefore, the tension-shear pattern should predominate in the grounded portion, the pure shear pattern should predominate across the portion where ungrounding occurs, and the compression-shear pattern should predominate in the floating portion. Photo interpretation of ice stream crevasse patterns can therefore in principle be used to obtain an initial impression of the location and width of the ice dome–ice shelf junction for a given ice stream. In fact, ice stream dynamics are rarely so simple. Since the aerial photographs are taken at an instant of time, they show the location and width of the grounding zone at a specific point in the tidal cycle along the ice dome–ice shelf junction. Ice thinning caused by tidal flexure may localize and magnify the crevasse pattern caused by the transition from extending flow to compressive flow across the junction, especially if the widths of the tidal zone and grounding zone are comparable [*Thiel and Ostenso,* 1961]. Tidal flexure stress fields must therefore also be considered.

7. Photo Interpretation of Ice Streams Using ERTS 1 Imagery

a. Viscoplastic Instability in Ice and Glacial Crevasse Patterns

Theoretical investigations presented in the preceding sections can be field tested through the use of aerial photographs taken from artificial satellites in polar or near-polar orbits. The theoretical investigations related crevasses in ice streams and outlet glaciers to viscoplastic instability in polycrystalline ice and reached five conclusions. (1) Slow steady state creep is unstable because it is controlled by hard glide, which is a condition of viscoplastic instability between transient and transitional creep. (2) Transitional creep begins with viscoplastic instability at the upper yield stress and occurs during recrystallization from an ice fabric in which the strain rate is controlled by hard glide to one in which the strain rate is controlled by easy glide. (3) Transitional creep ends in fast steady state creep at the lower yield stress, which is stable because it is controlled by easy glide. (4) Fracture is expected in zones of viscoplastic instability because of the accelerated strain rates which accompany ice recrystallization. (5) Fracture causes transverse crevasses along a grounded ice stream, shear crevasses along ice stream sides, and either longitudinal or transverse crevasses along a floating ice stream, depending on whether or not it merges with a confined and pinned ice shelf. Crevasses are among the more easily recognizable features in the Landsat image mosaics reproduced in Figure 26. These mosaics were obtained from ERTS 1 photographs through the courtesy of W. R. MacDonald and the United States Geological Survey. The index map gives their locations. *Southard and MacDonald* [1974] and *MacDonald* [1976*a*, *b*, *c*] have described ERTS 1, presented maps of the polar areas covered by ERTS 1 space imagery, and given examples of how image mosaics can be used to improve mapping, monitor meteorological conditions, and study ice dynamics in the Antarctic.

Figure 26 presents reproductions of preliminary Landsat image mosaics for West Antarctica and the adjacent parts of East Antarctica which are important in addressing the question, 'Is the West Antarctic ice sheet disintegrating?' Unfortunately, areas in latitudes higher than 80°S are not scanned by ERTS 1, and some of the details in latitudes which are scanned have been lost in the reproduction process. In the discussion which follows the original image mosaics should be examined when the features described are not visible in Figure 26. The original image mosaics are in the 1:500,000 to 1:1,000,000 scale range, for which crevasse and flow patterns in the Antarctic ice dome–ice stream–ice shelf system are clearly visible.

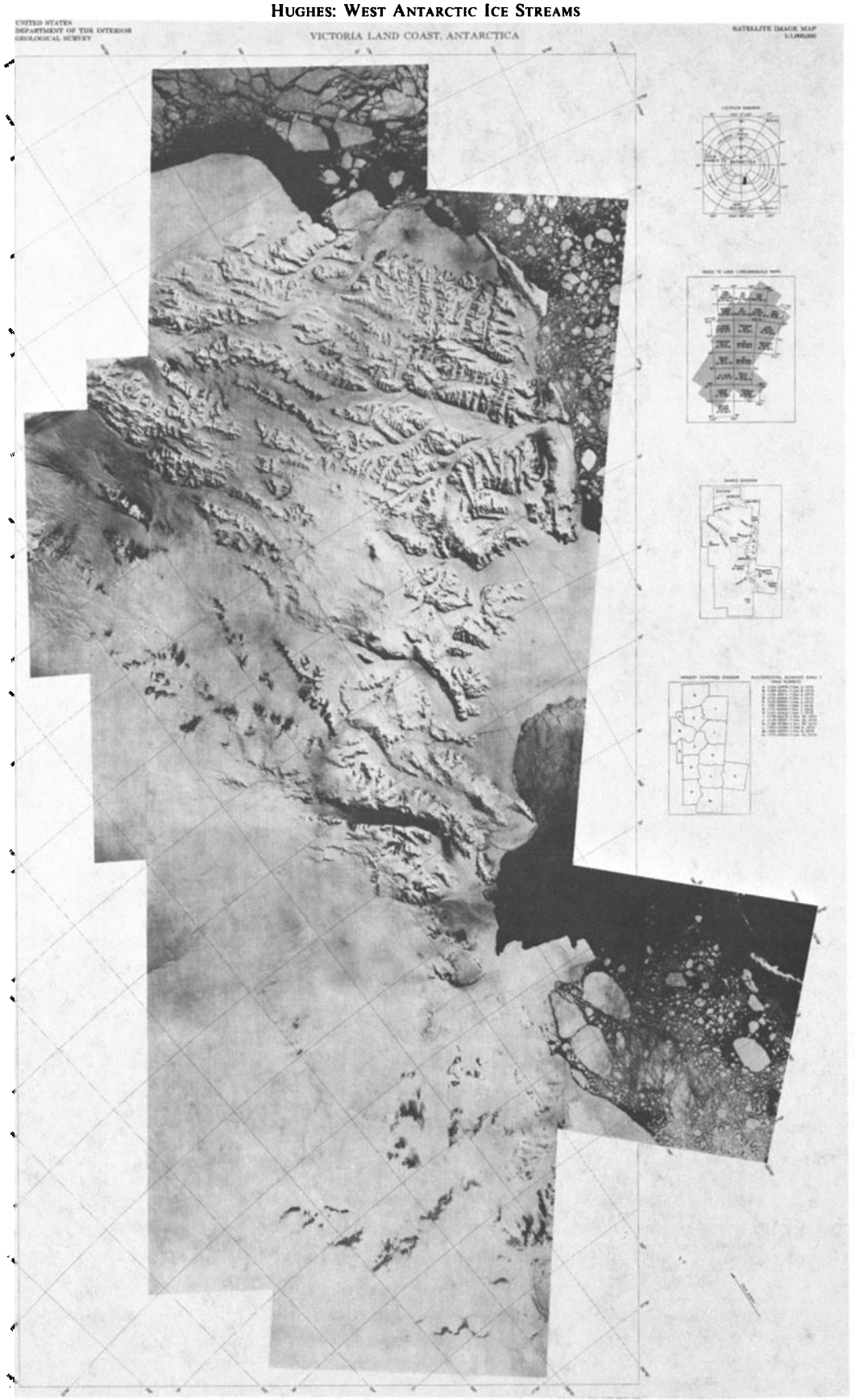

Fig. 26*a*. Victoria Land coast; scale, 1:1.000,000.

Fig. 26. Reproductions of preliminary Landsat image mosaics assembled from ERTS 1 photography over West Antarctica and adjacent parts of East Antarctica. These reproductions were reduced from 1:500,000 to 1:1,000,000 scale image mosaics provided through the courtesy of William R. MacDonald and the United States Geological Survey. The preliminary Landsat (ERTS) image mosaics were compiled by W. R. MacDonald under experiments conducted under USGS/NASA proposal SR-149, 'Cartographic Application of ERTS/RBV Imagery in Polar Regions,' January 1, 1972.

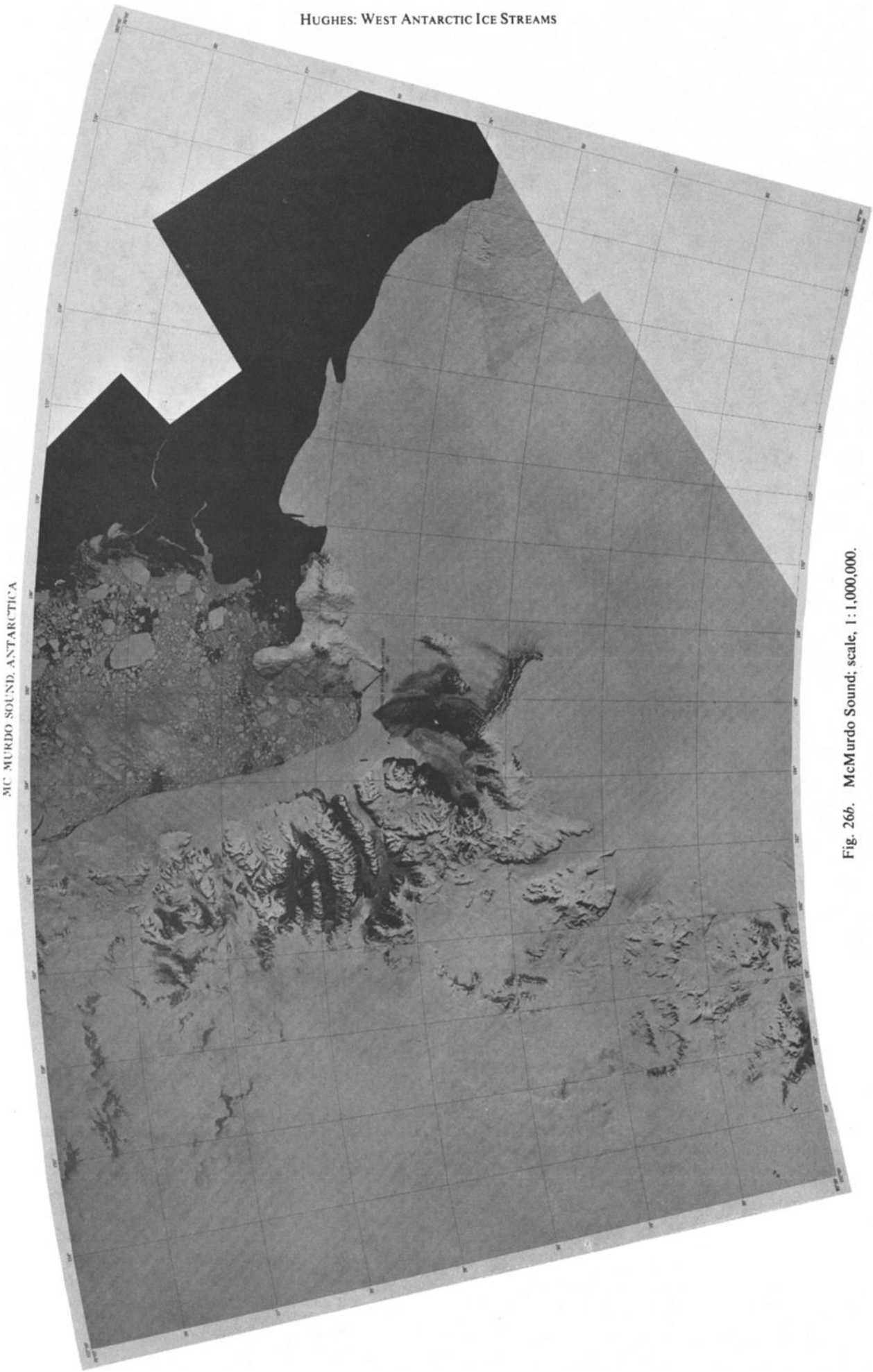

Fig. 26*b*. McMurdo Sound; scale, 1:1,000,000.

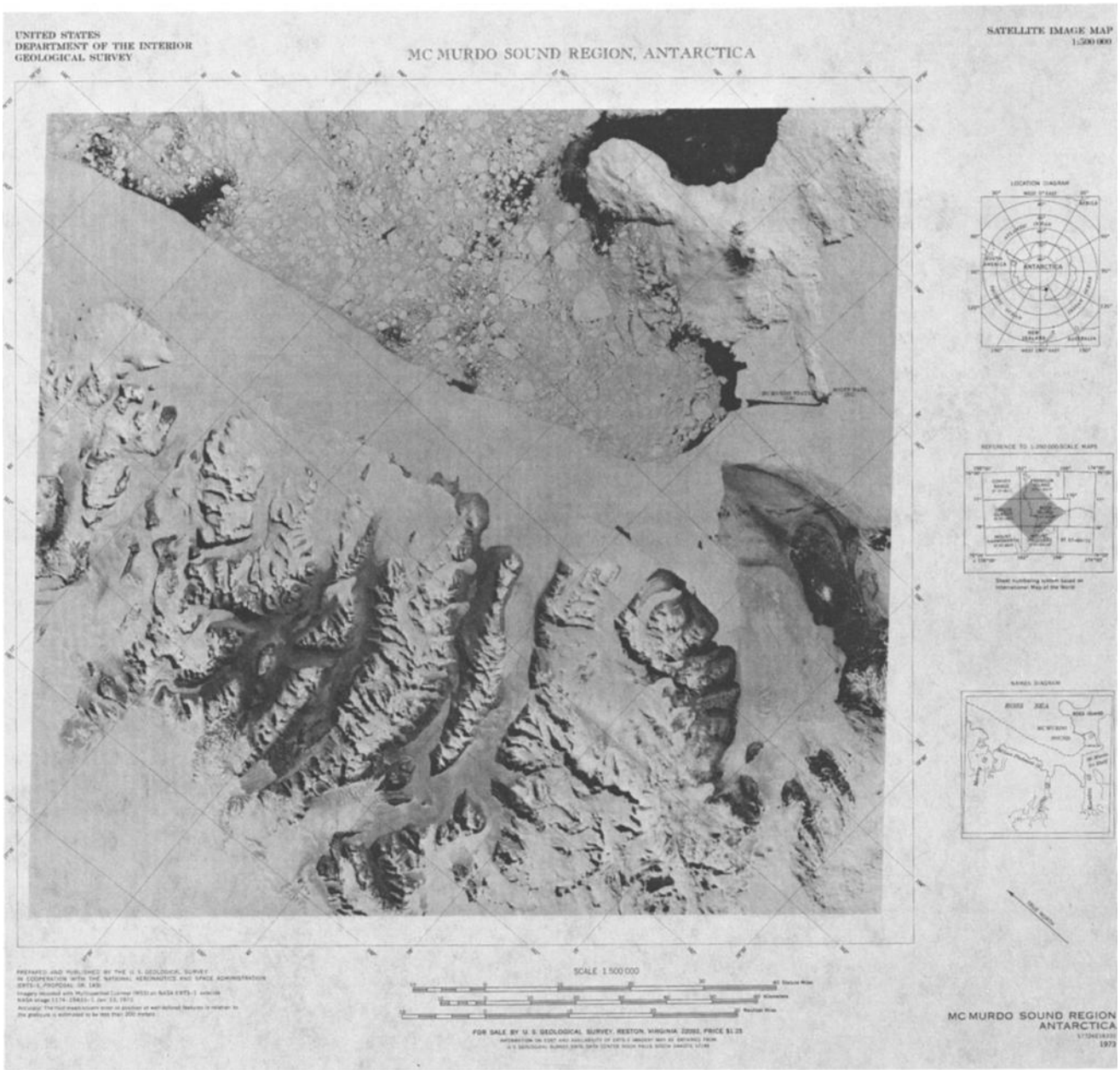

Fig. 26*c*. McMurdo Sound region; scale, 1:500,000.

b. Distinguishing Ice Shelf Grounding Lines by Crevasse Patterns

According to the tidal flexure analysis in section 4, a primary tidal flexure crevasse is expected along the grounding lines of ice shelves and floating ice streams or outlet glaciers, where the angle between floating ice and the sea floor is expected to be large, so that to and fro oscillations of the junction during tidal cycles will be small. Secondary tidal flexure crevasses on the ice shelf may occur in zones parallel to the ice shelf grounding lines, crevasse depth decreasing in successive zones. Only one or two zones of secondary tidal flexure crevasses have been observed [*Swithinbank*, 1955]. By themselves, tidal flexure cracks are small, but they may perturb the general stress field enough to cause massive stress relief via crevassing in the tidal zone. Hence the band of intensive crevassing along the tidal zone may be several kilometers wide, enough to be detected by ERTS 1 imagery. Bands do appear around Roosevelt Island and Berkner Island in Figures 26*d* and 26*j*. These islands are known grounded ice domes surrounded by the Ross and Filchner-Ronne ice shelves, respectively, so it is quite possible that the bands represent zones of tidal flexure crevasses accentuated by shear crevasses caused by ice flowing around these domes. Hence such bands in the ERTS 1 imagery may identify other grounding lines for these ice shelves. Figures 26*e*, 26*f*, and 26*g* show similar bands along West Antarctic coasts in the Amundsen and Bellingshausen seas, where ice shelves abut glaciated islands. These bands are also probably zones of tidal flexure and shear crevasses along ice shelf grounding lines [*Thiel and Ostenso*, 1961].

Surface crevasses identify the major ice streams which feed the ice shelves fringing West Antarctica. These ice streams

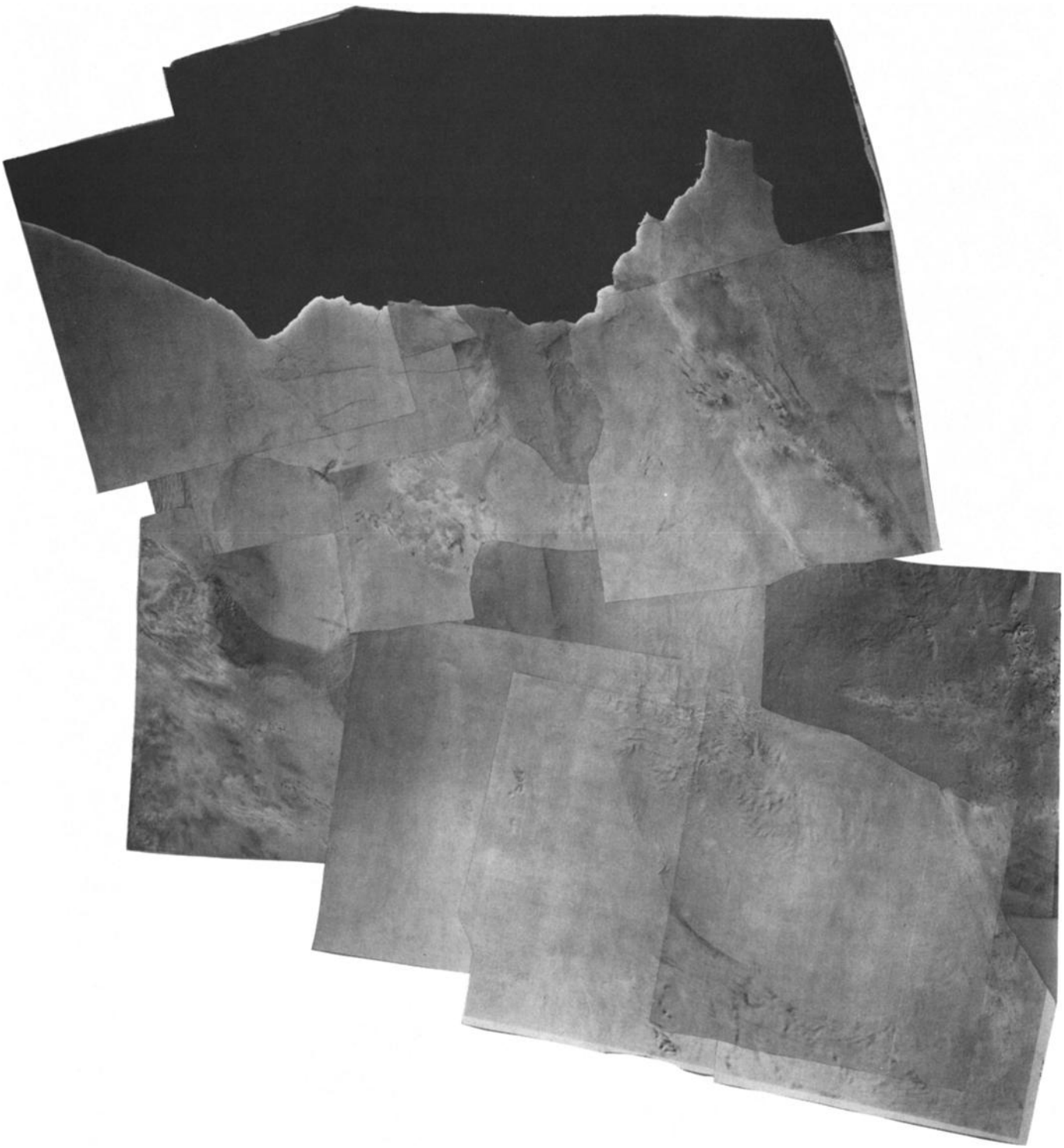

Fig. 26*d*. Roosevelt Island–Mount Siple.

Fig. 26*e*. Roosevelt Island–Mount Siple.

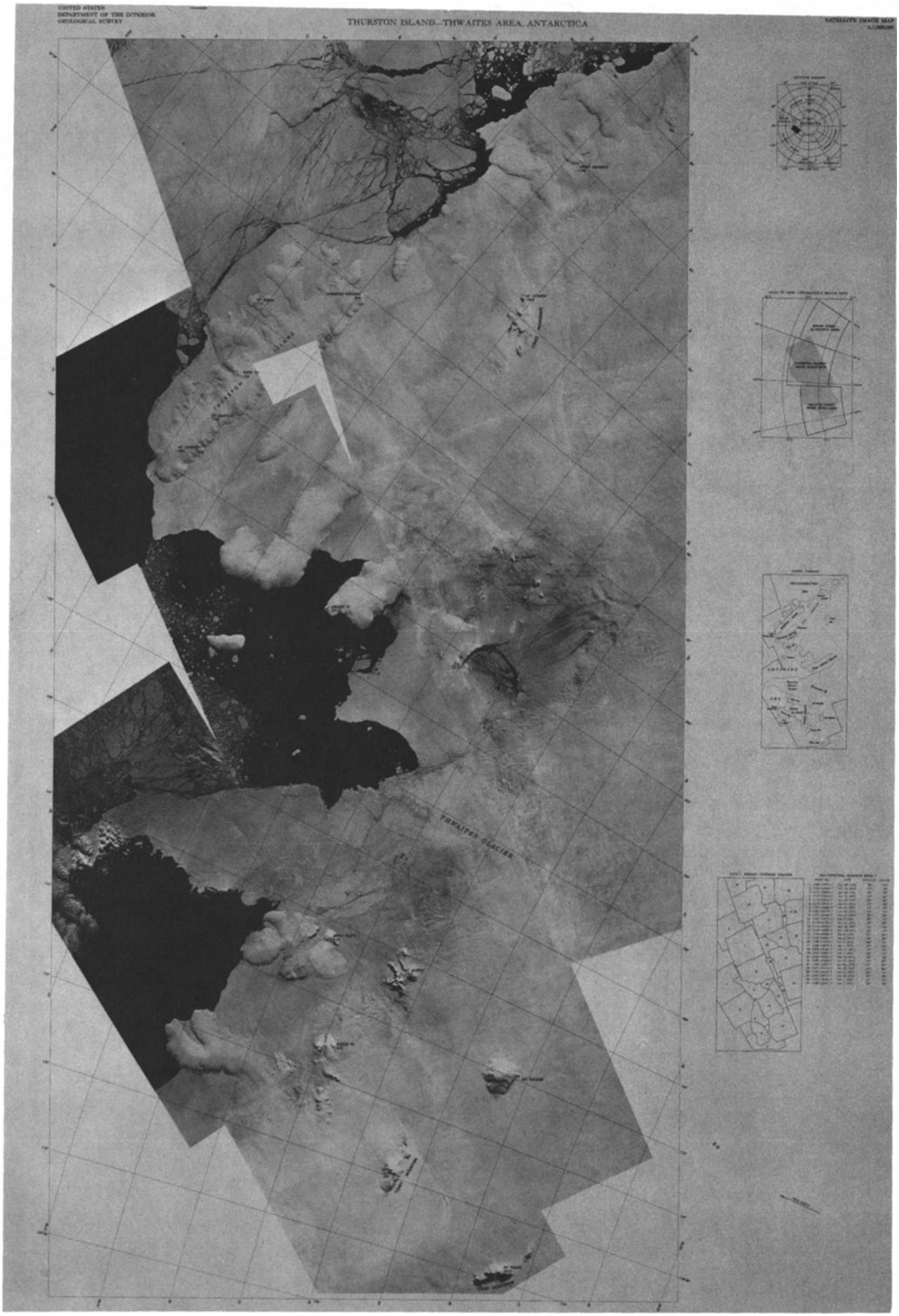

Fig. 26*f*. Thurston Island–Thwaites area; scale, 1:1,000,000.

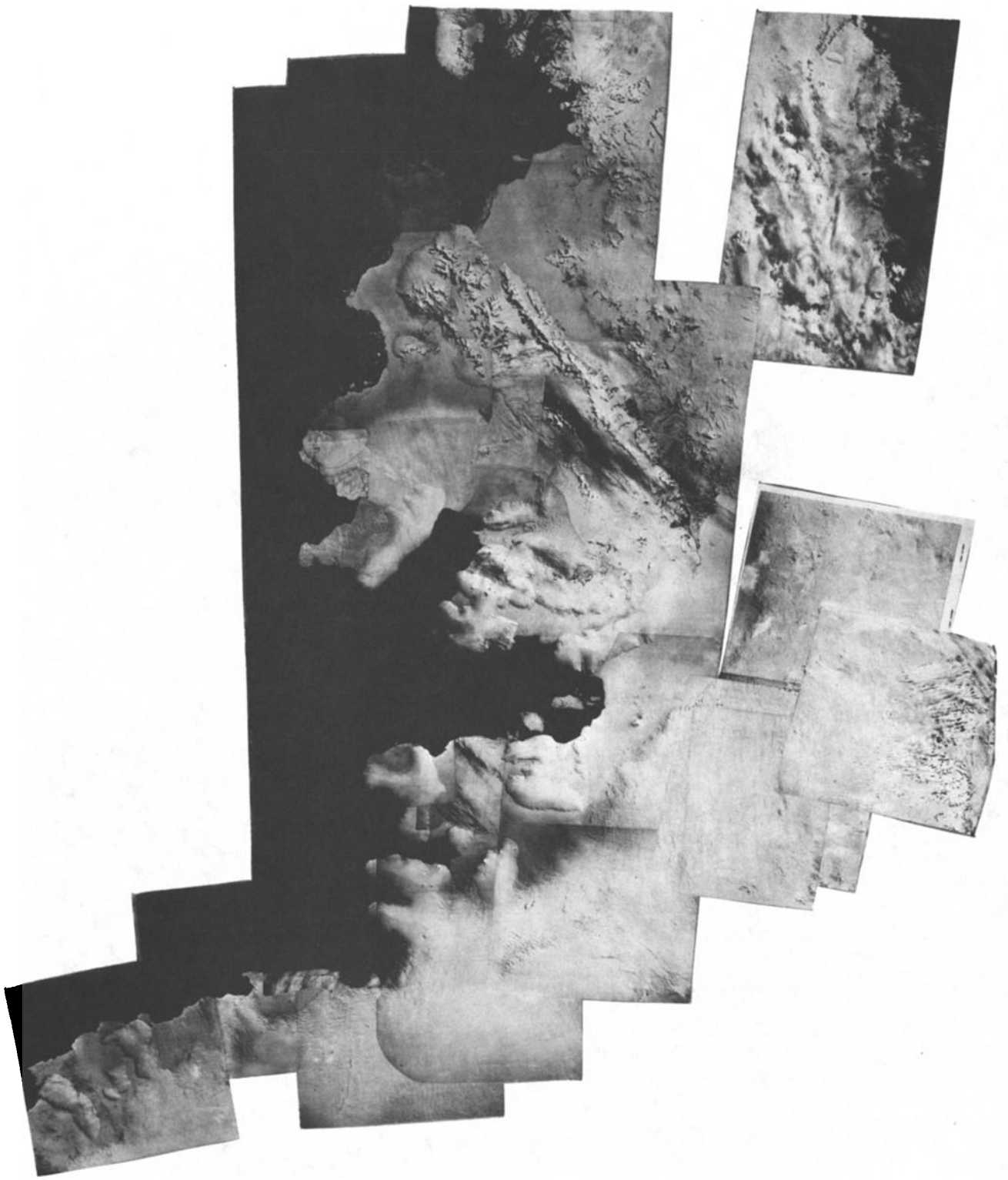

Fig. 26g. Alexander Island–Palmer Peninsula.

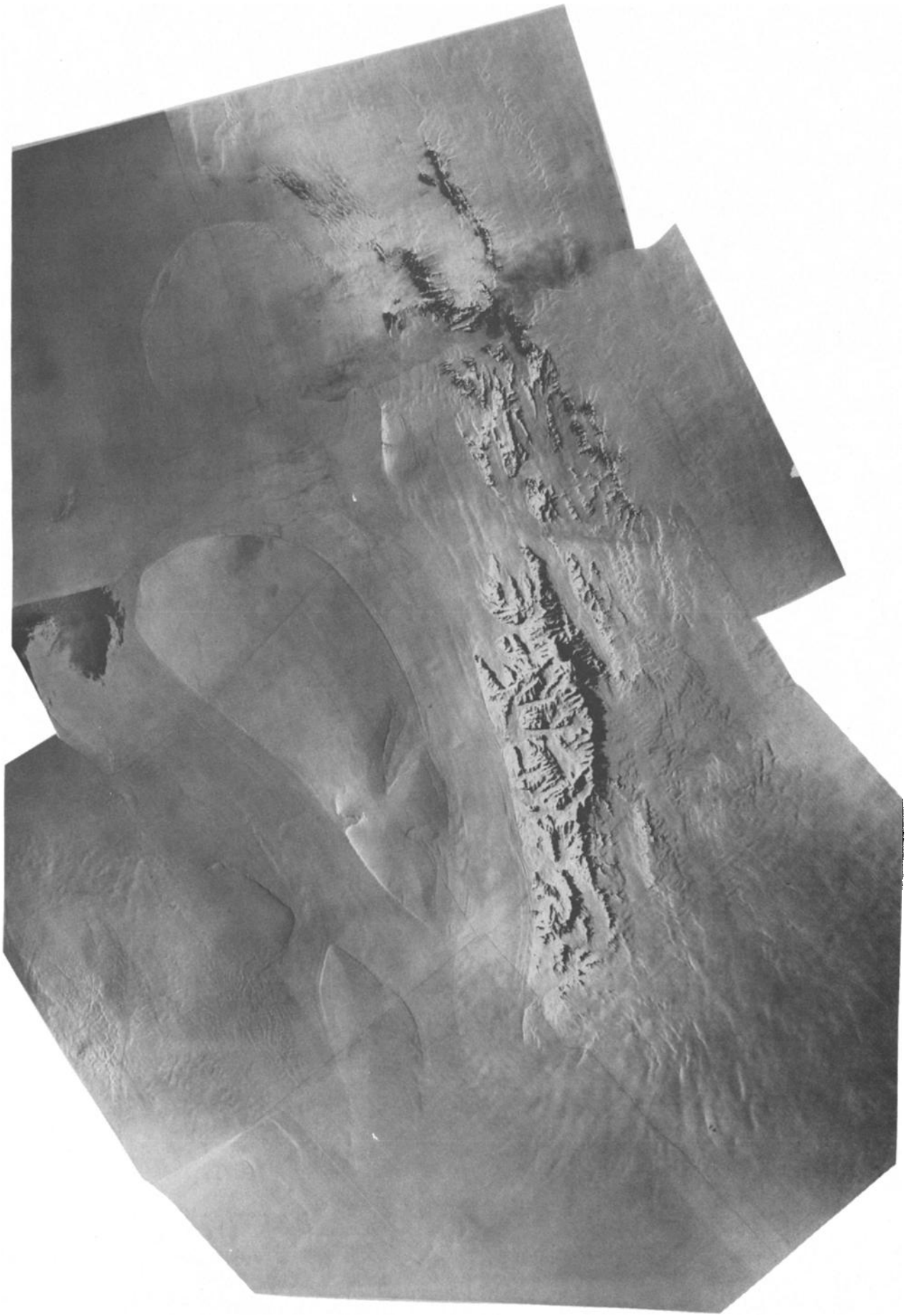

Fig. 26*a*. Ellsworth Mountains; scale, 1:500,000.

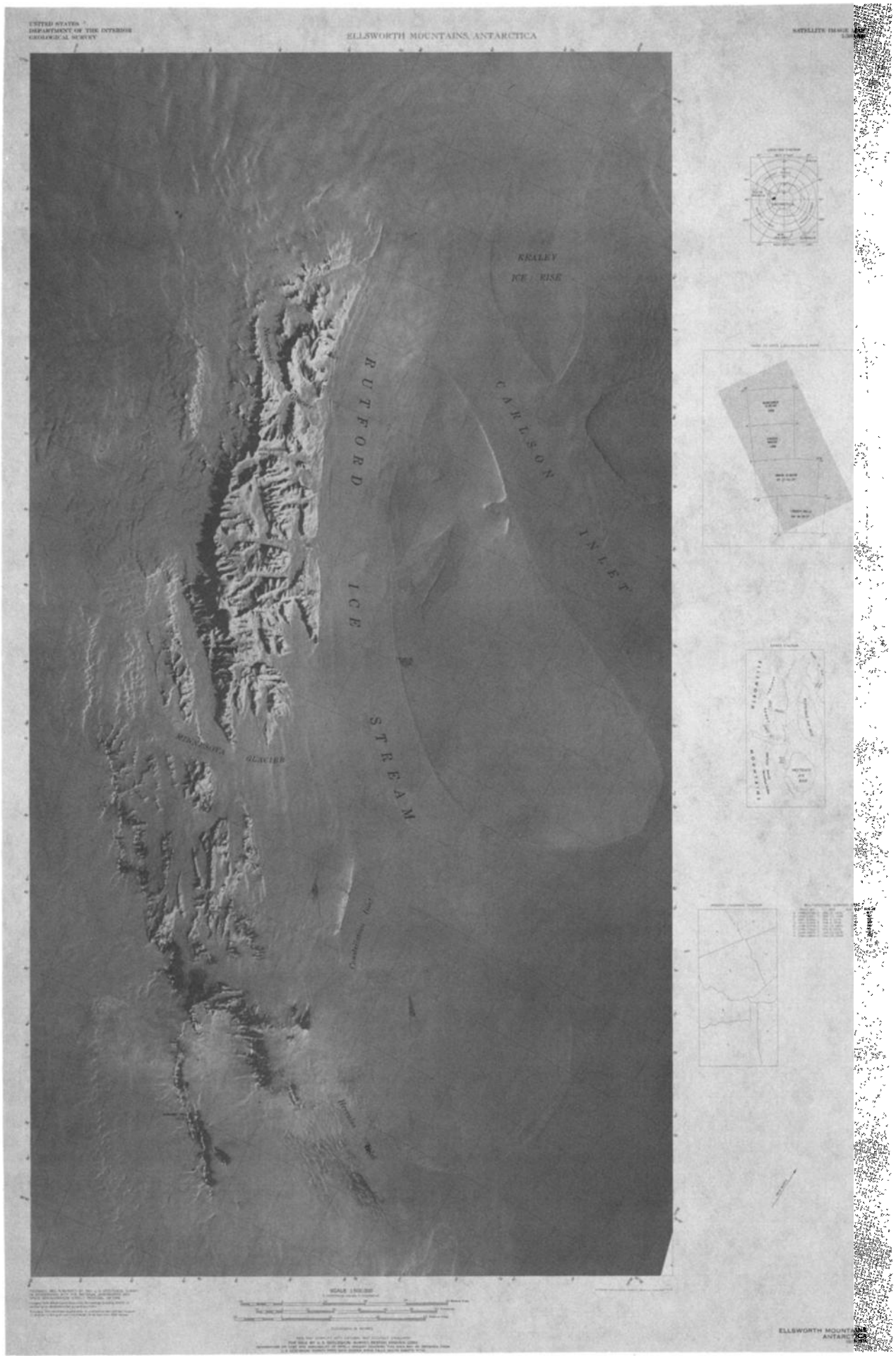

Fig. 26*i*. Ellsworth Mountains; scale, 1:500,000.

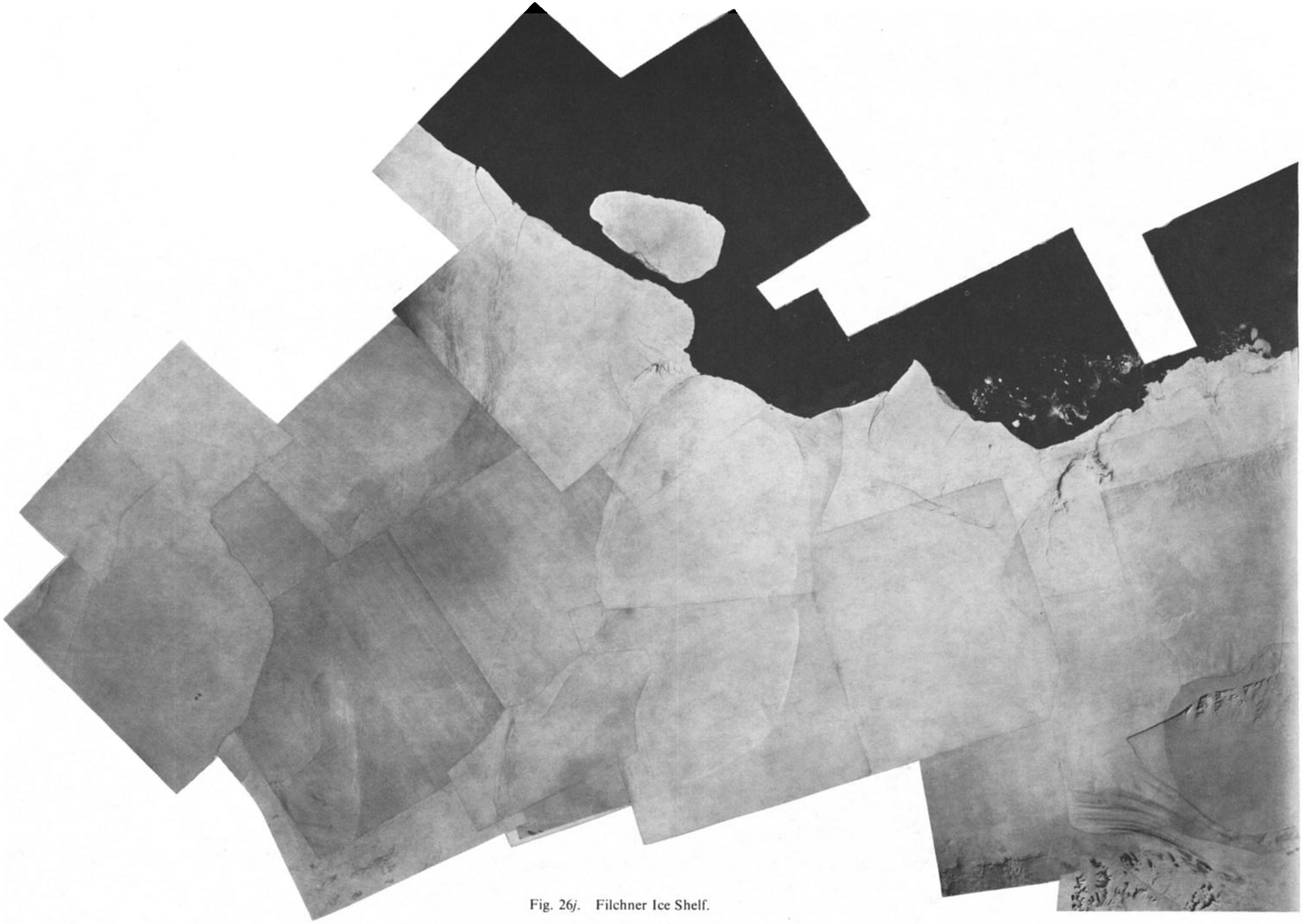

Fig. 26*j*. Filchner Ice Shelf.

Fig. 26*k*. Filchner Ice Shelf.

begin on the ice domes and end in the ice shelves, so they are partly grounded and partly afloat. Transverse grounding lines for the floating portions cannot generally be detected across ice streams because the angle between the ice shelf and the sea floor is often so small that grounding occurs across a broad zone that oscillates with the tide. Tidal flexure is therefore minimized, and any tidal flexure cracks which do form would probably be indistinguishable from transverse crevasses caused by extending flow in the ice stream. However, longitudinal grounding lines alongside ice streams are generally narrow with minimal tidal oscillation because the angle between the ice shelf and the bed is a maximum on the sides of bedrock channels eroded by ice streams. Tidal flexure is therefore maximized, and tidal flexure cracks will probably localize shear crevasses in rifts alongside the ice stream. These rifts will disappear upstream across the transverse grounding zone of the floating ice stream, allowing this zone to be located even though transverse tidal flexure crevasses may not exist in the zone. When this logic is applied to West Antarctic ice streams in Figures 25 and 26, it seems clear that Carlson Inlet in

Figures 26*h* and 26*i* is probably a forked ice stream, with Kealey Ice Rise at the fork. Hence Fletcher Ice Rise separating Carlson Inlet from Rutford Ice Stream is a grounded lobe of the West Antarctic ice sheet. Kealey and Fletcher ice rises are not true ice rises completely surrounded by the Ronne Ice Shelf because the bands identified with tidal zones do not surround them completely.

c. Distinguishing Outlet Glacier Ice Streams by Crevasse Patterns

Ice streams become outlet glaciers when they flow in fjords through coastal mountains because an ice sheet usually covers coastal islands but not coastal mountains. Hence ice streams that become outlet glaciers have rock sides instead of ice sides. However, suppose that an ice stream has rock walls partway up its sides and ice walls the rest of the way up. Does it behave like an outlet glacier? A practical decision can be made by comparing the observed surface crevasse pattern with the patterns predicted for free and rigid side boundaries. As shown in Figure 24, these crevasse patterns are identical except that longitudinal crevasses form during extending flow in outlet glaciers because ice pulls away from the rock walls. Without rock walls, ice would move laterally to replace the lateral contraction resulting from longitudinal extension. Transverse crevasses denote extending flow for both ice stream boundary conditions. Hence if an ice stream has both transverse and longitudinal crevasses in the same region, this region is behaving more like an outlet glacier, so that its sides are bounded by subglacial mountains close to the surface.

This is an important result from analyzing crevasse patterns because outlet glaciers generally cross a high bedrock upward step when they pass between coastal mountains, even if the mountains are subglacial, whereas low bedrock up-down sills usually exist where ice streams pass between coastal islands. The retreat of an ice shelf grounding line which accompanies surges of ice streams is halted by a high bedrock sill or step. Hence an outlet glacier surge is stabilized by its high bedrock step, but other ice stream surges can propagate into the heart of the marine ice sheet unless a high bedrock sill exists in the ice stream channel. Both Thwaites Glacier and Pine Island Glacier in Figure 26*f* and Stancomb-Wills Glacier in Figure 26*k* have punched through their confining ice shelf fringes and seem to be surging ice streams. Why have their grounding lines not retreated inland to create huge ice shelves comparable to the Ross and Filchner-Ronne ice shelves created by surges of the ice streams in Figures 26*d*, 26*h*, 26*i*, and 26*j*? The answer is that Thwaites, Pine Island, and Stancomb-Wills glaciers are outlet glacier ice streams passing between subglacial islands or mountains, as revealed by their longitudinal crevasses. Hence high bedrock sills or steps have probably checked grounding line retreat.

d. Monitoring Calving Bay Stability From Crevasse Patterns

Calving bays develop when an ice stream punches through the ice shelf fringing marine portions of an ice sheet and begins to surge. ERTS imagery can be used to monitor calving bays when they develop, and the crevasse patterns that develop will determine whether the calving bay exists in stable, unstable, or metastable equilibrium. As is shown in Figure 27, an ice stream merging with an ice shelf at the edge of the continental shelf is stabilized by the buttressing effect of the ice shelf, frictional drag along the ice stream sides, and a low bedrock sill where the ice stream becomes ungrounded. The ice stream is in unstable equilibrium because it will surge if critical thresholds are exceeded in these boundary regions. If the ice shelf narrows by calving, the ice stream can punch through it. If viscoplastic instability occurs in its lateral shear zones, strain softening largely uncouples the ice stream along its sides. If relative sea level rises sufficiently, the ice stream grounding line will retreat over the bedrock sill. The ice stream is in unstable equilibrium if the resulting surge causes catastrophic retreat of the ice stream grounding line and of the maximum slope inflection line at the ice stream–ice dome junction because these retreats draw down the marine portion of the ice sheet. The ice stream is in stable equilibrium when its retreating grounding line stops at the high bedrock step separating the marine and terrestrial portions of the ice sheet. This step usually occurs at the end of a fjord through coastal mountains that often form the boundary between a continental shield and a continental shelf. The ice stream then becomes an outlet glacier. As is suggested by Figure 1, Byrd Glacier probably had this history.

Monitoring crevasse patterns for the ice streams in Figures 25 and 26 by using ERTS imagery over a period of years will identify calving bays as they develop and will determine whether they are stable, unstable, or metastable. At present, stable calving bays are expected for outlet glaciers draining East Antarctica through the Transantarctic Mountains, unstable calving bays are expected for ice streams draining West Antarctica along deep bedrock troughs in sectors of the Ross and Weddell seas, and metastable calving bays are expected for ice streams draining West Antarctica over low narrow bedrock sills in sectors of the Amundsen and Bellingshausen Seas. This is because East Antarctica is basically a continental shield fringed by mountains and West Antarctica is basically a continental shelf fringed by island arcs.

Calving bays were first described by *Hoppe* [1948] in reconstructing deglaciation of the Scandinavian ice sheet over the Gulf of Bothnia. Calving bays fringe the West Antarctic ice sheet because it is a marine ice sheet [*Mercer*, 1968] whose margin is grounded far below sea level. Ice streams typically drain marine ice sheets [*Hughes*, 1973*b*, 1975*a*] and can easily plow through normal pack ice covering polar oceans. Ice streams fringing marine ice sheets have an inherent tendency to surge when relative sea level exceeds a critical value [*Weertman*, 1974], and these surges cannot be contained by pack ice. However, ice stream surges might be restrained by an ice shelf lying in a confining embayment, frequently grounded on pinning points in the embayment and having a grounding line thickness comparable to the ice stream thickness. In such cases a steady state calving bay extends along the ice shelf barrier where icebergs are released. However, ice shelves are nearly flat, so that if minor warming of the air along the ice shelf margin moves the top surface equilibrium line above the calving barrier, this equilibrium line immediately moves from the calving barrier to near the grounding line. Similarly, minor warming of the ocean along the calving barrier can cause a major retreat of the bottom surface equilibrium line under the ice shelf. Thus ice shelves exist in metastable equilibrium; their calving margins are stable for small temperature perturbations but become unstable when a critical temperature perturbation is exceeded. When this happens, a formerly steady state calving bay becomes a catastrophic calving bay that migrates landward or seaward in response to a critical degree of climatic warming or cooling.

Landward migration of a catastrophic calving bay brings the calving barrier of an ice shelf closer to its grounding line. Eventually, the surging ice streams can punch through the ice shelf because tidal flexure–lateral shear crevasses along the

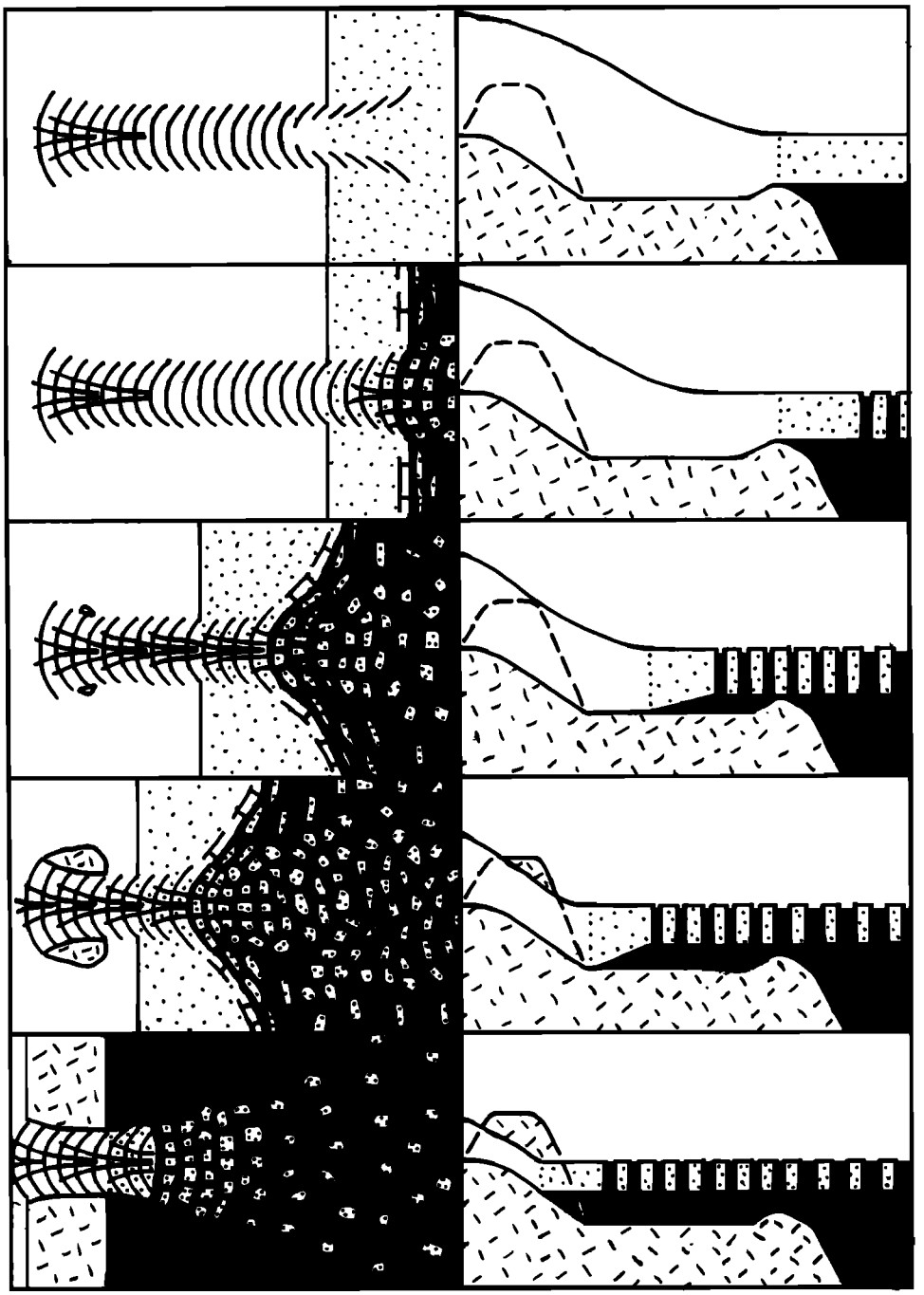

Fig. 27. The development of a calving bay from an ice stream surge in the marine portion of an ice sheet. Successive stages are shown in (left) surface plan and (right) longitudinal profile pairs proceeding from top to bottom. White areas are grounded ice, dotted areas are floating ice, black areas are seawater, checked areas are bedrock, and line segments are surface crevasses. This ice stream begins as an outlet glacier in a fjord through coastal mountains and continues across the continental shelf to merge with an ice shelf beyond the continental slope. Ice stream erosion creates a bedrock step at the rear of the fjord and a bedrock sill at the front of the continental shelf. A calving bay begins when the ice stream punches through the ice shelf and surges. The surge draws down the ice sheet so that the ice shelf grounding line migrates over the low bedrock sill, sweeps across the continental shelf, retreats into the fjord, and stops at the high bedrock step. The retreating grounding line converts the marine portion of the ice sheet into an ice shelf. A calving bay follows the retreating grounding line and sections the ice shelf into tabular icebergs along crevasses created by stress fields in the ice stream and along the ice shelf margin.

floating part of the ice stream uncouple it from the ice shelf for considerable distances, as shown by the rifts between Byrd Glacier and the Ross Ice Shelf in Figure 2. Ice stream surges are then no longer effectively contained by the ice shelf and can increase their velocity manyfold. The accelerated surge rapidly draws down the marine ice sheet, allowing the calving bay to follow the ice stream grounding line into the heart of the ice sheet. Hence a relatively minor climatic fluctuation along the ice shelf calving barrier can unleash glacial dynamic processes independent of climate that cause calving bays to remorselessly carve out the living heart of a marine ice sheet. Each stage of this process can be monitored for West Antarctica from ERTS 1 imagery. The transition from a steady state to a catastrophic calving bay is recorded as a massive fluctuation

of an ice shelf calving margin. An ice stream surge is recorded as a rapid increase in surface crevasse density. An ice stream punching through an ice shelf is recorded by the changing pattern of surface crevasses as extending flow replaces compressive flow in the floating portion. Disintegration of the West Antarctic ice sheet is recorded as retreat of crevasses along the grounding zone of its fringing ice shelves.

8. Discussion

This review subscribes to the research strategy outlined by *Fletcher* [1972] for studying dynamic systems. In his strategy the critical questions to be answered are in order.

1. What are the most energetic parts of the system?
2. What factors force the motion of these parts?
3. Are any of these factors subject to time variations?
4. What physical processes are associated with these variations?
5. To what extent can these processes be described quantitatively?
6. What observational tests can be designed to evaluate concepts of how the dynamic system works?

Ice streams apparently discharge nearly 90% of West Antarctic ice into the sea, particularly ice feeding the Ross Ice Shelf [*Hughes*, 1972*a*, pp. 31–32]. They are probably the most energetic parts of the Antarctic ice sheet [*Hughes*, 1973*a*, pp. 56–67]. They are also the most likely parts to become unstable and cause a surge of the ice sheet [*Hughes*, 1973*a*, pp. 26–47]. Instability probably originates along the maximum slope inflection lines which separate the ice stream from the ice dome [*Hughes*, 1973*a*, pp. 48–67] and along ice dome–ice shelf junctions which separate the grounded and floating portions of ice streams [*Hughes*, 1973*a*, pp. 68–85]. Inflection lines and grounding lines are probably the most energetic parts of ice streams.

Factors forcing the motion of ice streams are not well understood, but the main factor causing ice streams to move so fast is probably a progressive uncoupling of the ice from the bed. Since all West Antarctic ice streams are grounded below sea level, a thickening water layer separates the ice from bedrock as uncoupling progresses. The basal shear stress cannot be transmitted across this water layer, so the ice stream accelerates as the water layer thickens. A full-scale surge of the six major West Antarctic ice streams feeding the Ross Ice Shelf is probably restrained only by their energy dissipation in this ice shelf [*Robin*, 1975]. The elevation difference along an ice stream, the temperature difference across an ice stream, and the convergence of flow toward an ice stream are the factors in the vertical longitudinal plane, the vertical transverse plane, and the horizontal plane, respectively, which cause the ice stream to become uncoupled from its bed. But just how these factors operate and interact is an unanswered question.

Time variations in the forcing factors pinpoint a critical philosophical question, examined elsewhere [*Hughes*, 1973*a*, pp. 14–29]. Is the ice dome–ice stream–ice shelf system in fundamental equilibrium? If so, most time variations would probably not lead to any massive instability in the system because they would be reversible perturbations of a stable regime. But is the ice dome–ice stream–ice shelf system in fundamental disequilibrium and continually in search of an equilibrium state? In this case, some time variations would probably change the dynamics of the whole system in a fundamental way because they would be irreversible perturbations of an unstable regime. The true state of equilibrium for the system is probably a balance of stabilizing and destabilizing tendencies inherent in dynamic systems having stable, unstable, and metastable components. In general, short-term variations, such as the influence of tidal cycles on the ice dome–ice shelf junction, cannot cause irreversible perturbations of the system because they reverse before the system can fully respond to their effects. Long-term variations, such as the isostatic response of bedrock to absolute migration of ice dome–ice stream surface inflection zones or ice shelf–ice stream grounding zones, can cause irreversible perturbations of the system even if the variations are slow. Hence the ice dome–ice stream–ice shelf system is probably fundamentally stable for short-term variations and fundamentally unstable for long-term time variations. This is the condition of metastable equilibrium. If the West Antarctic ice dome–ice stream–ice shelf dynamic system exists in this condition, a critical question is what scale of time variations of what forcing factors irreversibly changes the energy balance of the system.

The physical processes associated with time variations of the forcing factors which move the ice dome–ice stream–ice shelf system can be classified as external and internal processes. The external processes are climatic changes over the ice sheet (changes in atmospheric albedo, storm patterns, temperature, precipitation, and solar input), tectonic changes under the ice sheet (changes in isostatic equilibrium, geothermal flux, episodic volcanism, and crustal plate migration), and oceanographic changes around the ice sheet (changes in sea ice distribution, sea level, currents, temperature, and salinity). The internal processes are changing flow patterns (resulting from migrations of ice margins, ice streams, ice domes, and ice divides), changing temperature fields (resulting from changes in the distribution of meltwater over the bed, changes in bed topography due to glacial erosion-deposition processes, and possibly from changing thermal convection regimes in the ice sheet), and changing velocity distributions (resulting from the changing flow patterns and temperature fields). All the internal and external physical processes interact to create various positive and negative feedback mechanisms in the ice dome–ice stream–ice shelf system.

Quantitative descriptions of the feedback mechanisms must rely on numerical modeling using high-speed computers. Finite difference modeling seems best suited for treating the dynamics of the ice dome–ice stream–ice shelf system as a whole, but finite element modeling promises to give a deeper insight into the most energetic parts of the system. Any phenomenon in nature can be analyzed quantitatively by using two distinct approaches. On the one hand, the phenomenon can be idealized and simplified so that an exact analytical solution to an approximation of the phenomenon is possible. On the other hand, the phenomenon can be modeled so that an approximate numerical solution to the actual phenomenon is possible. In general, an analytical solution of the idealized problem is necessary before a numerical solution of the real problem is possible, because the major features of the problem must first be understood. This is usually possible if the problem is idealized. Hence this review outlines several idealized solutions for problems related to ice streams and their interactions with ice domes and ice shelves.

The observational tests designed to evaluate concepts of how the ice dome–ice stream–ice shelf system works must rely on proven techniques. Photo interpretation of Landsat image mosaics is a new technique particularly suited to the study of ice streams. This review used this technique to test idealized analytical solutions of ice dynamics problems associated with ice streams. Other major techniques are studies of absolute surface velocities by geoceiver positioning, surface strain dis-

tributions by strain networks, bed profiling by radar sounding, ice-bed coupling by radar and seismic sounding, internal ice structures using geophysical methods (radar, seismic, and electrical resistivity profiling) and core hole drilling (ice fabric, texture, density, and purity profiling), internal ice dynamics by deep drilling (temperature profiles, deformation profiles, and basal sliding), and inflection line–grounding line dynamics by measuring gravity, tilt, and elevation variations. These and other observational tests of proven or potential worth and their limitations have been discussed by *Bentley et al.* [1972].

An ice stream begins in an ice dome and ends in an ice shelf, and since it transports most of the ice, it is in effect the junction between an ice dome and an ice shelf. This junction is the zone where rock, ice, and water meet, so it is critically sensitive to all three components of the earth's cryosphere-hydrosphere-atmosphere climatic machine. Ice sheets grow or shrink, sea level rises or falls, and the atmosphere warms or cools, depending on what happens in this zone. The ice dome–ice shelf junction is also the zone where glacial erosion stops and glacial deposition begins, especially in ice streams. It is therefore a fundamental threshold in the glacial geological record. Freshwater melted from the ice shelf or discharged from under the ice dome may form a continuous layer above the heavier sea water under the ice shelf. Tidal pumping of the ice shelf might therefore generate internal gravity waves in the stratified water which are focused at the ice dome–ice shelf junction. Shoaling of these waves along the junction may be a major mechanism for eroding both ice and bedrock via the abrasive action of rock particles entrained in the water [*Cacchione and Southard,* 1974]. Bottom crevasses also form along the ice dome–ice shelf junction and can extend much further into the ice than top crevasses because they are flooded by water [*Weertman,* 1973]. These bottom crevasses, filled with sea ice, may be weak zones in the ice shelf which help determine iceberg calving rates along the ice shelf barrier and therefore partly control ice shelf stability [*Hughes,* 1974, 1975*a*]. Finally, absolute retreat or advance of the ice dome–ice shelf junction will provide an ultimate answer to the question, 'Is the West Antarctic ice sheet disintegrating?' [*Hughes,* 1973*b*, 1975*a*; *Weertman,* 1974; *Thomas,* 1976].

Acknowledgments. Many of the ideas expressed in this review grew out of lengthy discussions with my colleagues at the University of Maine, H. W. Borns, Jr., G. H. Denton, J. T. Hollin, and R. H. Thomas. I am especially grateful to E. S. Robinson and R. H. Thomas for critically reviewing the manuscript, P. Calkin of the State University of New York at Buffalo for his radar sounding analysis of Byrd Glacier which was used in Figure 2, and W. R. MacDonald of the United States Geological Survey for providing the preliminary Landsat ERTS 1 image mosaics, which are reproduced in Figure 26 and provide the basic field observations for testing the models proposed in this review. I am indebted to R. H. Thomas for valuable suggestions in the Byrd Glacier analysis, my wife Beverly for typing the manuscript, and Pauline Whiting for helping draft the figures. This work is part of the University of Maine contribution to Climap and Wisp and was done in part while the author was a Senior Post-doctoral Fellow in the Advanced Study Program at the National Center for Atmospheric Research, which is sponsored by the National Science Foundation.

REFERENCES

Bentley, C. R., et al., The international Antarctic glaciological project standardization document, *Polar Rec., 16,* 349–364, 1972.

Boas, W., and M. E. Hargreaves, On the inhomogeneity of plastic deformation in the crystals of an aggregate, *Proc. Roy. Soc. London, Ser. A, 193,* 89–97, 1948.

Budd, W., The dynamics of ice masses, *Aust. Nat. Antarctic Res. Exped. Sci. Rep., Ser. A, 108,* 1969.

Budd, W., A first simple model for periodically self-surging glaciers, *J. Glaciol., 14,* 3–21, 1975.

Cacchione, D. A., and J. B. Southard, Incipient sediment movement by shoaling internal gravity waves, *J. Geophys. Res., 79,* 2237–2242, 1974.

Carbonnell, M., and A. Bauer, Exploitation des couvertures photographiques aériennes répétées du front des glaciers vêlant dans Diske Bugt en Umanak Fjord, juin–juillet, 1964, *Medd. Grønland, 173*(5), 1–78, 1968.

Denton, G. H., and H. W. Borns, Former grounded ice sheets in the Ross Sea, *Antarctic J. U.S., 9,* 167, 1974.

Dieter, G. E., *Mechanical Metallurgy,* McGraw-Hill, New York, 1961.

Elbaum, C., The relation between the plastic deformation of single crystals and polycrystals, *Proc. Symp. Naval Struct. Mech. 2nd,* 107–120, 1960*a*.

Elbaum, C., Plastic deformation of aluminum multicrystals, *Trans. AIME, 218,* 444–448, 1960*b*.

Fletcher, J. O., Rumination on climate dynamics and program management, memorandum, Off. of Polar Programs, Nat. Sci. Found., Washington, D. C., July 18, 1972.

Giovinetto, M., E. S. Robinson, and C. W. M. Swithinbank, The regime of the western part of the Ross Ice Shelf drainage system, *J. Glaciol., 6,* 55–68, 1966.

Glen, J. W., The creep of polycrystalline ice, *Proc. Roy. Soc., Ser. A, 228,* 519–538, 1955.

Goodman, D. G., H. J. Frost, and M. F. Ashby, The effect of impurities on the creep of ice I_h and its illustration by the construction of deformation maps, paper presented at Sixteenth General Assembly of the International Union of Geodesy and Geophysics, Grenoble, France, Aug. 1975. (Available from Cavendish Laboratory, Cambridge, England.)

Hawkes, I., and M. Mellor, Deformation and fracture of ice under uniaxial stress, *J. Glaciol., 11,* 103–131, 1972.

Hendershott, M. C., Ocean tides, *Eos Trans. AGU, 54,* 76–86, 1973.

Hetényi, M., *Beams on Elastic Foundation,* University of Michigan Press, Ann Arbor, 1946.

Higashi, A., Mechanisms of plastic deformation in ice single crystals, in *Physics of Snow and Ice,* edited by Hirobumi Ôura, Institute of Low Temperature Science, Hokkaido University, Sapporo, Japan, 1967.

Higashi, A., Mechanical properties of ice single crystals, in *Physics of Ice,* edited by N. Riehl, B. Bullemer, and H. Engelhardt, pp. 197–212, Plenum, New York, 1969.

Higashi, A., S. Koinuma, and S. Mae, Plastic yielding of ice single crystals, *Jap. J. Appl. Phys., 3,* 610–616, 1964.

Higashi, A., S. Mae, and A. Fukuda, Strength of ice single crystals in relation to the dislocation structure, *Proc. Int. Conf. Strength Metals Alloys 1967,* 784–789, 1968.

Hill, R., *The Mathematical Theory of Plasticity,* Oxford University Press, New York, 1964.

Holdsworth, G., Flexure of a floating ice tongue, *J. Glaciol., 8,* 385–397, 1969.

Holdsworth, G., Tidal interaction with ice shelves, paper presented at International Symposium on Tidal Interactions, Including Earth Tides, Sixteenth General Assembly of the International Union of Geodesy and Geophysics, Grenoble, France, Aug. 1975.

Hollin, J. T., Interglacial climates and Antarctic ice surges, *Quaternary Res., 2,* 401–408, 1972.

Hopkins, W., On the theory of the motion of glaciers, *Phil. Trans. Roy. Soc. London, 152*(2), 677–745, 1862.

Hoppe, G., Isrecessionen från Norbottens Kustland i belysning av de glaciala formelementon, *Geogr. Skr. Uppsala Univ. Geogr. Inst., 20,* 1–112, 1948.

Hughes, T., Scientific justification, *ISCAP Bull. 1,* Inst. of Polar Stud., Ohio State Univ., Columbus, 1972*a*.

Hughes, T., Elastic and viscoplastic tidal flexure of floating ice, A Study Prepared for the Greenland Outlet Glacier Survey, U.S. Coast Guard, New London, Conn., 1972*b*.

Hughes, T., Science plan, *ISCAP Bull. 2,* Inst. of Polar Stud., Ohio State Univ., Colombus, 1973*a*.

Hughes, T., Is the West Antarctic ice sheet disintegrating?, *J. Geophys. Res., 78,* 7884–7910, 1973*b*.

Hughes, T., Study of unstable Ross Sea glacial episodes, *ISCAP Bull. 3,* Inst. for Quaternary Stud., Univ. of Maine, Orono, 1974.

Hughes, T., The West Antarctic ice sheet: Instability, disintegration, and initiation of ice ages, *Rev. Geophys. Space Phys., 13,* 502–526, 1975*a*.

Hughes, T., West Antarctic ice streams, *ISCAP Bull. 4,* Inst. for Quaternary Stud., Univ. of Maine, Orono, 1975*b*.

Hughes, T., The theory of thermal convection in polar ice sheets, *J. Glaciol., 16,* 41–71, 1976.

Hughes, T., G. H. Denton, and M. G. Grosswald, Was there a late

Würm Arctic Ice Sheet?, *Nature*, in press, 1977.
Johnsen, S. W., W. Dansgaard, H. B. Clausen, and C. C. Langway, Oxygen isotope profiles through the Antarctic and Greenland ice sheets, *Nature, 235*, 429–434, 1972.
Kamb, W. B., The glide direction in ice, *J. Glaciol., 3*, 1097–1106, 1961.
Kawada, T., On the plastic deformation of zinc bicrystals, *J. Phys. Soc. Jap., 6*, 364, 485, 1951.
Langway, C. C., M. Herron, and J. H. Cragin, Chemical profile of the Ross Ice Shelf at Little America V, Antarctica, *Res. Rep. 316*, U.S. Army Cold Reg. Res. and Eng. Lab., Hanover, N. H., 1974.
Livingston, J. D., Multiple slip in bicrystal deformation, *Acta Met., 5*, 322–327, 1957.
MacDonald, W. R., Geodetic control in polar regions for accurate mapping with ERTS imagery, ERTS-1: A New Window on Our Planet, *Geol. Surv Prof. Pap. 929*, 34–36, 1976*a*.
MacDonald, W. R., Antarctic cartography, ERTS-1: A New Window on Our Planet, *Geol Surv. Prof. Pap. 929*, 37–43, 1976*b*.
MacDonald, W. R., Glaciology in Antarctica, ERTS-1: A New Window on Our Planet, *Geol. Surv. Prof. Pap. 929*, 194–195, 1976*c*.
Mercer, J. H., Antarctic ice and Sangamon sea level, *Int. Ass. Sci. Hydrol. Publ. 79*, 217–225, 1968.
Nye, J. F., The flow of glaciers and ice-sheets as a problem in plasticity, *Proc. Roy. Soc. London, Ser. A, 207*, 554–572, 1951.
Nye, J. F., The mechanics of glacier flow, *J. Glaciol., 2*, 82–93, 1952.
Nye, J. F., The distribution of stress and velocity in glaciers and ice sheets, *Proc. Roy Soc London, Ser. A, 239*, 113–133, 1957.
Nye, J. F., The response of glaciers and ice-sheets to seasonal and climatic changes, *Proc. Roy. Soc. London, Ser. A, 256*, 559–584, 1960*a*.
Nye, J. F., *Physical Properties of Crystals*, Oxford University Press, New York, 1960*b*.
Orowan, E., Convection in a non-Newtonian mantle, continental drift, and mountain building, *Phil. Trans. Roy. Soc London, Ser. A, 258*, 284–313, 1965.
Paterson, W. S. B., *The Physics of Glaciers*, Pergamon, New York, 1969.
Robin, G. de Q., Glaciology III: Seismic shooting and related investigations, *Sci. Result. Norw. Brit.-Swed. Antarct. Exped. 1949–1952, 5*, 1958.
Robin, G. de Q., Ice shelves and ice flow, *Nature, 253*, 168–172, 1975.
Robinson, E. S., H. A. C. Neuburg, and R. Williams, Ocean tides beneath the Ross Ice Shelf, *Antarctic J. U.S., 9*, 162–164, 1974.
Southard, R. B., and W. R. MacDonald, Erts-1 imagery applications in polar regions, *Antarctic J. U.S., 9*, 61–67, 1974.
Swithinbank, C. W., Ice shelves, *Geogr. J., 121*, 64–76, 1955.
Swithinbank, C. W., Ice movement of valley glaciers flowing into the Ross Ice Shelf, Antarctica, *Science, 141*, 523–524, 1963.
Thiel, E., and N. A. Ostenso, The contact of the Ross Ice Shelf with the continental ice sheet, Antarctica, *J. Glaciol., 3*, 823–832, 1961.
Thiel, E., A. P. Crary, R. A. Haubrich, and J. C. Behrendt, Gravimetric determination of ocean tide, Weddell and Ross seas, Antarctica, *J. Geophys. Res., 65*, 629–636, 1960.
Thomas, R. H., Flow law for Antarctic ice shelves, *Nature Phys. Sci., 232*, 85–87, 1971.
Thomas, R. H., The creep of ice shelves: Theory, *J. Glaciol., 12*, 45–53, 1973*a*.
Thomas, R. H., The creep of ice shelves: Interpretation of observed behavior, *J. Glaciol., 12*, 55–70, 1973*b*.
Thomas, R. H., Thickening of the Ross Ice Shelf and equilibrium state of the West Antarctic ice sheet, *Nature, 259*, 180–183, 1976.
Weertman, J., Deformation of floating ice shelves, *J. Glaciol., 3*, 38–42, 1957.
Weertman, J., Stability of ice-age ice sheets, *J. Geophys. Res., 66*, 3783–3792, 1961.
Weertman, J., Creep of ice, in *Physics and Chemistry of Ice*, edited by W. Whalley, S. J. Jones, and L. W. Gold, Royal Society of Canada, Ottawa, Ont., 320–337, 1963.
Weertman, J., Rate of growth or shrinkage of nonequilibrium ice sheets, *J. Glaciol., 5*, 145–158, 1964*a*.
Weertman, J., The theory of glacier sliding, *J. Glaciol., 5*, 287–303, 1964*b*.
Weertman, J., Water lubrication mechanism of glacier surges, *Can. J. Earth Sci., 6*, 929–942, 1969.
Weertman, J., Can a water-filled crevasse reach the bottom surface of a glacier?, *Int Ass. Sci. Hydrol. Publ. 95*, 139–145, 1973.
Weertman, J., Stability of the junction of an ice sheet and ice shelf, *J. Glaciol., 13*, 3–11, 1974.
Weertman, J., Glaciology's grand unsolved problem, *Nature, 260*, 284–286, 1976.
Whillans, I. M., State of equilibrium of the West Antarctic inland ice sheet, *Science, 182*, 476–479, 1973.
Wilson, A. T., Origin of ice ages: An ice shelf theory for Pleistocene glaciation, *Nature, 201*, 147–149, 1964.

(Received June 8, 1976;
accepted September 23, 1976.)